ETH
Eidgenössische Technische Hochschule Zürich
Swiss Federal Institute of Technology Zurich

IPA

Nuclear effects for electron neutrino - nucleus interactions and their impact on the search for CP violation at the T2K and Hyper-K experiments

Master's Thesis

Till Dieminger

Institute for Particle Physics and Astrophysics
Rubbia Group
ETH Zürich

Supervisors:
Prof. Dr. André Rubbia
Prof. Dr. Davide Sgalaberna

April 1, 2022

In Erinnerung an Augustine Dieminger.

Acknowledgements

I would like to thank Prof. Rubbia for the possibility of completing my Master's thesis in his group. I would also like express my deepest gratitude to Davide Sgalaberna and Stephen Dolan for the great supervision I was allowed to experience. Both spend their valuable time explaining the details of the topics we worked on, but also created an environment in which I could feel comfortable asking questions and working on interesting side topics. They also used the time they gave me to introduce me in to the working process at T2K and gave me the possibility to contribute to this experiment. I want to thank them for their trust and energy they put in to me.

Tom Dealtry helped me to get the VALOR framework running and guided me through the process of overcoming the problems a novice will run in to using such methods. I want to sincerely thank him for his patience and extraordinary explanations of the handling and inner workings of the code used for the sensitivity study.

Furhter I would like to thank Aoi Eguchi for the many discussions about physics and culture we had during the time of my thesis. It was a pleasure to share an office with him.

A final thanks to Justyna for her strong and steady support during the whole time of my very turbulent master studies and especially during these last six months.

Abstract

After the success of long-baseline (LBL) neutrino experiments, like T2K, in measuring neutrino oscillations, the focus now lies on the determination of the oscillation parameters and the search for Charge-Parity (CP) violation in the leptonic sector by precisely measuring the $\nu_\mu \to \nu_e$ and $\overline{\nu}_\mu \to \overline{\nu}_e$ appearance probabilities. One of the dominant systematic uncertainties in the measurements of CP violation comes from our modeling of the $\nu_e/\overline{\nu}_e$ cross-section ratio, which is subject to a range of uncertainties related to poorly-constrained nuclear physics processes. Whilst tight constraints on the $\nu_\mu/\overline{\nu}_\mu$ cross-section can be achieved using LBL experiment's near detector data, the lepton mass differences mean that the extrapolation to $\nu_e/\overline{\nu}_e$ is not trivial.

Currently running LBL experiments reach a sensitivity to exclude the CP conserving hypothesis of about three standard deviations for a relatively large range of δ_{CP} values, hence a more accurate evaluation of the $\nu_e/\overline{\nu}_e$ related uncertainties becomes increasingly crucial. Nikolakopoulos et al. [1] showed that a more consistent treatment of final state interactions (FSI) via a distortion of the outgoing nucleon wave function within an Hartree-Fock (HF) mean-field model for charged-current quasi-elastic (CCQE) interactions with continuum random phase approximation (CRPA) corrections leads to significantly different predictions for muon and electron neutrino cross sections at low energy transfers compared to widely used plane wave impulse approximation (PWIA) models, such as Spectral Function (SF), usually employed in LBL experiment's interaction simulations.

Following up on this work, we show how HF-CRPA predictions of the $\nu_\mu(\overline{\nu}_\mu)$ - $\nu_e(\overline{\nu}_e)$ cross-section ratio differs from the widely used models employed in the NEUT and GENIE neutrino interaction event generators. In a second step, we proceed to estimate the potential impact of such model differences on future measurements of CP-violation by the HK experiment. For this we estimate a systematic uncertainty for the cross-section ratio $\nu_e/\overline{\nu}_e$ and perform sensitvity and resolution studies to estimate the effect of the added uncertainty on the HK experiment with different sets of systematic uncertainties.

In the course of this work, an algorithm for extrapolating the CRPA from the SF cross-section was developed and implemented in the newest version of NIWGReWeight.

Contents

Contents

Introduction

James Chadwick's measurement of a continuous energy spectrum of electrons released in beta decays, which at this point was thought to be a two-body decay, led Wolfgang Pauli to the desperate measure of postulating a neutral, massless, and very weakly interacting particle - which he called the neutron and we today know as the neutrino. In his often cited letter to a conference in Tübingen, he apologized for the introduction of a particle, almost impossible to measure, but this was, in his eyes, the only way to retain the concept of energy and momentum conservation. After the theoretical groundwork on the neutrino interaction by Enrico Fermi [2] got published in 1934, it took almost twenty years until Reines and Cowan [3] found the first hints of this particle in 1953. These first observations were followed up in 1956 with further measurements that confirmed the existence of the neutrino.

Over many years since then, even though neutrinos are only interacting using the weak force, a large number of interactions of the three neutrino flavors have been measured and many of the original properties of it confirmed. The main difference between the particle we know today and the original description of Fermi's theory is its mass. Fermi's neutrino was massless, as is the case for the neutrino in the standard model, while the observation of neutrino oscillation, first predicted by Bruno Pontecorvo [4] in 1957 and finally confirmed by the Super Kamiokande [5] and SNO experiments, require the neutrinos to be massive. Although the precise masses and the hierarchy between them are not yet measured, due to the confirmation of neutrino oscillations, it is well established that at least two of them are non-zero. Besides the measurement of the masses and their hierarchy, the neutrino sector poses further interesting questions, for example, if the neutrino is a Dirac or Majorana particle or the existence of a CP-violating phase in the mixing matrix and the large mass differences inside the lepton doublets. These are investigations that open a path to the study of nature beyond the standard model.

Beyond the study of their intrinsic properties, the interest in neutrinos extends to a variety of topics in astro- and nuclear physics. An understanding of CP violation could lead to an explanation of why we exist - or more precisely, why there is an asymmetry between matter and anti-matter. A current explanation, the so-called Leptogenesis [6] requires an asymmetry between the Leptons and their anti-particles, something that could be achieved with a CP-violating phase in the neutrino sector.

1. INTRODUCTION

T2K and Hyper-Kamiokande (HK), the experiments on which this thesis is based, measure the extent of CP violation in the neutrino sector. Like every experiment, they need to consider systematic uncertainties in their evaluation of the measured data. This thesis tries to estimate and evaluate one of these uncertainties, i.e. how different modeling of the nuclear effects affects the sensitivity to the CP-violating phase. For this, the next chapter serves as an introduction to the basics of neutrino physics awhile the third summarises the T2K and HK experiments. The fourth chapter uses different models to evaluate the impact of the modeling on cross-section ratios used in the HK experiment and tries to define an overall uncertainty. The final chapter investigates the effect that this added uncertainty has on the HK experiment.

Neutrino Physics and Oscillations

This chapter presents the basics of neutrino physics in the standard model and the beyond standard model phenomena of neutrino oscillations. When it comes to standard model physics, the neutrino interaction on quarks are not discussed, the focus lies on the interaction with nucleons like protons and neutrons and the subsequent interaction of the final state particles inside a larger nucleus.

2.1 Neutrinos in the Standard Model

In the Standard Model of Particle Physics (SM) neutrinos are one of the fundamental particles. They are the only massless fermions and are solely charged under the weak interaction. This means that the only force affecting them is the weak force with its small cross-section, which makes them hard to detect, hence large target masses are required.

Neutrinos come in three flavors, corresponding to the three electrically charged leptons in the standard model. The neutrinos form doublets with the corresponding left-handed leptons, as it is assumed that no right-handed neutrinos exist. The corresponding right-handed electrically charged leptons form singlets. Therefore the standard model contains the left-handed electron-, muon-, and tau neutrino (ν_e, ν_μ, ν_τ) and their corresponding right-handed anti-particles ($\overline{\nu}_e, \overline{\nu}_\mu, \overline{\nu}_\tau$).

2.1.1 Neutrino Interactions

Neutrinos can only interact using $W^\pm$ or Z_0 bosons, the mediators of the weak force. The interactions via the first are called charged currents, while interactions using the latter are called neutral currents. Every fermion in the standard model carries a weak charge. Due to this, neutrinos can interact with all leptons and the complete quark sector. Since quarks are always bound in a hadron or meson, the interactions are usually depicted on the corresponding hadron.

Neutral currents do not allow for any charge exchange between the interacting particles and only change their corresponding momentum and spins. Therefore the initial

and final states include the same particles and can be written as $\nu + f \to \nu + f$, where f is any fermionic particle in the standard model. There always is a neutrino in the final state. The corresponding Feynman diagram is shown in fig. 2.1. This interaction does not allow for the determination of the neutrino flavor, which is a requirement in the measurement of neutrino oscillations, a phenomenon discussed in section 2.2.
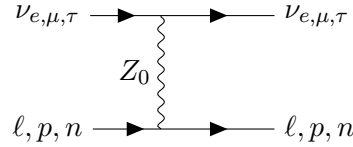
Figure 2.1: Feynman diagram for the Neutral Current (NC) interactions.

Charged currents on the other hand exchange electric charge between the scattered particles, which allows for a wider variety of interactions. Similar to the neutral current interactions there can be interactions that have a neutrino in both the initial and final state, as depicted in fig. 2.2a. But in this case, the final state neutrinos can be of different flavor compared to the initial state neutrino. In this case, the charged nature of the W boson forces a charge transfer, meaning that the leptons change the branch on which they sit on the Feynman diagram.

Due to the transfer of electric charge by the W boson, an interaction on a hadron with a neutrino in the inital and final state, similar to the neutral current, is not allowed. The scattering of a neutrino on a neutron and a final state with the corresponding lepton and a proton however is allowed. Since a charged current neutrino interaction creates a lepton corresponding to its flavor, while an anti-neutrino creates the corresponding anti-lepton, charge conservation dictates that neutrinos can only scatter on neutrons and not protons and vice-versa for anti-neutrinos. The corresponding Feynman diagram can be found in fig. 2.2b. Since the interaction partner of the neutrino is not a lepton but a quark or nucleon in a bound state, this interaction is called a semi-leptonic interaction. Effectively, the flavor of neutrinos is determined by the final state lepton of the charged current interactions.

(a) Charged Current Interaction with Leptons

(b) Charged Current Interaction with Quarks or Hadrons

Figure 2.2: Two Feynman diagrams for the charged current (CC) interactions. (a) shows the exchange of a W boson with a lepton, leading to a fully leptonic final state. (b) shows the interaction between a neutrino and a quark, called the semi-leptonic interaction.

2.2 Neutrino Oscillations & Massive Neutrinos

2.2.1 Vacuum Oscillations

In the Standard Model, neutrinos are massless. It was theorized that the mass eigenstates are a non-trivial superposition of the different flavors, also called the weak eigenstates. This leads to a phenomenon called neutrino oscillation, where neutrinos change their flavor under propagation, as they interact in the weak eigenstates and propagate using the mass-eigenstates. This was later experimentally shown by Super Kamiokande and SNO, as they found that neutrinos change their flavors, i.e. that the neutrino flavor states oscillate. This requires that the masses of at least two neutrinos have to be non-vanishing and the mass differences to be quite small [7]. This is due to the requirement of coherent production and detection of different neutrino species and the Heisenberg principle. More details can be found in appendix B.

The superposition of the three different mass eigenstates for a given weak eigenstate can be written using a 3×3 matrix

$$\begin{pmatrix} \nu_e \\ \nu_\mu \\ \nu_\tau \end{pmatrix} = \begin{pmatrix} U_{e1} & U_{e2} & U_{e3} \\ U_{\mu 1} & U_{\mu 2} & U_{\mu 3} \\ U_{\tau 1} & U_{\tau 2} & U_{\tau 3} \end{pmatrix} \begin{pmatrix} \nu_1 \\ \nu_2 \\ \nu_3 \end{pmatrix}.$$

Assuming three neutrino flavours, this matrix is unitary and satisfies

$$\sum_i U_{\alpha i} U_{\beta i}^* = \delta_{\alpha\beta}, \quad \text{and} \quad \sum_\alpha U_{\alpha i} U_{\alpha j}^* = \delta_{ij}. \tag{2.1}$$

If a non-unitarity is found, this could hint at the existence of a further neutrino, i.e. a sterile. These do not interact using the weak force, so are only interacting via the gravitational force or an oscillation between active and sterile neutrinos with their environment.

The probability to detect a neutrino in the weak eigenstate β, that started in the weak eigenstate $\alpha \neq \beta$, is given as $\|\langle \nu_\beta | \nu_\alpha(t) \rangle\|^2$. For the vacuum propagation of $|\nu_\alpha\rangle$, the eigenstates of the Hamiltonian $\mathcal{H} |\nu_i\rangle = E_i |\nu_i\rangle$ are used, as they evolve simply as $|\nu_i(t)\rangle = \exp(-iE_i t) |\nu_i\rangle$, where $E_i = \sqrt{\vec{p}^2 + m_i^2}$. At time t this expression is then rewritten in terms of the weak eigenstates $|\nu_\sigma\rangle$:

$$|\nu_\alpha(t)\rangle = \sum_i U_{\alpha,i} \exp(-iE_i t) |\nu_i\rangle = \sum_{i,\sigma} U_{\alpha,i} e^{-ipt} \exp\left(-i\frac{m_i^2 t}{2E}\right) U_{\sigma,i}^\dagger |\nu_\sigma\rangle. \tag{2.2}$$

The neutrino oscillation probability, i.e. the probability to measure ν_β at t, is now

5

2. Neutrino Physics and Oscillations

given by :

$$\mathcal{P}(\nu_\alpha \to \nu_\beta) = \|\langle \nu_\beta | \nu_\alpha(t) \rangle\|^2$$

$$= \delta_{\alpha\beta} - 4 \sum_{i>j} \Re(U_{\alpha i}^\dagger U_{\beta i} U_{\alpha j} U_{\beta j}^\dagger) \sin^2\left(\frac{\Delta m_{ij}^2 L}{4E}\right) \qquad (2.3)$$

$$\pm 2 \sum_{i>j} \Im(U_{\alpha i}^\dagger U_{\beta i} U_{\alpha j} U_{\beta j}^\dagger) \sin\left(\frac{\Delta m_{ij}^2 L}{4E}\right),$$

where $L = ct$ is the approximation of the traveled distance and $\Delta m_{ij}^2 = m_i^2 - m_j^2$ is the squared mass difference. The assumption that all neutrinos are of the same energy is used, as well as the approximation that

$$E_i - E_j \approx \frac{m_i^2 - m_j^2}{2E} := \frac{\Delta m_{ij}^2}{2E}. \qquad (2.4)$$

These approximations can be lifted when using wave packets for the derivation, resulting, after a more tedious calculation, in the same oscillation probability.

Doing the same derivation for $\mathcal{P}(\overline{\nu}_\alpha \to \overline{\nu}_\beta)$, the sign in front of the imaginary part in eq. (2.3) flips. As the CP-operator maps $\mathcal{P}(\nu_\alpha \to \nu_\beta)$ to $\mathcal{P}(\overline{\nu}_\alpha \to \overline{\nu}_\beta)$, these two probabilities should be identical, if CP symmetry is assumed to hold. The term possibly violating the CP-symmetry is therefore connected to the complex phase of the mixing matrix (δ_{CP}). This means, that if $\delta_{CP} \neq 0, \pi$, CP symmetry is broken.

When $\alpha = \beta$, this probability is called survival probability or disappearance probability. For both the neutrinos and anti-neutrinos it is given as

$$\mathcal{P}(\nu_\alpha \to \nu_\alpha) = \mathcal{P}(\overline{\nu}_\alpha \to \overline{\nu}_\alpha) = 1 - 4 \sum_{i>j} |U_{\alpha i} U_{\alpha j}^*|^2 \sin^2\left(\frac{\Delta m_{ij}^2 L}{4E}\right). \qquad (2.5)$$

As it is equal for both neutrinos and anti-neutrinos, it can not be used to measure a possible CP violation. Therefore the measurement of the CP violation is purely based on the comparison of the appearance probabilities $\mathcal{P}(\nu_\alpha \to \nu_\beta)$ and $\mathcal{P}(\overline{\nu}_\alpha \to \overline{\nu}_\beta)$, where $\alpha \neq \beta$. The disappearance probability on the other hand can be used to determine the other mixing parameters.

From the oscillation formulas above, it can be seen that the squared mass-difference Δm_{ij}^2 plays an important role in the determination of the oscillation frequency. As it only appears in $\sin^2(x)$, the measurement of the oscillation probability does therefore not allow to resolve the sign of Δm_{ij}^2. Hence there are two possible ways, called mass-hierarchies, how the three masses m_1, m_2, m_3 can be ordered. The first one, called the normal hierarchy (NH), is $m_1 < m_2 < m_3$, while the second called the inverse hierarchy (IH) $m_3 < m_1 < m_2$. Nonetheless, the absolute value of the mass-differences can be measured using oscillation experiments, with the current values being $|\Delta m_{12}^2| = 7.53 \times 10^{-5} \ eV^2$ and $|\Delta m_{32}^2| = 2.54 \times 10^{-3} \ eV^2$.

Using an analogous parametrisation of the mixing matrix as to the one in the quark sector, the so-called Pontecorvo-Maki-Nakagawa-Sakata matrix, the transformation between the mass and weak eigenstates can be written as

$$
\begin{pmatrix} U_{e1} & U_{e2} & U_{e3} \\ U_{\mu1} & U_{\mu2} & U_{\mu3} \\ U_{\tau1} & U_{\tau2} & U_{\tau3} \end{pmatrix} = \begin{pmatrix} 1 & 0 & 0 \\ 0 & \cos\theta_{23} & \sin\theta_{23} \\ 0 & -\sin\theta_{23} & \cos\theta_{23} \end{pmatrix} \begin{pmatrix} \cos\theta_{13} & 0 & \sin\theta_{13}e^{-i\delta_{CP}} \\ 0 & 1 & 0 \\ -\sin\theta_{13}e^{-i\delta_{CP}} & 0 & \cos\theta_{13} \end{pmatrix}
$$
(2.6)

$$
\times \begin{pmatrix} \cos\theta_{12} & \sin\theta_{12} & 0 \\ -\sin\theta_{12} & \cos\theta_{12} & 0 \\ 0 & 0 & 1 \end{pmatrix}
$$

This matrix has four independent parameters $\theta_{12}, \theta_{23}, \theta_{13}$ and δ_{CP}. The three angles determine the mixing, and δ_{CP} is a possible complex phase. As mentioned above, this complex phase leads to different oscillation probabilities between neutrinos and anti-neutrinos and with that, to a violation of the CP symmetry.

The first matrix, including the parameter θ_{23}, is usually called atmospheric, as it appears together with the mass-difference Δm_{32}^2, which leads to an oscillation pattern of wavelength $\lambda_{32} = 4\pi E_\nu/\Delta m_{32}^2$, which is of the order of 100's kilometer. These parameters therefore can be measured using atmospheric or long-baseline neutrino experiments. Current measurements, by the T2K and MINOS experiment, show a value of $\sin^2(\theta_{23}) = 0.545$. Even though the value of $\sin^2(\theta_{23})$ is known, the quadrant of θ_{23} is not yet known.

The second matrix is called subleading, as the mixing angle $\sin^2(\theta_{13}) = 0.0218$, as measured using reactor neutrino experiments, leads to a second-order effect.

The third matrix, including θ_{12}, is called the solar matrix, as the connected mass-difference Δm_{12}^2 leads to a wavelength in the order of hundred thousands of kilometers, best probed with solar neutrinos. The current measurement value by the SK experiment is $\sin^2(\theta_{12}) = 0.307$. These values are taken from the Particle Data Group at [8].

2.2.2 Propagation through Matter

If neutrinos propagate through matter, neutral ($\nu_f + p, n, e \xrightarrow{Z_0} \nu_f + p, n, e$) and charged current ($\nu_e + e \xrightarrow{W^\pm} \nu_e + e$) interactions have to be accounted for. The neutral current interactions affect all three flavors in the same manner, while the charged current only plays a significant role for the electron neutrinos, since the matter of earth contains only electrons. This requires the introduction of a potential in the Hamiltonian, which can be described as

$$
i\partial_t \left| \nu_\alpha(t) \right\rangle = (\mathcal{H}_{vac} + V) \left| \nu_\alpha(t) \right\rangle, \qquad V = \begin{pmatrix} \sqrt{2}G_F n_e & 0 & 0 \\ 0 & 0 & 0 \\ 0 & 0 & 0 \end{pmatrix}.
$$
(2.7)

2. Neutrino Physics and Oscillations

Taking into account these matter effects and expanding the PMNS matrix for $\nu_\mu \to \nu_e$, the oscillation probability for accelerator energies can be approximated by [9]:

$$
\begin{aligned}
\mathcal{P}\left(\overset{(-)}{\nu}_\mu \to \overset{(-)}{\nu}_e\right) = {} & 4c_{13}^2 s_{13}^2 s_{23}^2 \cdot \sin^2 \Phi_{31} \\
& + 8c_{13}^2 s_{12} s_{13} s_{23} (c_{12} c_{23} \cos\delta_{CP} - s_{12} s_{13} s_{23}) \cdot \cos\Phi_{32} \sin\Phi_{31} \sin\Phi_{21} \\
& \pm 8c_{13}^2 c_{12} c_{23} s_{12} s_{13} s_{23} \sin\delta_{CP} \sin\Phi_{32} \sin\Phi_{31} \sin\Phi_{21} \quad\quad (2.8) \\
& + 4s_{12}^2 c_{13}^2 (c_{12}^2 c_{23}^2 + s_{12}^2 s_{23}^2 s_{13}^2 - 2c_{12} c_{23} s_{12} s_{13}) \cos\delta_{CP} \cdot \sin^2 \Phi_{21} \\
& - 8c_{13}^2 s_{13}^2 s_{23}^2 \frac{aL}{4E_\nu} (1 - 2s_{13}^2) \cdot \cos\Phi_{32} \sin\Phi_{31} \\
& + 8c_{13}^2 s_{13}^2 s_{23}^2 \frac{a}{\Delta m_{31}^2} (1 - 2s_{13}^2) \cdot \sin^2 \Phi_{31}.
\end{aligned}
$$

Here c_{ij} and s_{ij} are short-forms of $\cos\theta_{ij}$ and $\sin\theta_{ij}$ respectively and Φ_{ij} was used for $\frac{\Delta m_{ij}^2 L}{4E}$. The matter effects are summarized in the parameter $a = 2\sqrt{2} G_F n_e E_\nu$, where n_e is the electron density in matter. The first term is the quasi 2-neutrino oscillation probability, the second term is CP invariant and the third term violates CP symmetry. The fourth term is the so-called solar term and the last two terms are the included matter effects. To understand why the second and third terms are respectively CP invariant and violating, one has to calculate the same probability after a CP transformation; meaning $\mathcal{P}(\bar{\nu}_\mu \to \bar{\nu}_e)$. This results in the same equation but changing $\delta \mapsto -\delta$ in all terms. While the second term is symmetric under this transformation, the third one is not, meaning that it violates the CP-symmetry if δ_{CP} is non-trivial. The individual contributions to the corresponding oscillation probability are shown in fig. 2.3 for a fixed neutrino flight path of 295 km. The blue dotted line, corresponding to the third term of eq. (2.8), is different for neutrino and anti-neutrino oscillations. This is the effect of the CP-violating term. The matter effects are not the same for neutrinos and anti-neutrinos either. This can be analyzed and used to determine the sign of Δm^2 (mass hierarchy) [10]. The size of matter effects for a fixed neutrino flight path of 295 km can be seen in fig. 2.4

(a) The neutrino oscillation probability.

(b) The anti-neutrino oscillation probability.
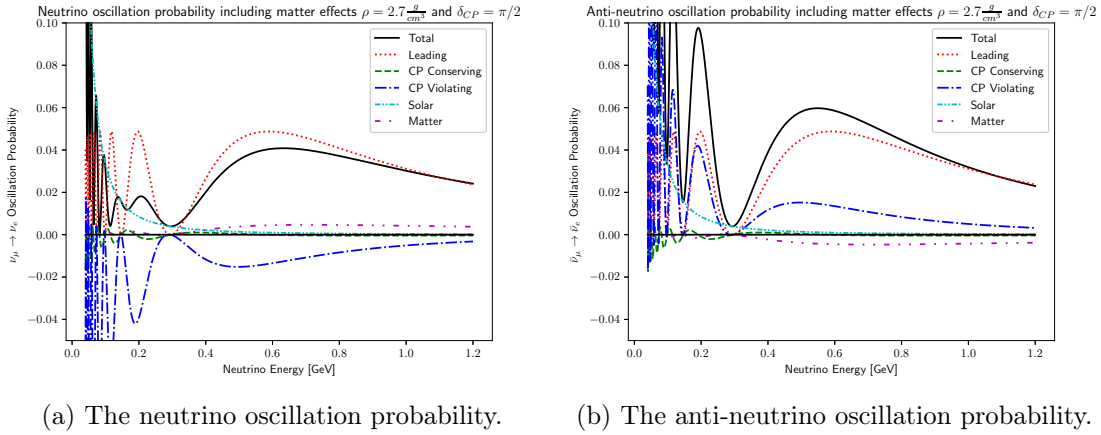
Figure 2.3: The oscillation probabilities for a distance of $L = 295$ km, split up in to the different contributions. A δ_{CP} phase of $\pi/2$ is assumed. For the matter effects, an average density of 2.7 g/cm^3 is approximating the density of the earth is used. The change in the CP-violating contribution in blue is clearly visible. Further the matter contributions are different for the neutrino and anti-neutrino oscillation probabilities. The neutrino travel distance is chosen to be the one of the T2K experiment.
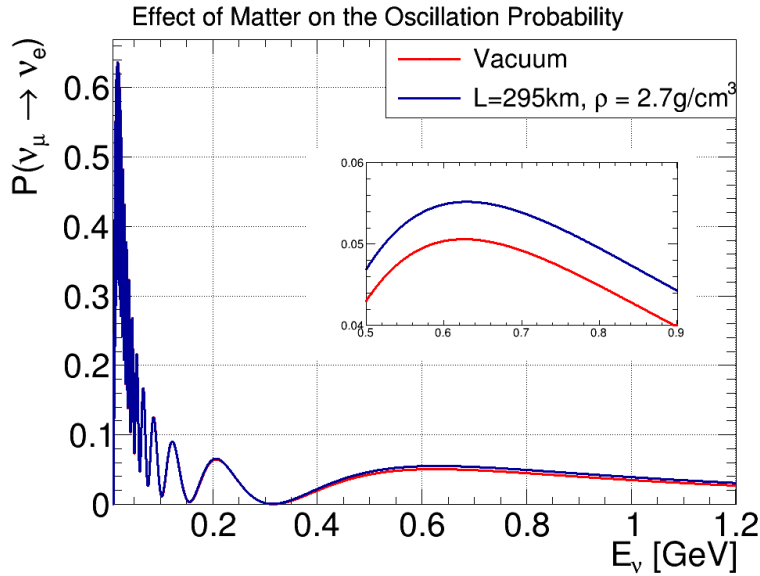
Figure 2.4: The ν_e appearance probability for L=295 km, plotted in vacuum and in a material with an average density of 2.7 g/cm^3. Although the difference at energies below 0.5 GeV is small, at around 600 MeV the fractional difference is about 10%. The neutrino travel distance is chosen to be the one of the T2K experiment.

9

2.3 Neutrino Interactions at Accelerator Experiments

Current long-baseline (LBL) experiments, like the T2K experiment this thesis is based on and which will be described in the next chapter, have neutrino beams with energies up to several GeV. Thus the focus in this section lies on the interactions at energies in this region. As the determination of the neutrino flavor is an important requirement for these experiments, the focus will further be on semi-leptonic charged current interactions.

2.3.1 Semileptonic Interactions

In electron-proton scattering experiments the momentum transfer Q^2 is often regarded as the inverse of the spacial resolution the experiment can achieve. While for lower Q^2 values the electron scatters on the whole proton, higher Q^2 value allow to resolve the point-like subparticles of the proton in the deep-inelastic scattering. Similarly the momentum transfer plays a key role in determining the type of interaction in neutrino experiments. An event with a low Q^2 value can be thought of as the neutrino interacting with the nucleus. Events with a higher energy-momentum transfer will instead interact with the nucleons or even the quarks inside the nucleus. It is therefore sensible to categorize the semileptonic interactions into three regions according to the momentum transfer.

- Nuclear interaction: $Q^2 \ll 1 \; GeV^2$

- Intermediate interaction: $Q^2 \approx 1 \; GeV^2$

- Deep Inelastic Scattering: $Q^2 \gg 1 \; GeV^2$

In the deep inelastic scattering (DIS) regime, the neutrino probes the bare quarks inside the bound nucleus, while for the nuclear region, the interaction takes place between the neutrino and the nucleus of the target material. Since most accelerator experiments are dominated by events in the intermediate region, the focus will be on interactions with momentum transfers slightly below 1 GeV. Here the interaction can be thought of as occurring between the neutrino and a single nucleon in the nucleus.

Inside the intermediate region, there are again three different modes of interaction, each corresponding to different physics. The most abundant is the so-called quasi charged current quasi-elastic interaction (CCQE), where a neutrino (anti-neutrino) interacts with a neutron (proton) and the final state includes the corresponding lepton and a proton (neutron). Since this is a two-body interaction, four-momentum conservation allows for

a reconstruction of the neutrino energy [1]

$$E_\nu^{CCQE} = \frac{m_P^2 - m_N^2 - m_\ell^2 + 2m_N E_\ell}{2(m_N - E_\ell + p_\ell \cos\theta_\ell)}. \tag{2.9}$$

Here m_f is the mass of the corresponding particle f, while E_ℓ, p_ℓ are the energy, momentum of the leptons in the final state. θ_ℓ is the leptons angle with respect to the incoming neutrino direction.

Even though this quasi two-body interaction seems simple, the calculation of the corresponding cross-section is more complicated, as it has to take into account the bound quarks and other nucleons inside the nucleus. But this poses a major problem, as their dynamics are dictated by the non-perturbative region of QCD.

The cross-section can be written using the well known leptonic tensor $L^{\mu\nu}$ and the hadronic tensor $W_{\mu\nu}$, describing the physics of the lepton and quark in the interaction respectively

$$d\sigma = G_F^2 \cos^2\theta_C \pi L^{\mu\nu} W_{\mu\nu} \frac{d^3k}{(2\pi)^3}. \tag{2.10}$$

Due to the aforementioned complications in the QCD calculations, the hadronic tensor is usually built from so-called structure functions, which allows for a phenomenological description of the interaction. For this, a variety of models were and are developed, trying to capture the complex physics of the nucleus.

The modeling of the hadronic tensor is mainly based on form-factors, which try to combine the information of the target nucleus

$$j^\mu = F_1^V(Q^2)\gamma^\mu + i\frac{\kappa}{2M}F_2^V(Q^2)\sigma^{\mu\nu}q_\nu - F_A(Q^2)\gamma^\mu\gamma^5 + F_P(Q^2)q^\mu\gamma^5. \tag{2.11}$$

There are four major form factors. Two vector form-factors $F_{1,2}^V$ model the charge distribution inside the nucleon. Under the conserved vector current (CVC) hypothesis, they are measured using electron-proton elastic scattering.

The axial form-factor $F_A(Q^2)$ models the axial part of the interaction and is usually assumed to be of a dipole form

$$F_A(Q^2) = \frac{1.267}{(1 + \frac{Q^2}{M_A^2})^2}. \tag{2.12}$$

The value at $Q^2 = 0$ can be determined using the β-decay. But as this form factor's Q^2 dependence can only be measured in neutrino scattering experiments, the parameter M_A,

---

[1] For anti-neutrinos exchange $m_N \leftrightarrow m_P$. There will be further modifications to this formula, discussed in the section about nuclear effects. They will lead to the fact that, even for pure CCQE events, a complete reconstruction formula does not exist. The reason for this is that the physical interaction is with the quark and not the nucleon. But since no information about the state of the quark or nucleon is available, the energy reconstruction will always be biased and smeared out, even for CCQE events. This can be due to effects like binding energy or the unknown initial state momentum of the nucleon.

called the axial mass, is less well constrained. Measured values lie in a range between 800 MeV and 1.35 GeV. The pseudoscalar form-factor F_P is usually neglected for neutrino experiments due to the small mass of the involved leptons.

Besides the CCQE interactions, the struck nucleon can enter the final state as an excited resonance, i.e. Δ^{++} for protons. In this case, the interaction is called a resonance interaction (CCRes). The excited nucleon decays back to its ground state while emitting a light meson, usually a pion. Therefore the final state of this interaction includes a lepton, hadron, and an extra pion. Since this requires the neutrino to have a high enough energy for the excitement and subsequent pion-mass generation, this affects mainly events in which the neutrino has an energy of approximately 1 GeV.

If the neutrino energy is significantly larger than this, the majority of interactions will have a Q^2 value larger than 1 GeV and again fall mostly in the deep inelastic region (CCDis). Here the struck nucleon carries enough energy to break the core, leading to a final state with several hadrons.

These three different physical interactions are called interaction modes. It is an incomplete list but the most important modes are the mentioned CCQE, CCRes, and CCDis. The QE cross-section dominates the region with neutrino energies below 1 GeV, while the region between 1 and 10 GeV is mainly carried by resonance scattering. Above 10 GeV the majority of the cross-section is due to the deep inelastic scattering. The predicted and measured reduced neutrino cross-section for the different interactions can be seen in fig. 2.5. Reduced cross-section means that the cross-section as a function of energy is divided by the corresponding energy $\sigma(E_\nu)/E_\nu$.

2.3.2   Nuclear Effects

The discussion above assumes that the nucleon is free, at rest and that the other nucleons do not join in the interaction. While this holds for hydrogen, for all other targets this is not the case.

In the intermediate region of interest, the interaction is traditionally considered a two-step process. First, the neutrino scatters on a bound nucleon, here the initial state of the nucleon (IS) plays a role. Then the hadrons produced in the primary scattering are affected by the surrounding nucleus in the so-called Final State Interactions (FSI). Both of which are discussed in the following.

Nucleon Initial State

Initial State Interactions (ISI) include all effects that are due to insufficient knowledge about the state of the nucleons inside the nucleus before the neutrino interaction, for example, the kinematics of the initial nucleons. Further complications arise from the fact that some nucleons may be correlated through the strong interaction. If a neutrino scatters on one of them, this leads to an ejection of two nucleons after the interactions
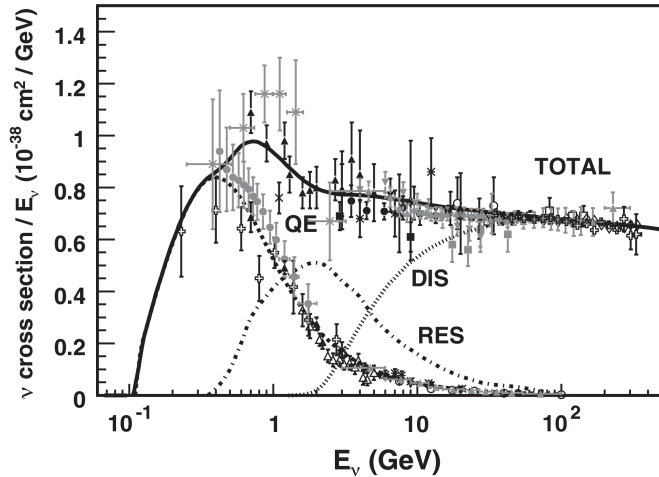
Figure 2.5: The neutrino cross-section divided by the neutrino energy on a Hydrogen target as a function of the neutrino energy. The different modes are depicted in different line styles and the inclusive cross-section is shown as a solid line. The T2K experiment uses a neutrino flux with a mean energy of around 800 MeV and a flux peak at 600 MeV. A majority of events have energy transfers in the region of a couple of hundred MeV, meaning that the majority of events will fall in the region dominated by the CCQE interactions. Figure from [11]

(2p2h interactions). Also, long-range screening effects due to the extended nucleus can affect the overall cross-section. Since all of these are effects of QCD in a nonperturbative region, these have to be modeled. These models are then included in the calculation of the cross-sections and accounted for in the energy reconstruction. Here the necessity for nuclear models in neutrino physics becomes obvious. In the following several approaches for modeling the initial state of the nucleus are discussed.

Fermi Gas
A rudimentary model to illustrate this is the so-called (relativistic) Fermi gas model (FG or RFG), in which the nucleons are considered as gas inside a potential with a binding energy E_B. The gas is characterized by the Fermi momentum p_F, which is an upper bound for the momentum inside the potential.

In this model an interaction can only occur when the energy transfer is larger than the binding energy and the final state momentum is larger than the Fermi momentum, as all momentum states below are filled by the other nucleons. This last part is called Pauli Blocking, where we see no events below the Fermi momentum in the recorded spectrum.

If the nucleon is bound inside such a potential, the binding energy E_B has to be taken into account for the energy reconstruction formula (eq. (2.9)) of CCQE events, leading

13

to

$$E_\nu^{\mathrm{CCQE}} = \frac{m_P^2 - (m_N - E_B)^2 - m_\ell^2 + 2(m_N - E_B)E_\ell}{2(m_N - E_B - E_\ell + p_\ell \cos\theta_\ell)}. \tag{2.13}$$

Not taking in to account the binding energy would have lead to a shift in the reconstruction resolution $(E_{true} - E_{reco})/E_{true}$.
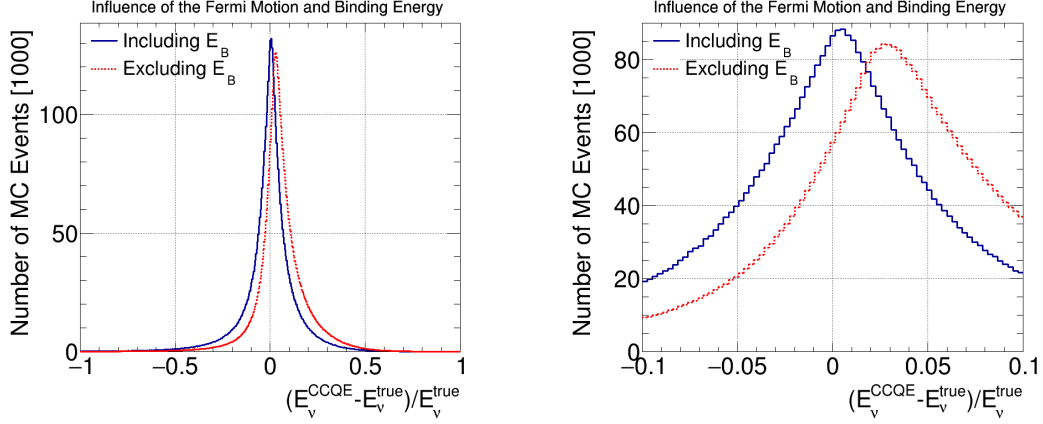
Figure 2.6: Neutrino energy resolution after reconstruction. Due to the Fermi motion of the initial state nucleon the distribution is smeared. The binding energy leads to a shift in the overall distribution if not included, as seen in the comparison between the blue solid line and the red dotted one.

As the momentum of the struck nucleon is not known or experimentally accessible, it can not be accounted for in the energy reconstruction. This leads to a smearing of the reconstructed neutrino energy as shown in fig. 2.6, meaning that even for pure CCQE events, the initial state interactions lead to an imperfect reconstruction of the energy.

Spectral Function
A more elaborate way to model the initial state of the nucleus is the so-called Spectral Function (SF) [12, 13]. This model uses a shell description for the momentum distribution and nucleon removal energy based on both electron scattering data and theoretical predictions. A further difference between the Spectral Function and the Fermi Gas is that in the latter, the initial state nucleon momentum is considered to be a uniform distribution, while for SF, the distribution includes information about the nucleus shell structure. Further, the removal energy is correlated to the momentum of the struck nucleon. The energy levels are not assumed to be discrete as in the Fermi Gas model but are considered to be Gaussian distributed. Since the tails of the Gaussian distributions overlap, the SF is, therefore, able to model nucleon-nucleon correlations. In this way, it can model interactions where the neutrino scatters on a correlated pair of nucleons, the aforementioned 2p2h interaction. The Fermi Gas is not able to model these. This highlights the importance of detailed modeling of neutrino-nucleus interactions.
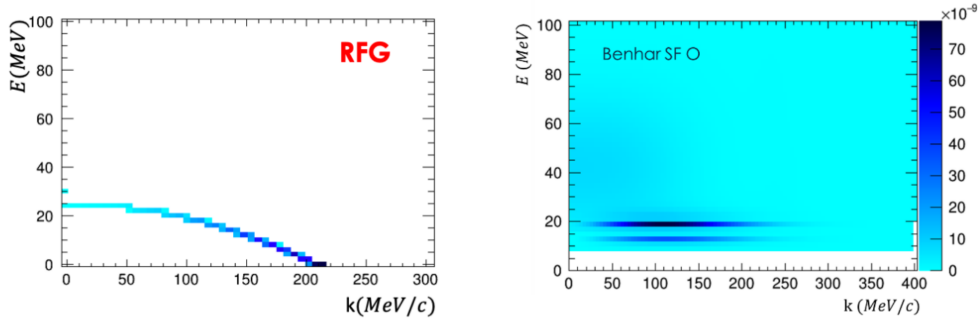
Figure 2.7: Comparison between RFG and SF nuclear ground states of Oxygen. This shows nicely the differences in removal energy and nucleon momentum. Taken from the T2K collaboration.

Final State Interactions

Final State Interactions (FSI) are interactions of the final state hadrons with the rest of the nucleus. This directly affects the final state hadrons like pions and protons, but can also have an effect on the lepton prediction due to the changed states of the struck nucleon in the final state.

Pions can undergo four main processes inside the nucleus, as depicted in fig. 2.8. A pion can get absorbed inside the nucleus, which gets important when it comes to identifying CCQE events, as discussed later in this section. The charge exchange, in which a charged pion interacts with a nucleon, also leads to a wrong classification. Further, the pion can elastically scatter on a nucleon, changing its kinematics, or an inelastic scattering can occur, leading to a production of additional pions.

In theory, leptons can undergo similar interactions, but since they would need to scatter using the electroweak interactions' small cross-section, this does not play a major role. On the other side, the final state of the lepton can be influenced by the allowed final states of the struck nucleon. This alters the energy and momentum transfer Q^2 and with this the budget available for the generation of the lepton mass and kinematics. An example for such an effect is explained below for the inclusion of Pauli Blocking, but the underlying argument that final state interactions can affect the lepton kinematics due to the available Q^2 budget holds for general FSI. Therefore the internal structure of the nucleus does not only play a role in the lepton cross-section in the initial state interactions but also in the final state interactions.

A further effect to take into account are radiative corrections, which come from higher-order Feynman graphs of the leptons. Here a photon is radiated away, which, in Cerenkov detectors, leads to a wrong reconstruction of the event topology. Further, this can also result in a changed kinematic of the lepton, influencing the reconstructed energy and recorded spectrum.

Similar to the initial state interactions, the final state interactions also complicate the
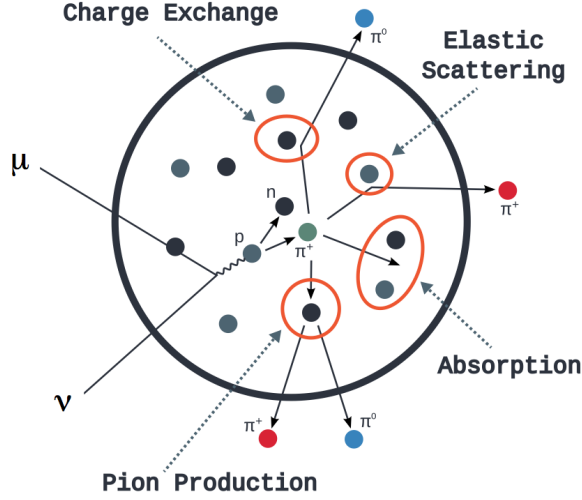
Figure 2.8: A schematic representation of the possible FSI a pion can undergo in a nucleus. Taken from [14]

reconstruction of the neutrino energy, as both can change the kinematics of the lepton, which is the main variable used in the reconstruction. It further affects the selection of CCQE events. If there would be no final state interactions, the way to differentiate between CCQE and CCRes interactions, in a perfect detector, would be the detection of the final state hadron and mesons. If no pion would be detected, a topology named CC0π, it would be clear that this interaction originates from a CCQE interaction, while if a pion would be detected, it would have to come from a CCRes interaction. This second topology is called CC1π. Similarly, the 2p2h interaction could be identified by the final state, since it is the only interaction including two final state hadrons.

But due to the final state interactions, an unequivocal correspondence is not guaranteed anymore. If the pion of a CCRes interaction got absorbed, this event is falsely attributed to be a CCQE event, while the emission of a pion would lead to the opposite classification error, a CCQE event would be interpreted as CCRes. This can also affect the 2p2h events, where one or both hadrons get absorbed. Vice versa, the elastic scattering of a final state particle could lead to the ejection of further hadrons, again leading to miss-classifications. This is summarized in fig. 2.9.

This differentiation between the physical modes and the effective finale states, called topologies, is very important to keep in mind as a background that can not be removed, even with perfect detection of all final state particles.

16
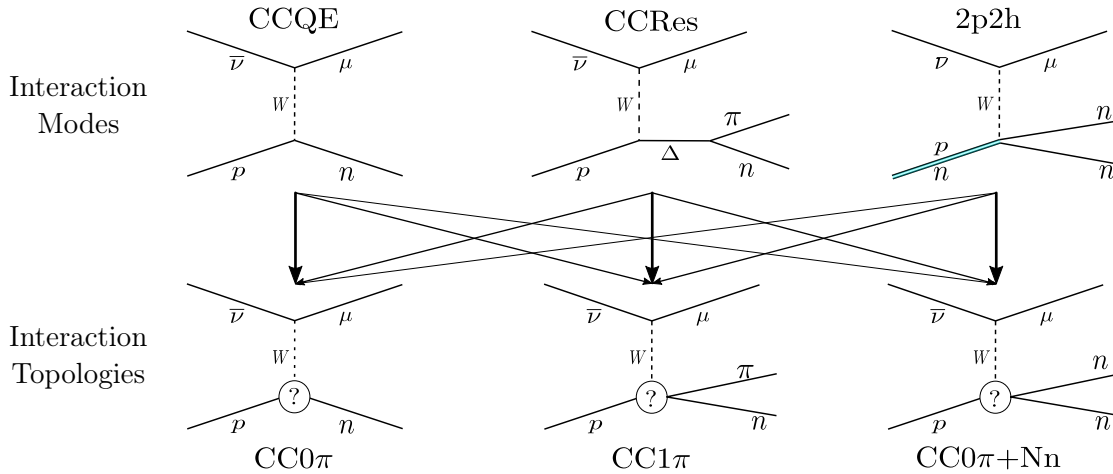
Figure 2.9: A summary of the different interaction modes and topologies. The final state interactions make it impossible to unequivocally say which interaction mode is the underlying one for a given final state composition.

Modeling of Final State Interactions

As discussed above, these non-perturbative final state interactions are due to the composite nature of the nucleus. Therefore these interactions have to be modeled phenomenologically. To do this, several different approaches are used and some of them are discussed here.

In neutrino Monte Carlo generators, one of the main methods used is the cascading method. Here particles from the primary vertex are individually propagated through the nucleus. In several steps, interactions are randomly sampled and applied.

First, the free path length of the chosen particle is determined and the particle is propagated by one free path length. If the particle is still inside the nucleus, a random sampling of possible interactions is performed. This determines what kind of scattering the particle undergoes in the nucleus. The final state particles are then similarly propagated through the rest of the nuclear core. If the particle ends up outside of the nucleus, the procedure is stopped, using the next particle from the primary vertex. Due to the small cross-sections of the electroweak interactions, this usually means that the lepton kinematics are not altered in this process.

Only if all particles left the nucleus, these are then registered as the actual final state of the full interaction. This is an effective way to include certain kinds of FSI into generators, while it does not allow to model FSI, where two particles from the primary vertex interact with each other or the influence of the final nucleus structure on the outgoing lepton.

In order to model the latter, one can use the so-called Hartree Fock method, which uses an effective potential in which the struck nucleus is sitting. This potential tries to

summarize the effect of all the other nucleons and therefore serves as an approximation of the nuclear structure. Solving the equations of motion for the scattering including this potential leads to changed kinematics of the lepton. This is because the allowed nucleon final states inside this potential dictate the allowed values of energy and momentum transfer of the lepton. This process is called the distorted wave impulse approximation. These corrections can be either calculated in a relativistic or non-relativistic approximation, an example for the first is the so-called Super Scaling Analysis Model (SuSAv2 [15]) while the latter class includes the Hartree Fock model. This does not model interactions like the hadron rescattering or pion-absorption inside the nucleus, which therefore still have to be included using a cascade model, but allows for the inclusion of the interactions between the final state particles and the deformed nucleus. This introduces a double counting of final state interactions since the effects of the rescattering of the nucleon inside the cascading model already are accounted for in the effective potential of the Hartree Fock model.

Another final state effect, which comes from a correction of the W propagator due to long-range nuclear screening, is modeled by the so-called Random Phase Approximation. The inclusion of this into the Hartree Fock model is called the Continuous Random Phase Space Approximation (CRPA) [16].

Effects of FSI on the Lepton Kinematics

In order to explain the possible effects that FSI can have on leptons, Pauli Blocking in an RFG allows for a simple and intuitive example.

The major difference at low neutrino energies between the electron and muon neutrino is the mass of the final state leptons. This difference in kinematics affects the maximal and minimal energy transfer and the available region of phase space. One example where the kinematics come into play is the Fermi Gas when Pauli Blocking is included in the relativistic Fermi gas model. This part closely follows the works in [17].

Looking at the relativistic Fermi gas model, the allowed range of the momentum transfer $|\vec{q}|$ for a given energy transfer ω is given by

$$|h - p_F| \leq |\vec{q}| \leq h + p_F, \qquad h = \sqrt{(\omega - \epsilon + E_F)^2 - M^2}, \tag{2.14}$$

where p_F is the Fermi momentum and h is the available energy of the lepton. Here ϵ parameterises the removal energy.

For an interaction to take place, the energy transfer has to surpass a minimal threshold, which is just

$$\omega_{\min} = E_{p'}^{\min} - E_F + \epsilon, \tag{2.15}$$

where $E_{p'}^{\min} = M$ when no Pauli Blocking is taken in to account. When Pauli Blocking is taken in to account, the minimal energy of the final state hadron has to be at the Fermi

energy, meaning $E_{p'}^{\min} = E_F = \sqrt{M^2 + p_F^2}$. To then produce a lepton of mass m for a given scattering angle θ, the neutrino energy has to be such that

$$|\vec{q}| = \sqrt{E_\nu^2 - 2E_\nu|\vec{k}'|\cos\theta + |\vec{k}'|^2}, \qquad (2.16)$$

where $|\vec{k}'| = \sqrt{(E_\nu - \omega)^2 - m^2}$. The difference between the electron and muon mass can therefore affect the phase space available for quasielastic interaction when either the neutrino energy is comparable to the muon mass, or the leptons angle is sufficiently small.

This effect is portrayed in fig. 2.10 The blue regions depict the allowed phase space, as given in eq. (2.14), while the black shaded region is excluded due to Pauli Blocking ($\omega \leq 25$ MeV). The red and blue lines are the allowed kinematics of the muon and electron respectively, as given in eq. (2.16). Solid lines are used for a $5°$, and the dotted lines for $60°$ lepton scattering angles. Here the angles are understood with respect to the neutrino direction. For a neutrino energy of 200 MeV, as seen in (a), the available phase space for the forward scattered events shrinks by around 50% for the electron neutrinos, while for the muon neutrino only around 30% of the phase space has to be disregarded when Pauli Blocking is taken into account. For the high angles, the reduction in phase space is quite similar for both the electron and muon neutrinos.

Therefore the difference in lepton mass affects the angular distribution of the final state lepton. Looking at the region of higher energy at 600 MeV in (b), the high angle events are not affected by the reduction of the phase space, while the low angle events get affected very similarly.

As seen in this example, the available phase space for the lepton mass can depend on the details of the included nuclear effects. In a more general setting, the available Q^2 for the generation of the mass of the lepton is dependent on the state of the struck nucleon. Therefore FSI can directly alter the cross-sections and kinematics of leptons, even though leptons do not rescatter in the nucleus. This especially is important to keep in mind, since the cascade model cannot include these effects, as it can't alter the Q^2 of the interaction in retrospect and is therefore not included in the majority of currently used models. While models based on an effective Hartree-Fock potential try to account for this, have a problem here due to the above-mentioned double counting of the FSI.

2.4 Leptogenesis and Jarlskog Invariant

The T2K and HK experiments try to measure the CP violating phase of the leptonic sector. Besides the fundamental scientific interested in determining one of the SM parameters, the measurement of CP violation would interesting since it could offer a possible explanation for the matter-antimatter asymmetry in the universe. The violation in the leptonic sector can be translated into a baryon asymmetry using leptogenesis [6]. The breaking of CP-symmetry in the leptonic sector is required since in the hadronic sector

the violation is not strong enough to explain the currently observed asymmetry of matter and anti-matter.

In order to infer the δ_{CP} phase one can measure differences in the oscillation probabilities between $\nu_\mu \to \nu_e$ and $\overline{\nu}_\mu \to \overline{\nu}_e$.

$$\Delta\mathcal{P} = \mathcal{P}(\nu_\mu \to \nu_e) - \mathcal{P}(\overline{\nu}_\mu \to \overline{\nu}_e) \tag{2.17}$$
$$= -16\Im\left(U_{e1}U_{\mu 2}U_{\mu 1}^* U_{e1}^*\right) \sin\left(\frac{\Delta m_{32}^2 L}{4E}\right) \sin\left(\frac{\Delta m_{21}^2 L}{4E}\right) \sin\left(\frac{\Delta m_{31}^2 L}{4E}\right).$$

Here $J = \Im\left(U_{e1}U_{\mu 2}U_{\mu 1}^* U_{e1}^*\right)$ is the so-called Jarlskog invariant, which can be expanded and approximated using the current measurement values as

$$J = \frac{1}{8}\cos(\theta_{13})\sin(2\theta_{13})\sin(2\theta_{12})\sin(2\theta_{23})\sin\delta_{CP} \approx 0.034\sin\delta_{CP}. \tag{2.18}$$

As the Jarlskogs invariant is just the imaginary part, which earlier was found to be the reason for a possible CP violation, its vanishing would imply the conservation of the CP symmetry, its violation hence requires all three angles are different from zero and that the masses of the three neutrinos are different. To determine the final value of the Jarlskog invariant, the measurement of the δ_{CP} phase is required.

(a) The effect of Pauli Blocking on neutrinos with an energy of 200 MeV. For small angles the restriction of the allowed phase space after Pauli Blocking with respect to the full phase space is larger as for neutrinos at higher angles. For high angles the electron and muon are similarly restricted in their available phase space, as for low angles the electron's phase space gets reduced stronger than the muons.
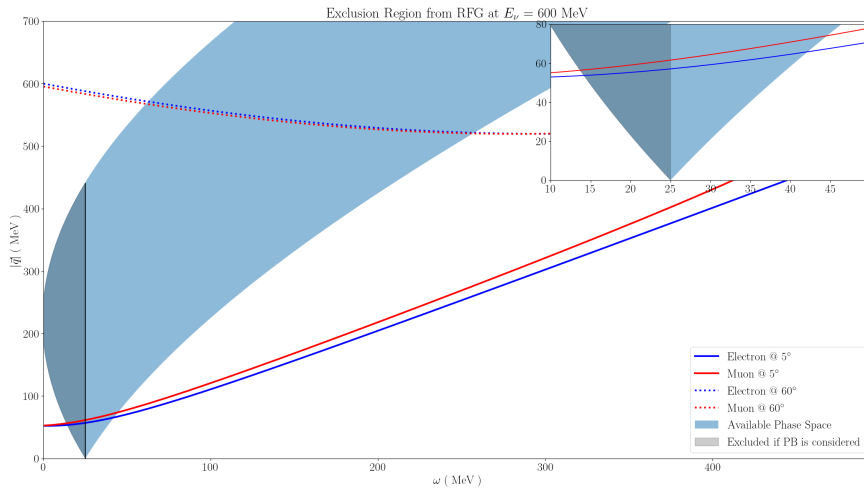
(b) The effect of Pauli Blocking on neutrinos with an energy of 600 MeV. The high angled neutrinos are not affected by the Pauli Blocking while the low angled neutrinos experience a similar restriction in phase space.

Figure 2.10: The restriction of the phase space due to Pauli Blocking for different energies and scattering angles.

2. Neutrino Physics and Oscillations

The T2K and Hyper-K Experiments

Tokai to Kamiokande (T2K) is a long-baseline neutrino-oscillation experiment in Japan, that measures the electron neutrino appearance in a muon neutrino beam. In 2013 T2K reported a signal of electron neutrino appearance events compared to background predictions with a significance of 7.3 σ [5, 18, 19, 20]. The measuremnt of $\theta_{13} \neq 0$ allowed to search for CP violations in the $\nu_\mu \to \nu_e$ appearance channel. Therefore the goal of the T2K experiment is to measure a possible CP violation in neutrino oscillations and perform neutrino intersections cross-section measurements. In this chapter, a short introduction to the setup and main working mechanisms of the T2K experiment and its successor, Hyper-Kamiokande (HK), is given.

A 30 GeV proton beam, produced at the Japan Proton Research Accelerator Complex (J-PARC), impinging on a graphite target, produces a neutrino beam, dominated by muon neutrinos. The mode of the resulting neutrino flux is at around 600 MeV, with an average energy of around 800 MeV. The composition of the flux is then measured at the near detector complex at a distance of 280m from the production point. A second detector is placed at a distance of 295 km, called Super-Kamiokande (SK). The distance is chosen such that the neutrino oscillation probability is maximal. After this distance, in which the neutrino beam travels through the earth, the composition of the beam has changed and is measured at SK. By comparing the neutrino energy spectrum observed at the near- and far-detector, one can infer the oscillation probability and with this the oscillation parameters. In the same way, T2K can use an $\overline{\nu}_\mu$ beam to infer the anti-neutrino oscillation probability. Comparing both of them allows the determination of the δ_{CP} phase as discussed above. A schematic of the T2K experiment is shown in fig. 3.1.

3.1 The Neutrino and Anti-Neutrino Beam

The beam is produced using the shared facilities at J-PARC. In this section, the methods of producing the neutrino beam at the targeted energy are discussed.
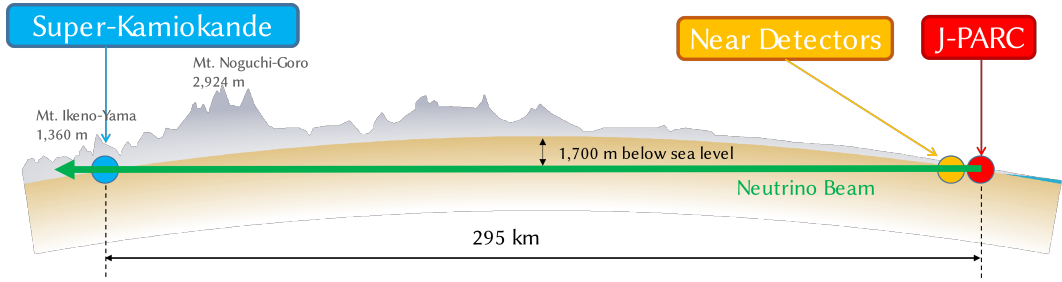
Figure 3.1: Schematic of the T2K experiment in Japan. Taken from the T2K collaboration.

3.1.1 The Beamline

The J-PARC beamline accelerates protons using three accelerators. First H$^-$ are accelerated in a linear accelerator up to 181 MeV. In a second step, charge stripping foils remove the pair of electrons to then inject the protons into a rapid-cycle synchrotron. Here the protons are accelerated to 3 GeV before being handed over to the Main Ring synchrotron. Having reached their final energy of 30 GeV the protons are bent and focused towards the secondary beamline, in which they impinge on a carbon target. This leads to the production of secondary mesons, mainly pions, and kaons. These are focused by a set of magnetic horns, which allows for a selection of positively or negatively charged mesons. This selection dictates the neutrino beam composition, since negatively charged mesons mainly decay in ν_μ, while positively charged ones mainly decay into $\overline{\nu}_\mu$. Depending on the settings of the horn the first selection is called the Forward Horn Current (FHC), while the second selection is titled Reverse Horn Current (RHC).

After being focused, pions and kaons enter a 96m decay tunnel, in which the mesons decay into neutrinos, leptons, and hadrons. A beam dump stops the majority of leptons and hadrons. The high-energy muons which cross the beam dump are detected to monitor the neutrino beam. A schematic of the T2K neutrino beamline is shown in fig. 3.2.

3.1.2 The Off-Axis Method

Using the T2K beamline of 295 km, one finds that the first oscillation maximum occurs at 600 MeV. To tune the beam to this energy, T2K employs the "off-axis angle" technique. Here the beam center is focused 2.5° away from the far detector SK. As described below, the main contribution to the beam comes from the muonic decays of pions. Hence the energy of the neutrino produced in this decay can be determined by

$$E_\nu = \frac{m_\pi^2 - m_\mu^2}{2(E_\pi - p_\pi \cos\theta)}, \quad p_\mu = \sqrt{E_\pi^2 - m_\pi^2}. \tag{3.1}$$

Here m_π and m_μ are the masses of the pion and muon respectively and p_π is the pion's momentum. $\cos\theta$ is the direction of the resulting neutrino with respect to the pions

24
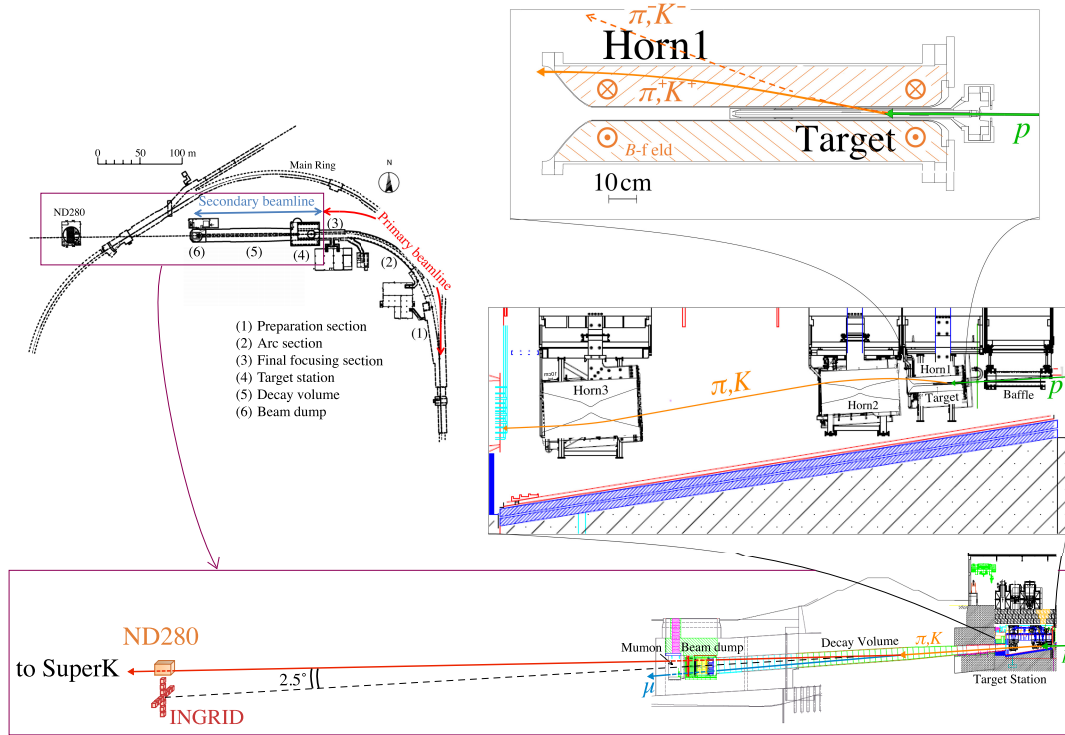
Figure 3.2: A schematic of the T2K beamline at J-PARC. The proton beam from the primary beamline at J-PARC hit the target station, where the interaction with a carbon target leads to the production of pions and kaons. Using magnetic horns a selection between positively and negatively secondaries is possible. These then go through the decay volume where they decay into neutrinos and leptons. The majority of leptons are absorbed in a beam dump, while high energetic muons are detected at Mumon to monitor the beam. At 280 m distance, the INGRID detector is situated, while at the same distance but 2.5 degrees of axis the ND280 detector is placed. Taken from the T2K collaboration.
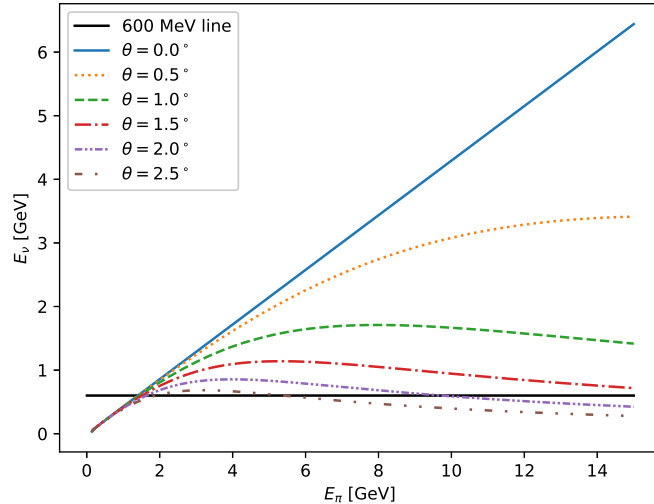
Figure 3.3: Neutrino energy as a function of the pion energy and lepton angle. The off-axis method exploits the narrower distribution of the neutrino energy for higher angles to tune the beam to the preferred energy region.

initial direction. Hence the angle can also be thought of as the angle in reference to the neutrino beam axis. Plotting eq. (3.1), as seen in fig. 3.3, shows that the neutrino energy distribution is strongly affected by the direction. Moving away from the beam center, the energy distribution is narrower and moved to lower energies. This can be used to tune the flux shape of the neutrino beam. For the T2K experiment, the angle used is 2.5°, since this leads to a beam energy of 600 MeV, maximizing the oscillation probabilities at SK. This off-axis method, therefore, focuses the beam to the energy of the oscillation maximum as seen in fig. 3.4. Comparing this with the neutrino cross-section plots, as done in fig. 3.5, the final flux falls in the energy region in which the CCQE cross-section is dominant. This is helpful for the energy reconstruction efforts as discussed earlier.

3.1.3 Beam Composition

A precise knowledge of the flux is required for the determination of the oscillation parameters. The beam is predicted using Monte Carlo simulations, which are tuned to the hadron-production measurements of the NA61/SHINE experiment at CERN.

The main contribution to the flux in the FHC and RHC are

$$\pi^+ \rightarrow \mu^+ + \nu_\mu \text{ (FHC)} \tag{3.2}$$
$$\pi^- \rightarrow \mu^- + \overline{\nu}_\mu \text{ (RHC)}$$

. For energies above 3 GeV, the dominant contributions come from the kaon decays such
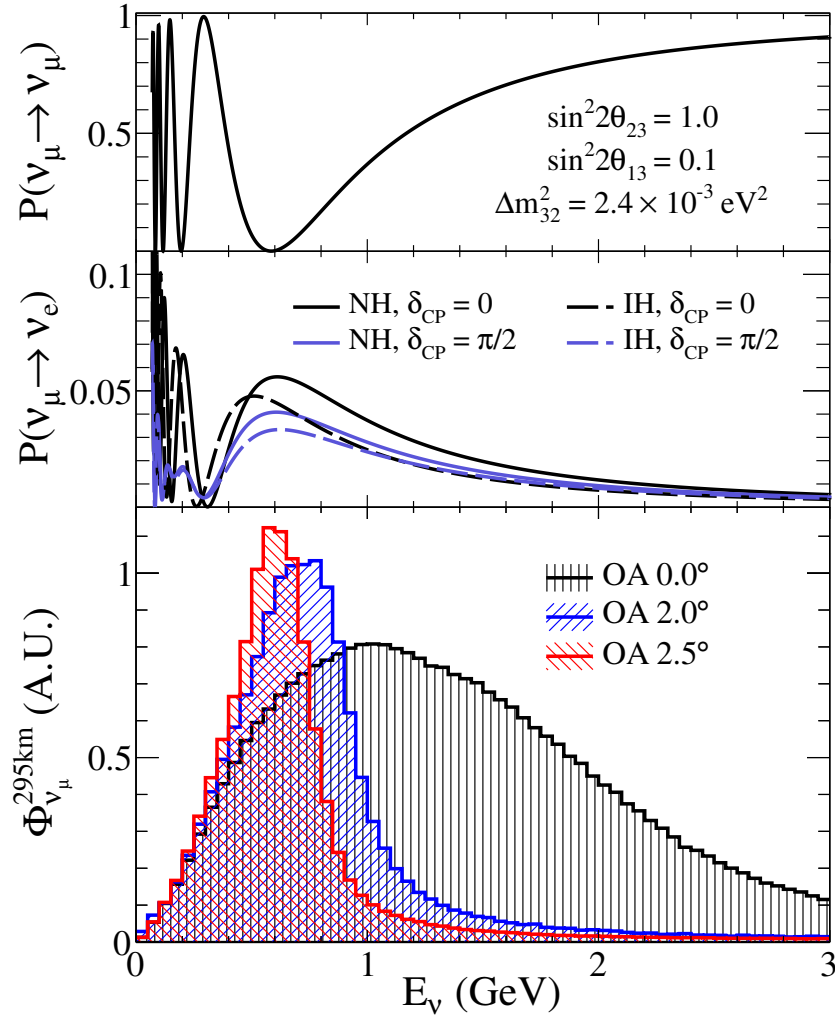
Figure 3.4: The off-axis effect. The flux gets more narrow and the flux peak is moved to lower energies. For the T2K experiment this is done such that the ν_e appearance probability is maximised, while the chanes to have a surviving ν_μ is minimised. Taken from the T2K collaboration.

as

$$
\begin{aligned}
K^+ &\to \mu^+ + \nu_\mu \ (\text{FHC}) \\
K^+ &\to \pi^0 + \mu^+ + \nu_\mu \ (\text{FHC}) \\
K^- &\to \mu^- + \overline{\nu}_\mu \ (\text{RHC}) \\
K^- &\to \pi^0 + \mu^- + \overline{\nu}_\mu \ (\text{RHC})
\end{aligned}
\tag{3.3}
$$

Nonetheless, there is a "wrong-sign" neutrino contamination, which is a contamination of anti-neutrinos in the neutrino beam and vice versa. The reason for the contamination is
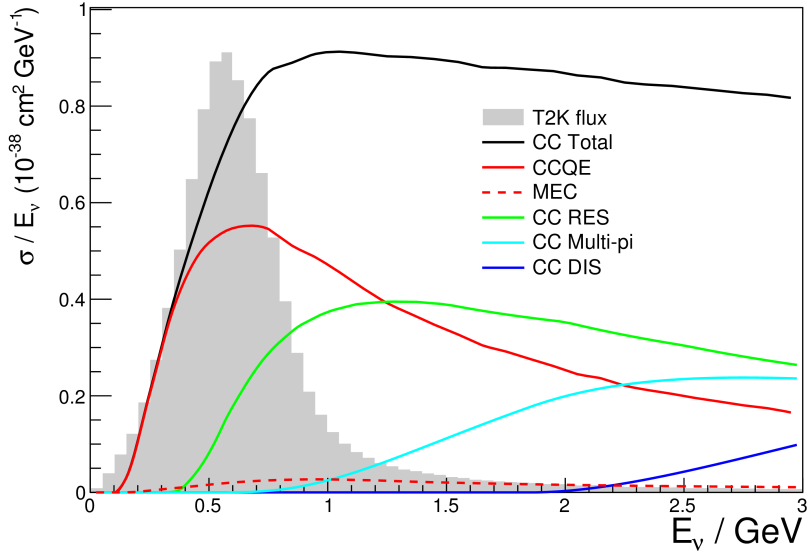
Figure 3.5: The ν_μ T2K flux overlaid with the ν_μ reduced cross-section σ/E_ν, split up in to the different modes. The flux peak is at $E_\nu \approx 600$ MeV. This aligns with the peak in the reduced CCQE cross-section. Taken from the T2K collaboration.

the incomplete focusing of the magnetic horns. Further there is an intrinsic contribution of electron neutrinos due to the electronic decays of pions and kaons

$$
\begin{aligned}
\pi &\rightarrow \mu + \nu_\mu \rightarrow e + \nu_e + \nu_\mu \\
K &\rightarrow e + \nu_e \\
K &\rightarrow \mu + \nu_\mu \rightarrow e + \nu_e + \nu_\mu.
\end{aligned}
\tag{3.4}
$$

The FHC flux can be found in fig. 3.6a, where the predicted flux at the near detector is shown split up into four different flavors. Here the contamination due to the wrong sign and due to the electron neutrinos is visible, but also the flux peak around 600 MeV due to the off-axis configuration. The corresponding plot for the RHC flux is shown in fig. 3.6b, where, again, the contamination of electron anti-neutrinos and the wrong sign is seen. In the RHC operation, the wrong sign contamination is larger due to the higher multiplicities of positive parent particles.

3.2 The Detectors

The T2K experiment uses a variety of detectors and detection techniques. For the near detector complex, there are ND280, INGRID, and WAGASACI-BabyMIND. These are placed at a distance of 280 meters from the neutrino production target. In this section, a short introduction to the main detectors is given and ND280 is discussed in more detail.
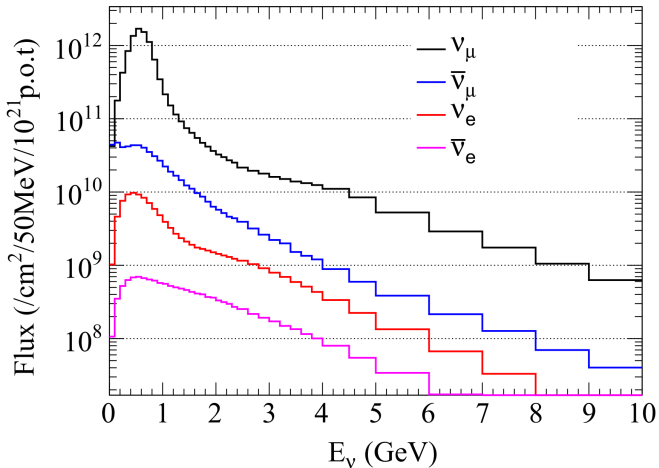
(a) The T2K predicted FHC flux at the near detector ND280. The contamination due to electron neutrinos and wrong sign (anti-neutrinos) can be seen. The flux peaks around 600 MeV. Taken from the T2K Collaboration.
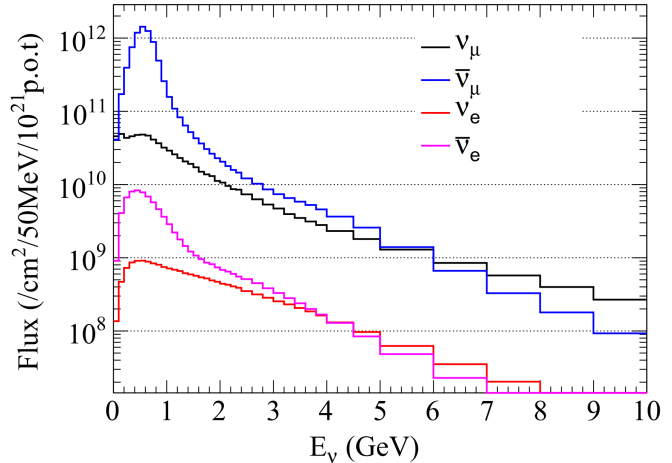
(b) The T2K predicted RHC flux at the near detector ND280. The contamination due to electron anti-neutrinos and wrong sign (neutrinos) can be seen. The flux peaks around 600 MeV. Taken from the T2K Collaboration.

The current far detector SK is discussed to explain the detection principle, further its differences to HK analyzed.

3.2.1 INGRID

INGRID is an on-axis neutrino detector used to monitor the beam position and intensity. It consists of 14 modules, each made up of 9 iron planes sandwiched between plastic scintillating modules. Each module further is encased in veto planes, which reject interactions occurring outside the module itself. Thanks to the high density of iron, it is possible to monitor the neutrino beam closely and with high spatial resolution. This is needed to correctly predict the off-axis angle at ND280.

3.2.2 WAGASCI-BabyMIND

The WAGASCI detector is made of a plastic scintillator that contains water to measure the neutrino cross-section of water. It consists of segmented water and scintillator cells. The BabyMIND spectrometer is made of magnetized iron plates, that allow for muon charge identification, needed to distinguish ν_μ and $\overline{\nu}_\mu$ interactions in WAGASCI.

3.2.3 ND280

The purpose of the ND280 (Near Detector 280m) is to precisely measure the ν and $\overline{\nu}$ energy spectrum. Being at the same off-axis angle as Super-Kamiokande, it is used to

constrain the neutrino flux and cross-section systematic uncertainty in the oscillation analysis at T2K.

The current ND280 consists of several sub-detectors, see fig. 3.7. Two active Fine-Grained Detectors (FGD), three time projection chambers (TPC), both used for the main tracking work. Around these detector elements, the electromagnetic calorimeter (ECAL) identifies electromagnetic showers and reconstructs their energy. Upstream of these detector elements a pion detector (P0D) is located. It observes neutral current interactions including neutral pions in their final state. The overall detector is surrounded by the UA1 magnet, making it possible to reconstruct the particle charge and the momentum in the TPCs. A schematic can be found in fig. 3.7
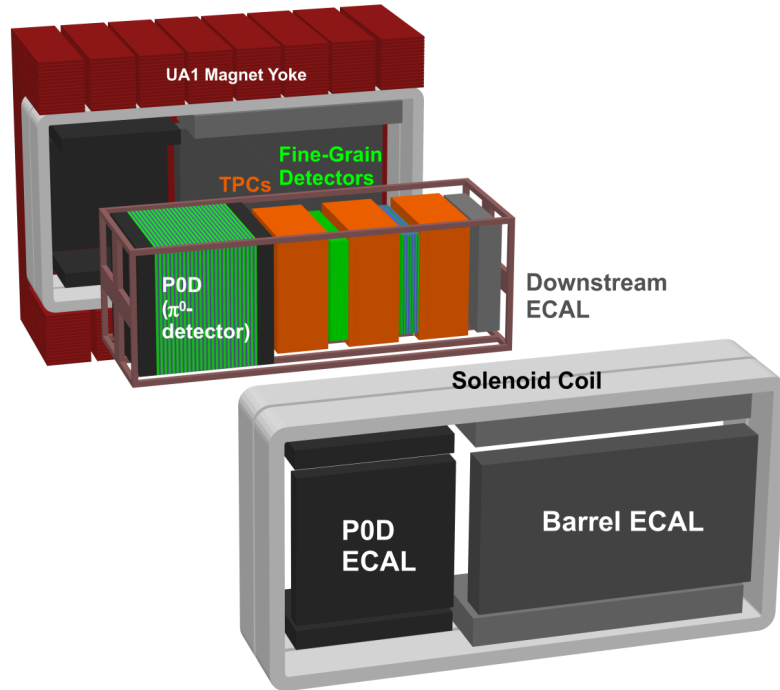
Figure 3.7: Schematic of the ND280 detector of T2K before the update. Taken from the T2K collaboration.

The P0D upstream detector will get replaced in an upgrade by several other detectors [21]. The SuperFGD, a fine-grained detector built out of several scintillator cubes is placed in the middle, sandwiched between two high angel TPCs, to track the final state muons which are ejected at high angles. Around the TPCs, time of flight detectors (ToF) allows for energy reconstruction.
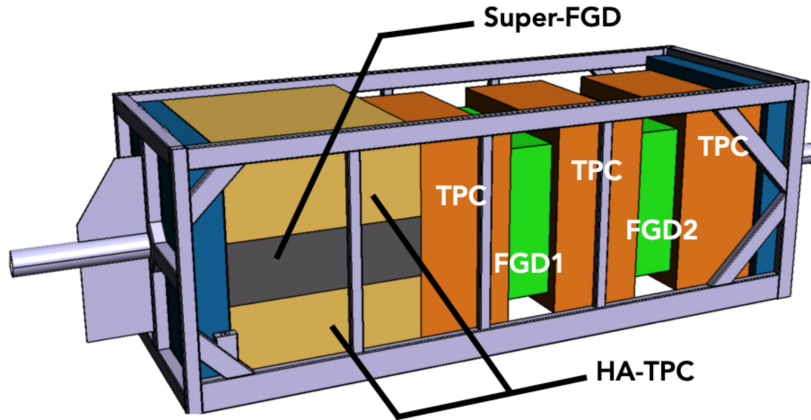
Figure 3.8: Schematic of the upgraded ND280 detector of T2K. Taken from [21].

Fine-Grained Detectors

Choosing the neutrino beam direction as the z axis, the FGDs are made from plastic scintillator bars aligned in either the x or y direction. Each bar has a square cross-section of 9.6mm. 192 such bars are glued to each other to form a plane. FGD1 contains 15 of these XY modules, while FGD2 contains 7. Each scintillator bar contains a hole in which a wavelength shifting fibres (WLS) fiber is situated. These are then read out by Hamamatsu Multiplier Photon Counters (MPPC). The FGD2 further has six thin-walled hollow polycarbonate sheets, which are filled with water, essential to measure neutrino interactions on water. This allows comparing the cross-section differences for carbon and water targets. Each of the FGDs has an active mass of around 1.1 t. This high mass is required to achieve high enough statistics for neutrino oscillation and cross-section measurements

P0D

The P0D consists of tracking planes of scintillator bars, interleaved with lead and brass sheets. Its purpose is to measure neutral current neutrino events on a water target, by measuring the produced π^0 particles

$$\nu_\mu + N \to \mu + N + \pi^0 + X. \tag{3.5}$$

To achieve such, the planes of scintillator bars are additionally interleaved with fillable water targets, the so-called water bags.

Time Projection Chamber

The three TPCs are used for tracking charged particles generated in neutrino interactions in the FGDs. A charged particle passing the gas-filled TPC is ionizing the gas. The

ionization electrons are drifting towards anodes and are detected by Micromega modules. This allows for the measurement of the momenta, charges, and particle types.

Electromagnetic Calorimeter

One electromagnetic calorimeter is surrounding the detector, while a second calorimeter is used at the end as a downstream electromagnetic calorimeter. These are lead-scintillator sampling calorimeters, consisting of bars with a cross-section of 40mm×10mm which are bonded to 1.75 mm thick lead sheets. The role of these lead sheets is to produce showers, which are then in turn measured by the scintillators.

3.2.4 Upgrade of ND280

In order to constrain the uncertainties on neutrino interaction models and cross-sections, T2K is measuring neutrino-nucleus cross-sections by using the ND280 near detector. Using the TPCs and FGDs high masses, it has an excellent capability in measuring and identifying charged particles and their kinematics. Thanks to this, neutrino interactions and their different final state topologies can be studied. The current detector configuration however is limited in acceptance for particles with large scattering angles, as the TPCs are only located at the forward and backward regions of the FGDs. Any event with scattering angles above 40° with respect to the beam axis is not detectable using the current setup. This excludes a large portion of the phase space, a circumstance made worse by the fact, that the far detectors have full angular acceptance. Further, due to the requirement of the current FGDs, that charged particles need a track length of at least 6 cm to be properly reconstructed, ND280 is limited in its efficiency in detecting low momentum particles. For protons, this translates to a momentum threshold of around 600 MeV. Hence a cross-section measurement for events with low momentum final state hadrons is not possible.

As the goal of T2K is to measure the CP violation with a significance above 3 σ, it is important to reduce the systematic uncertainties on the neutrino cross-section, which requires solving the above-mentioned weaknesses. To overcome this limitation, an upgrade to ND280 was proposed [21]. For this, it was decided to replace the P0D with the main target detector, called SuperFGD, two high angles TPCs and ToF sensors. These detectors are explained below.

SuperFGD

The Super Fine Grained Detector (SuperFGD) is built out of about 2 million plastic scintillator cubes with a size of $1 \times 1 \times 1$ cm^3. Due to a surface treatment (chemical etching), they are optically independent. They are connected by three orthogonal WLS. The WLS are then read out at the side of the SuperFGD by Multi-Pixel-Photon Counters. This is schematically depicted in fig. 3.9.

Such a design enables the SuperFGD to detect particles, produced at any angle, reduce proton momentum threshold and detect neutrons efficiently. It also allows for the reconstruction of neutron energies using the time of flight technique. This leads to high efficiency for the full solid angle, while maintaining the high active mass necessary in neutrino experiments. Further, the energy threshold for detection of protons is reduced to around 300 MeV.
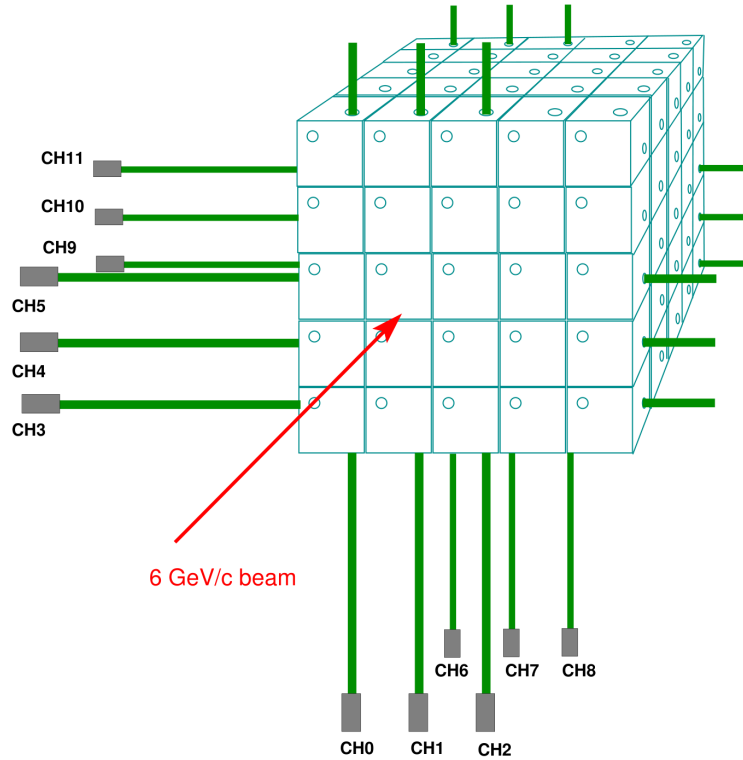
Figure 3.9: Schematic of the assembled cubes in SuperFGD with the WLS fibers. Taken from [22]

HA-TPC

The two High Angle TPCs (HA-TPC) are placed on top and bottom of the SuperFGD. They consist of a gas-tight rectangular box, sub-divided by a central high-voltage cathode. They are read out by eight micromegas on each site.

Time of Flight Sensors

Six time of flight sensors surrounds the SuperFGD and HA-TPCs. The goal of them is to precisely measure the time a charged particle needs to cross the SuperFGD. This is

33
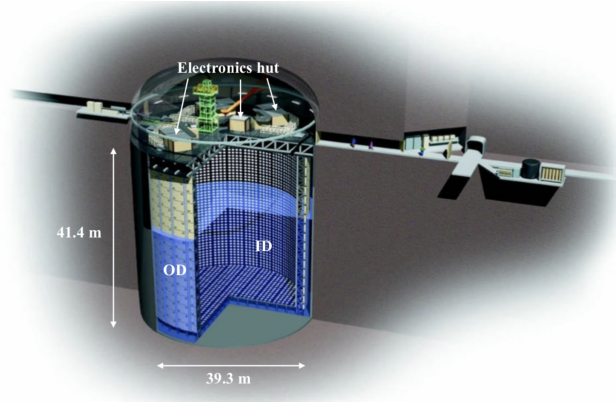
Figure 3.10: Schematic of the Super Kamiokande Detector. Taken from the T2K Collaboration.

used to reject background events based on the direction of the leptons, as well as the reconstruction of the energy of muons. Each module consists of several plastic scintillator bars and fully surrounds the SuperFGD and HA-TPCs.

3.2.5 Super-Kamiokande

Super-Kamiokande (SK) is the far detector of the T2K experiment. It is a 50 kton water Cerenkov detector. The water serves two purposes being the target material for neutrino interactions and producing Cherenkov light when crossed by a relativistic charged particle. The detector volume is divided into two concentric cylinders by a stainless steel framework which is placed approximately 2.5 meters inside the walls of the tank. This structure hosts both inward and outward-looking Photomultiplier Tubes (PMT). The outer cylinder ring acts as a veto against a background like cosmic rays, while the inner part is used for the actual data recording.

If a charged particle transverses a dielectric medium, in this case, ultra-pure water, the medium around is polarized. The excited molecules will decay back to their ground state, sending out photons. These photons form spherical wavefronts, originating from the moving particle. If the speed of the particle is smaller than the speed of light in this medium, the polarization field is approximately symmetric and the light is bunched up. In the case $v \geq c/n$, the polarization field is asymmetric along the direction of travel. This results in overlapping waveforms and constructive interference which leads to the observed cone-like light signal. In water this requires $\beta > 1/n \approx 0.75$, resulting in an energy threshold for electrons of 0.775 MeV, while for muons it is 160 MeV. For the similarly heavy pions, the energy threshold is 211 MeV, while for protons it is at an energy of 1.4 GeV. The UV light is detected by roughly 12.000 PMTs. These allow to reconstruct the light cone direction and the corresponding energy of the particle.

To differentiate muons from electrons, one can use two methods. For low momenta,
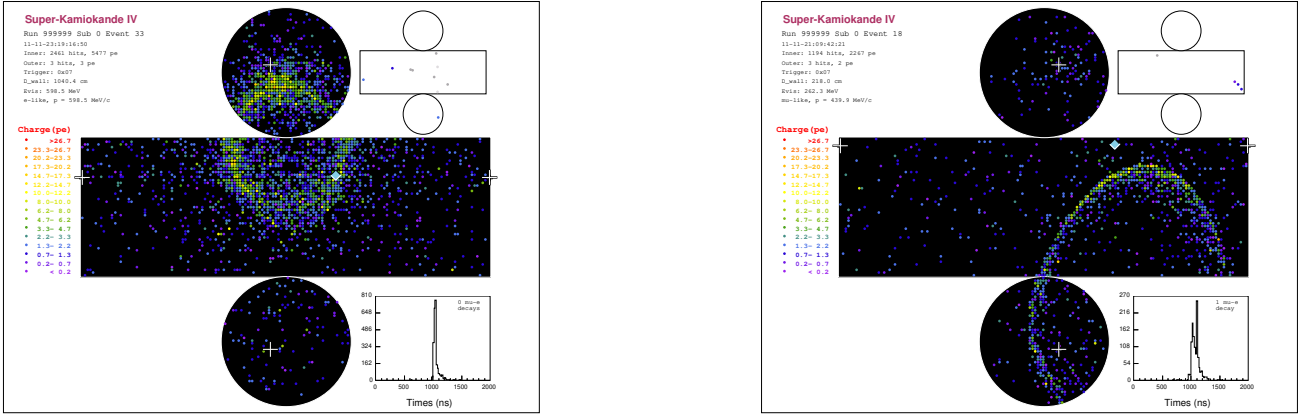
(a) An electron neutrino event in the Super-Kamiokande Detector. The ring has fuzzy edges due to the showering of the electron.

(b) A muon neutrino event in the Super-Kamiokande Detector. The ring is more crisp than for the electron since the muon is a WIMP.

Figure 3.11: Event displays of electron and muon neutrino events in the Super Kamiokande detector. Taken from the T2K collaboration.

the opening angles identify the flavor, since the heavy muons have collapsed rings. Electrons, being much lighter, will form cones with an opening angle that are around $43°$. For high momenta, the fact that electrons produce electromagnetic showers leads to many overlapping rings. These are seen in the detector as one fuzzy ring. Muons form more clearly defined rings, as they do not shower. These differences can be seen in fig. 3.11. On the left, the more fuzzy ring of an electron neutrino interaction is compared to a muon neutrino event on the right.

3.3 Hyper-Kamiokande

For further high-precision neutrino oscillation experiments, the far-detector complex also requires an upgrade. To achieve this, the Super-Kamiokande detector is going to be replaced by the planned Hyper-Kamiokande [23] (HK) detector, based on the same technique. The HK detector is planned to have a cylindrical tank with a diameter of 74 m and a height of 60 m. It will be installed 8 km south of the current SK detector, placing it at the same off-axis angle as the SK site. This cavity will be filled with 258 kt of ultra-pure water. The resulting fiducial volume will be 186 kt, an increase by almost a factor of 9 with respect to SK. Similar to SK, HK is also separated into an inner

detector and an outer detector to veto outside events. The inside of this separating wall will be covered by photo-sensors, each with almost twice the photo-detection efficiency compared to SK's PMTs. This allows tagging the neutrons from $\overline{\nu}_e + p \rightarrow e^+ + n$ events through the neutron capture of hydrogen with the subsequent detection of the 2.2 MeV photon. In the future, a possible Gd doping of the water could increase the neutron tagging efficiency. The tagging of the neutron is important, as the distinction between ν_e and $\overline{\nu}_e$ events is a requirement for the measurement of δ_{CP}.

This experiment will also use the J-PARC neutrino beam, while to get the biggest gain from the upgraded detector, a beam upgrade is performed simultaneously. The aim is to push the beam power from its current 485 kW up to 1.3 MW. This is done by increasing the repetition rate, i.e. the frequency of proton pulses, and the number of protons in each pulse.

As the new far detector increases statistics, the new experiments are expected to be systematically limited. To constraint the systematic uncertainties, the same near detector complex in Tokai is used, with possible upgrades to the near detectors. The further addition of the Intermediate Water Cherenkov Detector (IWCD), placed about 1 km from the neutrino source, will further reduce systematics. The ability of the IWCD to be moved vertically also allows the measurement of varying off-axis angle configurations, effectively probing the energy-dependence of neutrino interactions (νPrism).

To compare how the two far detectors perform, the corresponding exclusion power is shown in fig. 3.12. This plot should be read as the significance to exclude $\sin \delta_{CP} = 0$, assuming a certain true value of δ_{CP}. For the SK far detector, shown in violet as T2K-II, the exclusion power is limited to around 3 σ significance. This exclusion is only achieved for a narrow region of δ_{CP} values. For the HK detector in red, the exclusion power is well above 5 σ for a wide range of δ_{CP} values.

3.4 CP Violation at T2K and HK

As mentioned before, the determination of the CP violating phase of the PMNS matrix can be measured by a comparison of the appearance sample of neutrinos and antineutrinos. Since current neutrino beams with sufficient neutrino energy are muon beams, the search for CP violation is done using the $\nu_\mu \rightarrow \nu_e$ and $\overline{\nu}_\mu \rightarrow \overline{\nu}_e$ samples. In practice, the determination of δ_{CP} relies on a joint fit of the disappearance of the ν_μ and the ν_e appearance. This is done to constrain the oscillation parameters and with this increase the sensitivity of the fit to δ_{CP}.

To determine the oscillation probability P_{osc}, the approximation for the recorded spectrum $N(E_{rec})$

$$N_e(E_{rec}) = \int \Phi(E_\nu) \times \sigma_e(E_\nu, E_{rec}) \times R_{detector}(E_\nu, \sigma, \vec{p}) \times P_{osc}(E_\nu, \nu_\mu \rightarrow \nu_e) \, \mathrm{d}E_\nu. \quad (3.6)$$

shows, that one needs to know the flux Φ, cross-section σ and detector response $R_{detector}$.
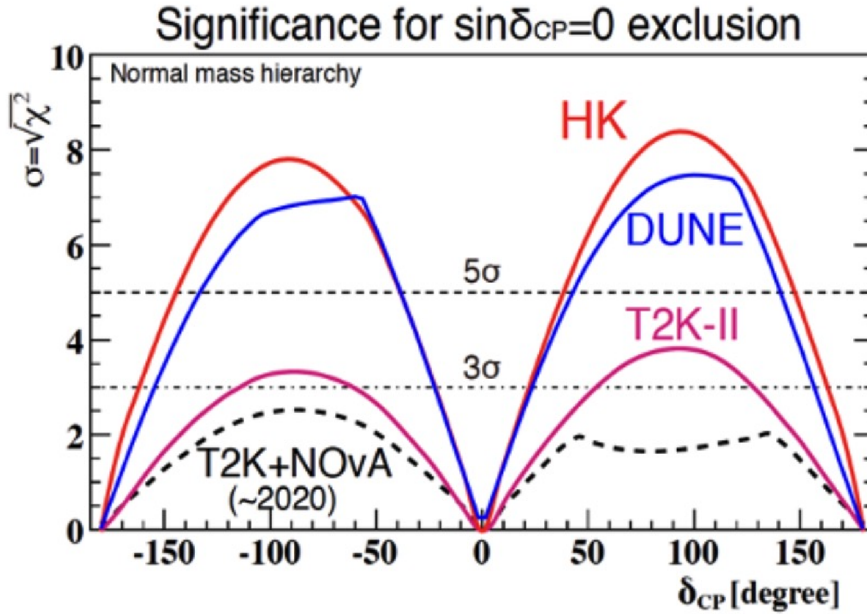
Figure 3.12: The exclusion power for $\delta_{CP} = 0$ for the SK and HK experiments as a function of the assumed true value of δ_{CP}. For the current T2K experiment (T2K-II) using the SK far detector the exclusion line is around $3\,\sigma$. While the exclusion power of HK is well over $5\,\sigma$ in a wide range of δ_{CP} values. Taken from [24].

To constrain the flux and cross-section, near detector and external data are used. Since the flux contains little electron neutrinos, the ND280 detector is statistically limited in the determination of σ_{ν_e}. The overall challenging measurement of the ν_e cross-section is further complicated by a large background of $\pi^0 \to \gamma\gamma$ events to the ν_e interaction topology. ND280, therefore, focuses on measuring the muon-neutrino cross-section and then extrapolating the electron-neutrino cross-section using the theoretical predictions of the cross-section ratio $\sigma_{\nu_e}/\sigma_{\nu_\mu}$ extracted from models. In the case of the current experiment, the used model for this is the SF discussed above. But this extrapolation is highly non-trivial due to the difference in leptons masses and the therefore deviating FSI effects. Since the cross-section is used as a normalization parameter, any uncertainty in this ratio leads directly to an uncertainty on the electron neutrino spectrum and its normalization. When comparing the ν_e and $\bar{\nu}_e$ appearance, this relative normalization is important, as can be seen in the definition of the Jarlkogs invariant. Therefore the predicted cross-section ratio $\sigma_{\nu_e}/\sigma_{\bar{\nu}_e}$ and its uncertainty plays a crucial role.

Using the SK detector, the systematic uncertainties on those cross-section ratios were dominated by the statistical uncertainty of the overall experiment. Looking forward to HK, this is no longer the case. One of the largest systematic uncertainty is the important cross-section ratio $\sigma_{\nu_e}/\sigma_{\bar{\nu}_e}$, i.e. the modeling of the electron-neutrino cross-section. This uncertainty is currently mainly due to radiative corrections as explained below, while the impact of nuclear effects is not yet considered.

3.5 Electron Neutrino Cross-Section

There are several differences between the $\overset{(-)}{\nu}_e$ and $\overset{(-)}{\nu}_\mu$ cross-sections. The most straightforward one is the different kinematic limits due to the difference in the final-state lepton mass. Moreover, additional uncertainties due to radiative corrections and second-class currents need to be taken into account. Radiative corrections enter the cross-section calculations as higher-order terms in perturbation theory [25]. A particle of mass m in a process of energy transfer Q is affected by a term of the order $\frac{\alpha}{\pi} \log \frac{Q}{m}$, which implies strong differences between ν_μ and ν_e due to the difference in mass.

This could be simply calculated, however it is not yet included in the modeling of the cross-sections. But even if these calculations would be included, the modeling may be biased and would need to be validated using a good data sample. To take this into account, a systematic uncertainty is added.

The so-called second class current form factors F_V^3 and F_A^3 are parts in the cross-section parametrisation that appear with a pre-factor of $\left(\frac{m}{M}\right)$. They, therefore, contribute significantly only to the muon cross-section. The existence of these second-class currents requires either charge or time symmetry violation. Since these violations are considered to be small or non-existent, these terms are usually neglected. This leads to an additional systematic uncertainty on $\sigma_{\nu_e}/\sigma_{\nu_\mu}$ and $\sigma_{\overline{\nu}_e}/\sigma_{\overline{\nu}_\mu}$ cross-section ratios. In HK the uncertainties due to second class currents and radiative corrections are assumed to be on the 2% level [26], with a commonly used covariance matrix being

$$V_{e,\overline{e}}^{rad.corr} = \begin{pmatrix} 1.7\%^2 & -0.33 \times 1.7\%^2 \\ -0.33 \times 1.7\%^2 & 1.7\%^2 \end{pmatrix}. \tag{3.7}$$

The resulting uncertainty on the $\nu_e/\overline{\nu}_e$ cross-section ratio is found to be 2.7%.

As discussed above, the initial and final state interactions can affect the Q^2 value of the interaction in a way, that is not yet fully understood. These effects are not trivially calculable and as long as not precisely measured, require approximations and modeling. That this can have a direct impact on the cross-section of electron and muon neutrinos, was earlier demonstrated in the example of Pauli Blocking. Due to the different lepton masses, the extrapolation of the ν_e to ν_μ cross-section is highly non-trivial and is done without sufficient knowledge and understanding of the different impacts of nuclear effects on ν_e and ν_μ interactions. This requires a careful evaluation of the uncertainties connected to this modeling and the inclusion of the corresponding systematics. As this is not done in the current state of the T2K and HK experiments, this thesis aims to determine such an uncertainty and the impact it has on HK's power to exclude the trivial phase hypothesis for δ_{CP}.

Modeling the $\nu_e/\overline{\nu}_e$ Cross-Section Ratio

As mentioned in the previous chapters, knowledge of the cross-section ratio $\sigma_{\nu_e}/\sigma_{\overline{\nu}_e}$ is crucial for determining the extend of CP violation. This is due to the fact, that CP violation would be observed as an asymmetry between the ν_e and $\overline{\nu}_e$ event rate in the far detector. The near detector ND280 constraints the systematic uncertainties related to the neutrino flux and cross-section. Due to the limited statistics for electron neutrinos, their cross-section shall be inferred by extrapolation from the measured muon neutrino cross-section. The cross-section ratio $\sigma_{\nu_e/\nu_\mu} = \frac{d\sigma_{\nu_e}}{d\cos\theta_e} / \frac{d\sigma_{\nu_\mu}}{d\cos_\theta \mu}$ is used (as well as its anti-neutrino counterpart $\sigma_{\overline{\nu}_e/\overline{\nu}_\mu}$) for modeling the ν_e (and $\overline{\nu}_e$) cross-section.

The nominal CCQE cross-section model used in T2K and HK is the Spectral Function [27, 28]. As the discussions in the previous chapters showed, the SF is lacking an accurate prediction of FSI. For T2K this is not a major concern due to the still limited statistics, while it could be for HK. In this chapter, the difference between the SF and other nuclear models are evaluated and a method to set systematic uncertainties for future T2K analyses and CP violation studies at HK are discussed.

4.1 σ_{ν_e/ν_μ} in Hartee-Fock Based Models

In the previous chapter, the effect of Pauli Blocking on the forward scattering region was discussed as an example of how the final state interactions can affect the kinematics of the outgoing lepton. It was shown that if a model includes Pauli Blocking, an increase of the muon neutrino cross-section with respect to the electron neutrino cross-section is expected in the low energy, forward scattering region. A similar effect is discussed in [1]. Here the authors show the impact of the struck nucleons' final wave function on the cross-section ratio. The model used for this is the Continuum Random Phase Space Approximation (CRPA), a Hartree-Fock model including kinematical corrections for the W-boson. Here, the muon neutrino cross-section in the low energy, forward scattered region is considerably larger than the electron neutrino cross-section, opposite to what one expects to see near the kinematic limit for the generation of the muon lepton mass.

This section will show, that the Spectral Function does not predict such a significant increase for σ_{ν_e/ν_μ} as CRPA does. Thus the difference between the σ_{ν_e/ν_μ} predictions for the Spectral Function and the CPRA model is large. Therefore these models are good candidates to evaluate the model dependence of the cross-section ratio. In fig. 4.3a, the ratio of the single differential CCQE cross-section $d\sigma/d\cos\theta_\ell$ between the electron and muon neutrino, as presented in [1], is shown. The region on the bottom left, meaning at angles below 20 degrees and neutrino energies around 200-400 MeV, drops below one. In this region, the CRPA model predicts that the muon neutrino cross-section is larger than the electron neutrino cross-section. At angles below 10 degrees and energies below 300 MeV, the muon neutrino cross-section is double the electron neutrinos. At low energies and angles above 40 degrees, the usually expected ratio is seen, where the electron neutrino cross-section is considerably larger compared to the muon neutrino cross-section.

4.2 Validation of the CRPA Model and Implementation in the T2K Cross-section Modeling Software

In order to compare the CRPA and SF predictions and their impact on T2K, a reproduction of the plot mentioned above and its equivalent for the SF is required. For T2K cross-section modeling, the NEUT Generator (version 5.5.0) is used. As in the latest T2K oscillation analysis, an M_A^{QE} value of 1.21 GeV is assumed. Using 300 million events, distributed over the four neutrino flavours ($\nu_e, \nu_\mu, \overline{\nu}_e, \overline{\nu}_\mu$), a template for $\frac{d^3\sigma}{dE_\nu dp_\ell d\cos\theta_\ell}$ is created, where p_ℓ and θ_ℓ are the momentum and scattering angle of the lepton.

T2K uses a software package called NIWGReWeight for studies of the neutrino cross-section. Here the nominal model, usually the SF, is modified using weights to fit predictions by different models. This is called reweighting. Such methods can then either be used in fake data studies or in the estimation of uncertainties on the cross-section. For this, NIWGReWeight includes hadron tensors calculated for the CRPA model and allows the use of its theoretical cross-section prediction for $\frac{d^2\sigma}{d\cos\theta_\ell dT_\ell}$, where T_ℓ is the kinetic energy of the lepton. To obtain the single differential cross-section $d\sigma/d\cos\theta$, an integration in the leptons kinetic energy T_ℓ is required. In general, a large step-size averages the cross-section over the kinetic energy. This can lead to unreliable predictions. The kinetic energy resolution of the hadron tensors is 1 MeV. To make the cross-section prediction a smooth function, NIWGReWeight uses a two-dimensional interpolation method. Therefore a certain advantage can be gained by using an integration step size below 1 MeV. The step size used was determined by decreasing it, until the predictions of $d\sigma/d\cos\theta_\ell$ did not change significantly anymore when going to smaller values. In the end, 100 keV was determined to be the step-size best suited.

The SF template with its triple-differential cross-section $\frac{d^3\sigma}{dE_\nu dp_\ell d\cos\theta_\ell}$ also requires integration. As the final cross-section $d\sigma/d\cos\theta_\ell$ should be a function of the neutrino energy, it is not possible to integrate out the differential with respect to the neutrino

energy E_ν, as it is done with the lepton's momentum. Instead the total cross-section $\sigma(E_\nu)$ is calculated and the corresponding E_ν slice of $\frac{d^3\sigma}{dE_\nu dp_\ell d\cos\theta_\ell}$ then normalised to fit the prediction of $\sigma(E_\nu)$. This effectively turns the triple-differential cross-section in to the double-differential cross-section $\frac{d^2\sigma}{dp_\ell d\cos\theta_\ell}$ at the energy E_ν. To then determine the step size for the integration in p_ℓ, a similar procedure to the one mentioned above for the CRPA model was used. For more details, especially on the implemented normalization and interpolation on the SF template, see appendix A, where the implementation of a reweighting from SF to several Hartree-Fock based models in to the NIWGReWeight framework is discussed. The results of this reweighting are also discussed in section 4.2.1.

The neutrino cross-sections for the SF and CRPA model can be found in fig. 4.1 and

| (a) σ_e on Carbon | (b) σ_μ on Carbon | (c) Cross-section ratio σ_{ν_e/ν_μ} |
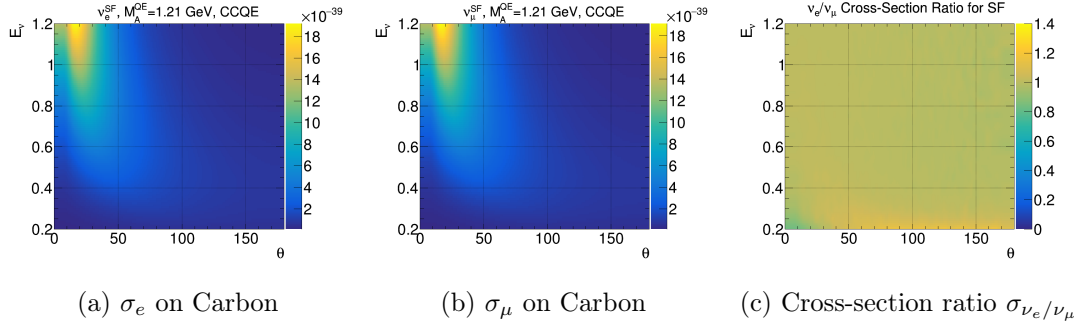
Figure 4.1: The electron and muon neutrino cross-section $\frac{d\sigma}{d\cos\theta}$ on Carbon assuming the Spectral Function with $M_A = 1.21$ GeV. The third plot shows the ratio between the electron and muon neutrino cross-section. It is flatly distributed around 1, with a small electron deficiency in the low energy region.

| (a) σ_e on Carbon | (b) σ_μ on Carbon | (c) Cross-section ratio σ_{ν_e/ν_μ} |
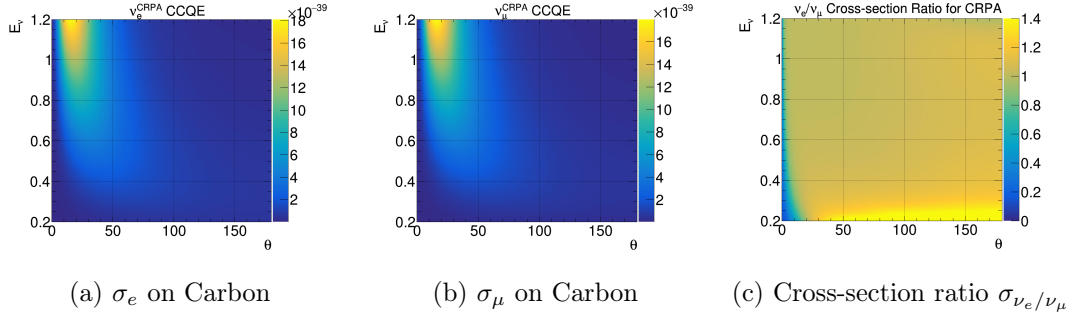
Figure 4.2: The electron and muon neutrino cross-section $\frac{d\sigma}{d\cos\theta}$ on Carbon assuming the CRPA model using the Hadron Tensors. In the third plot the small angle and low energy region clearly shows differences to the SF prediction.

fig. 4.2 respectively, while the anti-neutrino cross-sections and ratios are attached in the appendix in fig. D.1 and fig. D.2. Looking at the fractional cross-section σ_{ν_e/ν_μ} (fig. 4.2c and fig. 4.1c) as a function of the true neutrino energy and the true lepton angle, the difference between the SF and CRPA models is visible. While the former is mostly

constant in the forward scattered region, the latter clearly shows a dominance of the muon cross-section over the electron in this region of the phase space.

(a) The cross-section ratio from [1]

(b) Reproduction of the cross-section
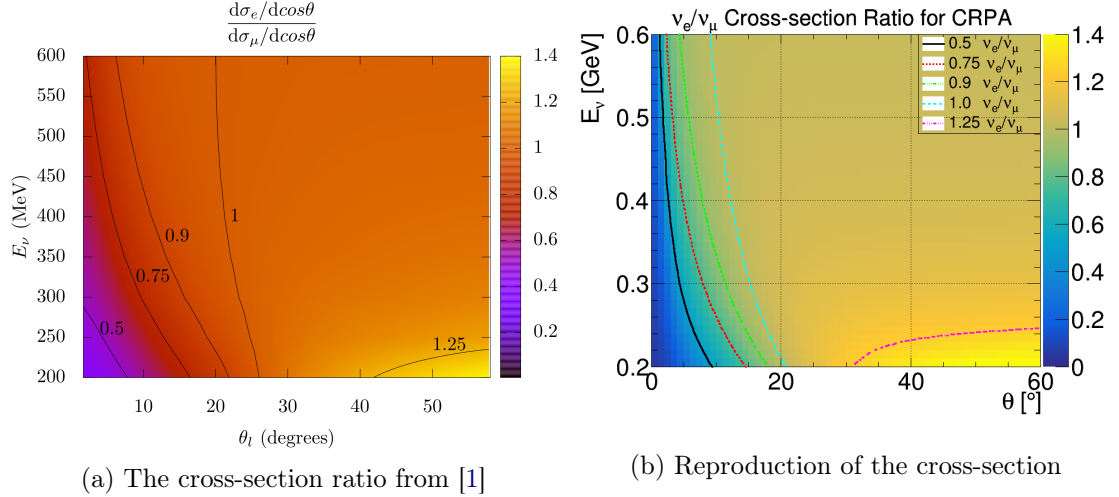
Figure 4.3: The cross-section ratio for the forward angled region compared between the hadron tensors in NIWGReWeight and the paper by [1]. Both plots use lines corresponding to fixed values of σ_{ν_e/ν_μ}. The model underwent modifications between the time of the initial publishing of [1] and the writing of this thesis. These changes lead to a change in the shape of the isolines.

A comparison between the CRPA cross-section ratio obtained from the hadron tensors and the one from [1] can be found in fig. 4.3. Here both plots use lines at constant values of σ_{ν_e/ν_μ}, called isolines. The values are chosen to be at 0.5, 0.75, 0.9, 1.0 and 1.25, as in [1]. Differences between fig. 4.3a and fig. 4.3b are due to updates applied to the model since it was published in 2019. Due to this, the shape of the isolines changed. The affected angular region is smaller, the isoline corresponding to a ratio equal to 1 starts at roughly 20 degrees, instead of approximately 25 degrees as in the original CRPA model. The overall prediction of the increased cross-section for muons at low angles remains. Overall, the differences between the SF and CRPA model stay large. As the predictions of these two models deviate from each other, this forms a good foundation to evaluate the model-dependence of the cross-section ratio σ_{ν_e/ν_μ}.

4.2.1 Evaluation of Model Differences using NIWGReWeight

In the framework of the NIWGReWeight software package, a reweighting between the SF and several Hartree-Fock based models was implemented. This was done to enable a fake data study and to have a direct way to evaluate the differences amid models. This section summarizes the findings of this study, while the technical implementation and its evaluation are discussed in appendix A and a technical note for T2K (T2K-TN-434).

To evaluate the differences between the CRPA and SF models, the muon neutrino flux at ND280 is used. A set of roughly five million muon neutrino events was generated using NEUT's SF on Carbon. These were then reweighted using the newly implemented method in NIWGReWeight to match the predictions of a combination of the CRPA and SuSAv2 models. The combination of both models is required, as the hadron tensors for CRPA only allow q_0 and q_3 values up to 1 GeV. The hybrid model extends this range up to 2 GeV. However, most of the events will fall in the region of phase space, where the CRPA tensors are used. Details on the combination of both models can be found in appendix A.2.2. For easier readability, in this section CRPA will refer to this CRPA-SuSAv2 Hybrid model.

In fig. 4.4, four variables are compared between the SF and CRPA muon-neutrino cross-section predictions. The predictions of the SF are shown in black, while the predictions with the applied reweighting are shown in blue. On the top, the plots depict the distribution of the corresponding variable, while the bottom shows the ratio between the SF and CRPA predictions.

Figure 4.4a shows the distribution of the energy transfer q_0. Here the main difference between the SF and CRPA model is an increase in the event rate of about 10% at the low end of the spectrum. At q_0 values above 120 MeV, the CRPA model predicts a decrease in events. The ratio drops down to around 0.8 at 240 to 360 MeV and then goes back up to 1 at around 1.2 GeV.

Looking at fig. 4.4b, which shows the distribution of the momentum transfer q_3, the ratio in the first bin is at roughly 0.45, meaning that the very low q_3 region is depleted. The intermediate region is around one, while the ratio again drops by 20% at around 1 GeV.

To see how these changes affect the recorded spectrum, one needs to know the connection between the lepton scattering angle and the kinematic variables q_0 and q_3. Assuming a pure CCQE interaction, a short calculation shows

$$T_\ell(q_0, q_3, E_\nu) = E_\nu - q_0 - m_\ell$$
$$\cos \theta_\ell(q_0, q_3, E_\nu) = \frac{T_\ell + m_\ell - \frac{q_3^2 - q_0^2 + m_\ell^2}{2 E_\nu}}{\sqrt{(T_\ell + m_\ell)^2 - m_\ell^2}}, \tag{4.1}$$

where m_ℓ is the corresponding mass of the lepton and T_ℓ its kinetic energy. In fig. 4.5 the muon scattering angle at an energy of $E_\nu = 800$ MeV, is shown as a function of q_0 and q_3. As an extended flux is compared to a mono-energetic assumption in the calculation of $\cos \theta$, the comparison is not perfect, but an increase in low q_0 events generally shows an increase in forward scattered events. As the CRPA model further decreases the number of events with q_3 values higher than 240 MeV, a larger fraction of events end up in the lower left region of the phase space, which corresponds to an increase in forward scattered events.

In fig. 4.4c the change in the energy-momentum transfer is shown. Over the whole

(a) Energy transfer q_0

(b) Momentum transfer q_3

(c) Energy-momentum transfer Q^2

(d) Energy reconstruction bias $E_\nu^{\text{CCQE}}/E_\nu - 1$
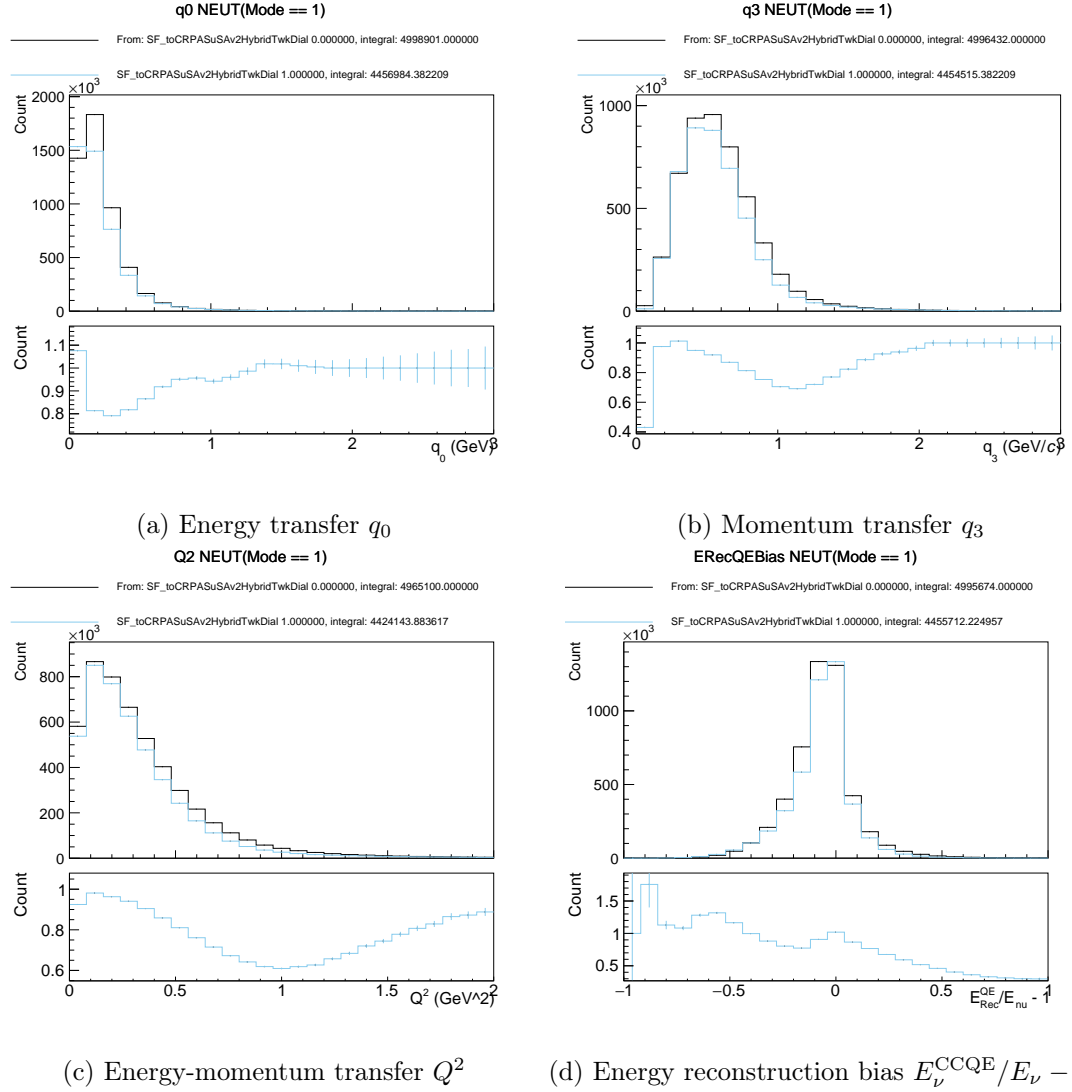
Figure 4.4: A comparison between different predictions between the SF and the CRPA model for muon neutrinos following the T2K ND280 flux. The black line shows the prediction of the SF model, while the blue line shows the results after reweighting, meaning for CRPA. The upper part shows the distribution of the corresponding variable (fig. 4.4a q_0, fig. 4.4b q_3, fig. 4.4c Q^2, fig. 4.4d Energy reconstruction bias). The lower part shows the ratio between the SF and the CRPA predictions.
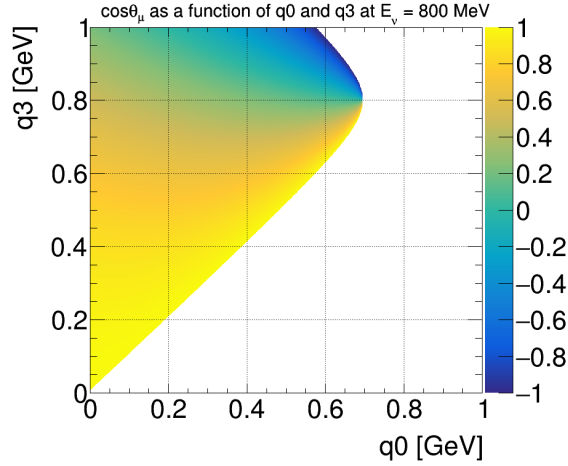
Figure 4.5: The scattering angle of the muon in a CCQE event at $E_\nu = 800$ MeV as a function of q_0 and q_3. The white region is the disallowed part of the phase space.

range of Q^2 values, the CRPA model predicts a smaller event rate compared to the SF. The largest differences are around 1 GeV, where the ratio between them drops as low as 0.6.

The difference in the energy-reconstruction bias $\frac{E_\nu^{\mathrm{CCQE}} - E_\nu^{\mathrm{true}}}{E_\nu^{\mathrm{true}}}$ is also interest, as the uncertainty in the energy reconstruction also influences the recorded energy spectrum. This is depicted in fig. 4.4d. The distribution is narrower for CRPA compared to the SF. Therefore the overall reconstruction bias is smaller.

4.2.2 Carbon and Oxygen

The original CRPA article [1] discussed the cross-section for neutrino-carbon interactions. Since the T2K near detector mainly consists of plastics, which are made out of Carbon and Hydrogen, while the far detector is a water-based tank, the differences between Carbon and Oxygen are of interest. In NIWGReWeight the hadron tensors for CRPA exist for Carbon, Oxygen, and Argon.

Therefore the cross-section ratio was evaluated for three different targets. The results can be found in fig. 4.6. Interestingly, the increased muon neutrino cross-section at low angles seems to be large in Carbon and Oxygen, but small in Argon, a heavier nucleus. This is contrary to what could be naively expected. Nonetheless, σ_{ν_e/ν_μ} is very similar for Oxygen and Carbon. To evaluate the differences, the ratio between the Carbon and Oxygen $\sigma_{\nu_e/\nu_\mu}^{O/C}$ predictions per nucleon is shown in fig. 4.7. In this comparison, the bright yellow region shows that only the very forward scattered events, with angles below 7 degrees, have a difference larger than 1% between Carbon and Oxygen. In this region, $\sigma_{\nu_e/\nu_\mu}^{O/C}$ is larger than 1, meaning that the cross-section ratio for Oxygen is larger than

(a) Carbon   (b) Oxygen   (c) Argon
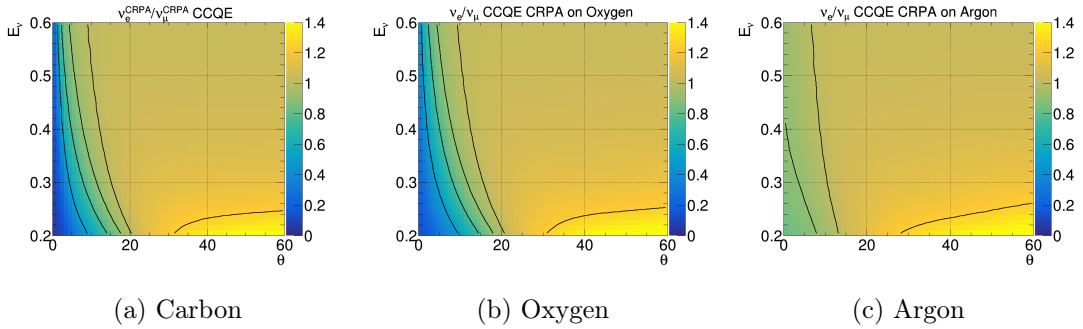
Figure 4.6: The CRPA cross-section ratio for different target materials. The isolines on all three plots are drawn for $\sigma_{\nu_e/\nu_\mu} = 0.5,\ 0.75,\ 0.9,\ 1.0,$ and 1.25. For Argon only the last three are visible. The Carbon and Oxygen cross-section ratios are similar on value and shape, while on Argon the shape and values differ dramatically from the ones on the smaller nuclei.
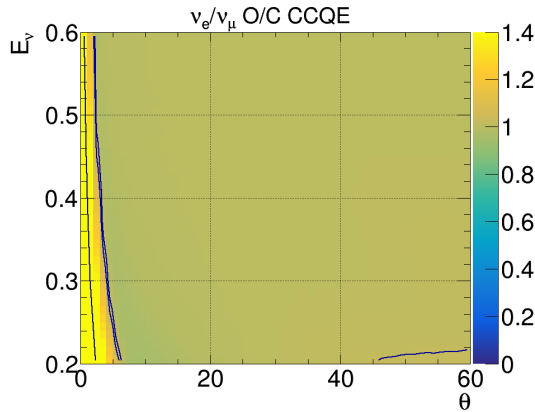
Figure 4.7: The fractional difference between the CRPA cross-section ratio σ_{ν_e/ν_μ} predicted in Oxygen and Carbon, $\sigma_{\nu_e/\nu_\mu}^{O^{16}}/\sigma_{\nu_e/\nu_\mu}^{C^{12}}$. Isolines are drawn at O/C $= 1.01,\ 1.05$ and 1.8. Only the very forward scattered region shows a difference of more than 1%. Here Oxygen has a larger cross-section ratio σ_{ν_e/ν_μ}, meaning the forward scattered region is flatter compared to Carbon.

for Carbon. The trend is also observed by comparing Carbon with Argon, although here the effect is much stronger. It seems that heavier nuclei are less affected by the model differences between CRPA and SF, compared to lighter ones.

A possible explanation is found in the q_0 dependence of σ_{ν_e/ν_μ}. At very low q_0, meaning at energy transfers below 15 MeV, theoretical predictions show that $\sigma_{\nu_e/\nu_\mu} \geq 1$, while at intermediate energy transfers the increased muon-neutrino cross-section starts to appear with $\sigma_{\nu_e/\nu_\mu} \leq 1$. This very low energy transfer region is not accessible to interactions on Carbon, since the nucleons in the p-shell, with the lowest removal energy,

still require energy transfers that fall in the region where a cross-section ratio below 1 is expected. In Argon, on the other hand, the p-shell has lower removal energy, therefore making the region of very low q_0 interaction accessible. This therefore could cancel out the effect leading to $\sigma_{\nu_e/\nu_\mu} \leq 1$ seen at low to intermediate q_0 regions. However, this is not yet fully understood and verified, so more work on the impact of the nuclear potential and its contribution to the muon dominance is needed for a satisfying understanding.

4.2.3 The forward scattered region and its impact for T2K

To evaluate how the forward scattered region affects the T2K experiment, it is necessary to know how much of the phase space covered by the T2K flux lies inside the region where the CRPA model predicts the muon-neutrino cross-section to be larger than the electron neutrino one. In order to visualize this, the isolines in Carbon of fig. 4.3b are overlaid to the muon neutrino flux at ND280, and the isolines in Oxygen to the $\nu_\mu \rightarrow \nu_e$ flux expected at HK. In both cases, only a small fraction of events fall in the region where CRPA predicts σ_{ν_e/ν_μ} to be smaller than 1.
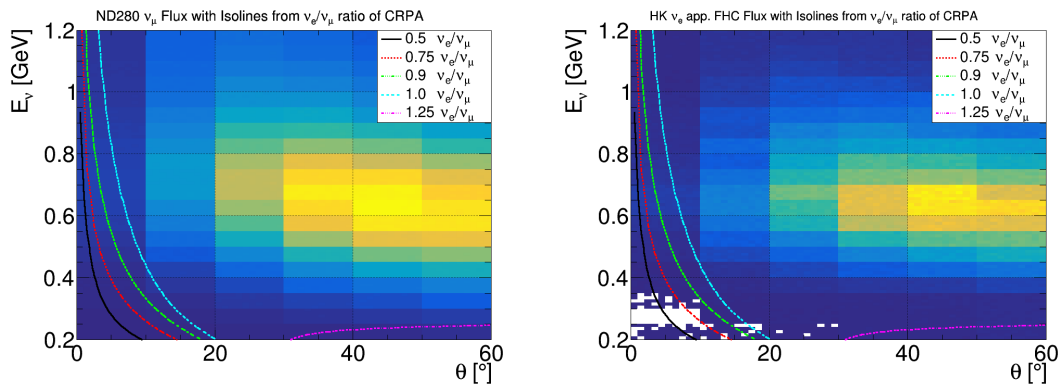
(a) ND280 flux overlaid with cross-section ratio isolines

(b) SK oscillated flux overlaid with cross-section ratio isolines

Figure 4.8: The flux at ND280 and HK overlayed with the isolines of the cross-section ratio of CRPA. For the ND280 flux the Carbon isolines , while for HK the ones on Oxygen are used. In both cases only a very small region of the phase space covered by the flux falls in the region of the muon dominance.

A more quantitative version of this is presented in table 4.1. These tables show the fraction of events of the predicted oscillated flux at HK that falls in the region where the fractional cross-section σ_{ν_e/ν_μ} drops below a certain value. First the total region $E_\nu \in (0.2, 1.2)$ GeV and $\theta \in (0, 180)°$ is considered and later the forward scattered region with angles below 20 degrees. This energy range is chosen as the region, in which the T2K oscillation analysis is performed. Within the full phase space, only 0.5% of events have a ratio below 1. When looking at a fractional cross-section that deviates more than

σ_{ν_e/ν_μ} at Hyper-K			σ_{ν_e/ν_μ} at ND280		
$E_\nu[GeV] \in (0.2, 1.2), \theta[°] \in$	$(0, 180)$	$(0, 20)$	$E_\nu[GeV] \in (0.2, 1.2), \theta[°] \in$	$(0,180)$	$(0,20)$
< 1	0.5%	6%	< 1	1.1%	4%
< 0.98	0.02%	2.5%	< 0.98	0.04%	1.4%
< 0.97	0.01%	1.8%	< 0.97	0.03%	1.0%
< 0.9	0.003%	0.4%	< 0.9	0.007%	0.3%
< 0.7	5e-5%	0.04%	< 0.7	1e-4%	0.05%

Table 4.1: Fraction of events of the expected HyperK (left) and ND280 (right) ν_e spectrum falling into the region of a given cross-section ratio. In all cases, the full energy range of 200 MeV up to 1.2 GeV is considered. In the first column, the full angular region is considered, while in the second only the forward scattered region of angles below 20 degrees.

2% from 1, this number reduces to only 0.02%. This means that only 0.02% of events fall in a region, where the CRPA model predicts an increased muon neutrino cross-section and with this, the biggest difference to the SF. Focusing on the forward scattered region with angles below 20 degrees, this number, as expected grows. But even in this case only approximately 3% of the events that lie in this region and have energy relevant for the oscillating analysis fall more than 2% below 1. Very similar numbers hold for the flux at ND280.

This shows that the part of the phase space affected by the increased muon-neutrino cross-section, and the T2K/HK flux does not have a significant overlap. As this is the largest deviation between the prediction of the CRPA model compared to the SF, the impact on the T2K and HK experiments due to this specific difference is expected to be small. A more systematic evaluation is done in the next section.

4.3 Evaluation of the full Phase Space

Having seen that σ_{ν_e/ν_μ} in the forward-angle region does not significantly impact the T2K flux, the remaining question is how different models, like CRPA and SF, predict the cross-section ratio on the whole phase space.

Therefore the Carbon cross-section ratio $\sigma_{\nu_e}/\sigma_{\nu_\mu}$ is calculated for both the SF and the CRPA model as a function of the phase space in neutrino energy E_ν and the lepton scattering angle θ. The results are then divided to get the fractional difference between them, yielding $\sigma_{\nu_e/\nu_\mu}^{SF/CRPA} = \sigma_{\nu_e/\nu_\mu}^{SF}/\sigma_{\nu_e/\nu_\mu}^{CRPA}$.

In fig. 4.9 the results for the neutrinos and anti-neutrinos can be found. If the result would be completely flat with a value of one, the cross-section ratio would be identical for both models, while a value of 1.02 or 0.98 both resemble a deviation of 2% between the

CRPA model and the Spectral Function. The region inside the black isolines corresponds to the part of the phase-space where the difference between both models is smaller than 2%. Similarly, the region inside the red, blue, or green isolines corresponds to a difference of 3, 4, and 5%.

The largest difference between the SF and CRPA model are the ones evaluated above in the forward scattering region with angles around 20 degrees. As this part of the phase space is only very sparsely populated by the HK flux, these differences do not play a major role. The region at higher scattering angles could have a larger impact. This can be seen in the fact that the isolines in the middle of the phase space show that the region with scattering angles above 100 degrees suffers from differences larger than 5% for both the neutrino and anti-neutrino. For anti-neutrinos a surprising structure at 400 MeV and angles larger than 150 degrees is observed in fig. 4.9b. This is due to a decrease in σ_{ν_e/ν_μ} in the CRPA model. A closer look into the details of the CRPA model would be necessary to understand its origin.

(a) Neutrinos
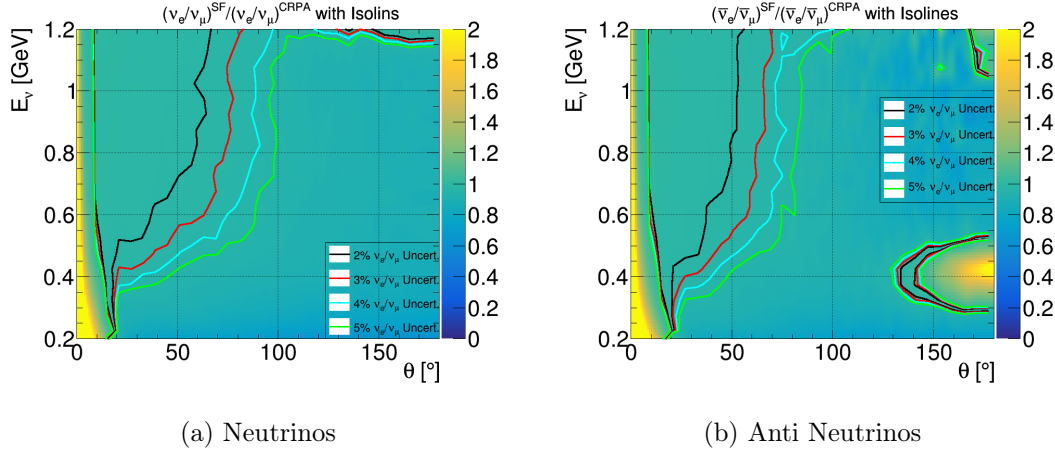
(b) Anti Neutrinos

Figure 4.9: The fractional difference in the cross-section ratio between the CRPA model and the SF prediction for the neutrino $\sigma_{\nu_e/\nu_\mu}^{SF/CRPA}$ and anti-neutrino $\sigma_{\bar{\nu}_e/\bar{\nu}_\mu}^{SF/CRPA}$ case. The isolines correspond to a deviation of 2,3,4, and 5%.

Further, at energies above 0.6 GeV and angles larger than $100°$ certain fluctuations are visible in this plot. They originate from the SF template, which shows a non-flat distribution of the cross-section ratio in this region. Even with a coarser (E_ν, θ) binning, this region stays above a 5% deviation.

For given neutrino energy, the angular region where $\sigma_{\nu_e/\nu_\mu}^{SF/CRPA}$ deviates from 1 by less than 2% is narrower for anti-neutrinos than it is for neutrinos. This means that anti-neutrinos are more strongly affected by the discrepancies between these two models than neutrinos are.

The large differences between CRPA and SF models come from both the region at low energies and at large lepton scattering angles. A possible reason could be that most of

4. Modeling the $\nu_e/\overline{\nu}_e$ Cross-Section Ratio

4. Modeling the $\nu_e/\overline{\nu}_e$ Cross-Section Ratio

the models are mainly tuned on the forward scattering region data, while the backward scattered region suffers from less accurate data. Therefore the discrepancy between the two models may decrease in the future if more data becomes available to better tune the whole phase space.

Nonetheless, the two models predict a non-trivial discrepancy in their cross-section ratio, whose effect on the T2K experiment shall be further evaluated. Hence, $\sigma_{\nu_e/\nu_\mu}^{SF/CRPA}$ was compared to the T2K neutrino flux in fig. 4.10. The oscillated $\nu_\mu \to \nu_e$ flux peaks
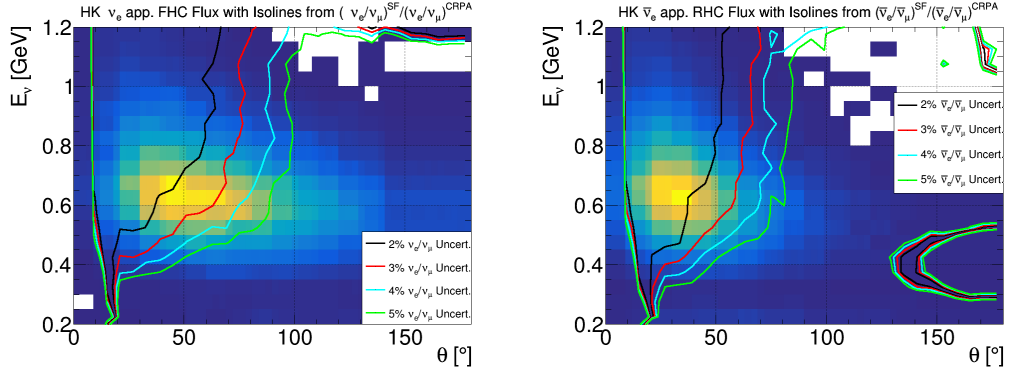
(a) $\nu_\mu \to \nu_e$ flux at SK overlaid with the deviations of the neutrino cross-section ratio

(b) $\overline{\nu}_\mu \to \overline{\nu}_e$ flux at SK overlaid with the deviations of the anti-neutrino cross-section ratio

Figure 4.10: The expected oscillated (anti-)neutrino flux at SK overlaid with isolines corresponding to a deviation of the cross-section ratio between CRPA and SF of 2,3,4, and 5%.

between 600-700 MeV with an angle around 50°. Therefore, the isolines corresponding to 2% and 3% deviations cross the peak region of the flux. Even the 4% and 5% isolines wrap around the region where the flux is still relatively high.

As mentioned above, for anti-neutrinos a larger difference between CRPA and SF is observed. However, the $\overline{\nu}_\mu \to \overline{\nu}_e$ oscillated flux has a narrower peak compared to the flux peak of $\nu_\mu \to \nu_e$. Therefore only the isoline corresponding to a 2% deviation cuts through this peak region, while the 3,4 and 5% lines are already wrapped around the peak. Hence a smaller total uncertainty is expected on the cross-section ratio $\sigma_{\overline{\nu}_e/\overline{\nu}_\mu}$.

The event rate at HK and T2K is compared to the σ_{ν_e/ν_μ} uncertainty in table 4.2. The Full Space column corresponds to the full phase space between 200 MeV and 1.2 GeV and lepton angles between 0 and 180°. Only around 29% of the total number of events are included in the region with a discrepancy of less than 2% for the neutrino flux, while for the anti-neutrinos this number increases up to 80%. The 5% cross-section ratio still excludes around 28% of the neutrino events, while only 8% of the anti-neutrino events are affected by deviations larger than this. The forward scattered region corresponds to an angle smaller than 60 degrees. In this region, the number of events that fall in the corresponding region is higher, since the region with a large uncertainty is left out. This

σ_{ν_e/ν_μ}	Full Space	Forward Angles	$E_\nu \geq 0.4$ GeV	$\sigma_{\overline{\nu}_e/\overline{\nu}_\mu}$	Full Space	Forward Angles	$E_\nu \geq 0.4$ GeV
1%	0.09	0.19	0.09	1 %	0.68	0.87	0.68
2%	0.29	0.60	0.29	2 %	0.80	0.97	0.80
3%	0.49	0.89	0.49	3 %	0.86	0.998	0.86
4%	0.62	0.96	0.63	4 %	0.89	0.999	0.90
5%	0.72	0.98	0.73	5 %	0.92	0.999	0.92

Table 4.2: The Fraction of events of the expected recorded HK spectrum falling in the region covered by the given uncertainty on the ν_e/ν_μ and $\overline{\nu}_e/\overline{\nu}_\mu$ cross-section ratios. The column labeled Full considered the full phase space with energies between 200 MeV and 1.2 GeV and the full angular range. The one labeled forward only looks at events in the forward scattered region, meaning angles below 20 degrees and again the full energy range of 200 MeV up to 1.2 GeV. The last column restricts the energy to 400 MeV. The anti-neutrino cross-section ratio has a smaller uncertainty connected to it compared to the neutrino cross-section ratio.

affects the numbers corresponding to the 5% deviations the most, seeing an improvement of almost 28% in the neutrino case.

The high energy column corresponds to events with an energy above 400 MeV, while allowing all angles. Here the numbers are closer to the full phase space than to the forward scattered region. In total the two models show considerable differences between each other. The largest differences are in the forward scattered region, while the ones affecting T2K the most, are in the backward scattered region.

4.4 Systematic Uncertainty on $\sigma_{\nu_e/\overline{\nu}_e}$

Above it was shown that it is necessary to include an uncertainty due to the different predictions by the SF and CPRA model. This section focuses on a definition of such an uncertainty. It further gives a retrospect justification for focusing on these two models for the evaluation of a nuclear effect systematic uncertainty.

Above the deviations on the cross-section ratios σ_{ν_e/ν_μ} where investigated. For the T2K experiment a covariance matrix between σ_{ν_e/ν_μ} and $\sigma_{\overline{\nu}_e/\overline{\nu}_\mu}$ is required, from which the uncertainty on $\sigma_{\nu_e/\overline{\nu}_e}$ is determined. To calculate the covariance matrix the standard formula

$$C_{i,j} = (X_i - \mathbb{E}(X_i))(X_j - \mathbb{E}(X_j)) \tag{4.2}$$

is used. As the calculation only includes two models, the diagonal elements corresponding to the uncertainty on σ_{ν_e/ν_μ} and $\sigma_{\overline{\nu}_e/\overline{\nu}_\mu}$ are calculated as

$$C_{\nu_e/\nu_\mu} = (\sigma_{\nu_e/\nu_\mu}^{\text{Model 1}} - \sigma_{\nu_e/\nu_\mu}^{\text{Model 2}})^2, \qquad C_{\overline{\nu}_e/\overline{\nu}_\mu} = (\sigma_{\overline{\nu}_e/\overline{\nu}_\mu}^{\text{Model 1}} - \sigma_{\overline{\nu}_e/\overline{\nu}_\mu}^{\text{Model 2}})^2. \tag{4.3}$$

The off-diagonal terms, which are used to determine the correlation are given by

$$C_{\nu_e/\nu_\mu,\,\overline{\nu}_e/\overline{\nu}_\mu} = (\sigma_{\nu_e/\nu_\mu}^{\text{Model 1}} - \sigma_{\nu_e/\nu_\mu}^{\text{Model 2}}) \times (\sigma_{\overline{\nu}_e/\overline{\nu}_\mu}^{\text{Model 1}} - \sigma_{\overline{\nu}_e/\overline{\nu}_\mu}^{\text{Model 2}}). \tag{4.4}$$

The covariance matrix then is used to determine the error $\delta_{x/y}$ on $\sigma_{x/y}$ and the correlation C between these values. The standard method of error propagation sets the uncertainty on $\sigma_{\nu_e/\overline{\nu}_e}$

$$\delta_{\overline{e}\to e} = \sqrt{\delta_{\mu\to e}^2 + \delta_{\overline{\mu}\to\overline{e}}^2 - 2 \times C \times \delta_{\mu\to e} \times \delta_{\overline{\mu}\to\overline{e}}}. \tag{4.5}$$

Another method, to determine the error on σ_{ν_e/ν_μ} and $\sigma_{\overline{\nu}_e/\overline{\nu}_\mu}$, is explained below, as it shows more intuitively the way how the different cross-section ratios are used. Both methods finally lead to the same results. As mentioned before, the ND280 detector mainly constraints the muon neutrino cross-section and is strongly limited by the available statistics for electron neutrinos. Therefore the electron neutrino cross-section σ_{ν_e} is inferred from the measured muon neutrino cross-section σ_{ν_μ} using the weight $\mathcal{W}_{\mu\to e} = \sigma_{\nu_e/\nu_\mu}$:

$$\sigma_{\nu_e} = \sigma_{\nu_\mu} \times \mathcal{W}_{\mu\to e}. \tag{4.6}$$

This weight is calculated as the ratio between the theoretical prediction of the electron and muon neutrino cross-section, which changes when changing the theoretical model. Therefore, to determine a systematic uncertainty, the change in this weight has to be evaluated. Since the systematic uncertainties are usually fractional, the prediction of the Spectral Function is used as the nominal prediction. Therefore the fractional systematic uncertainty $\delta_{\mu\to e}$ is defined as

$$\delta_{\mu\to e} = \frac{\mathcal{W}_{\mu\to e}^{SF} - \mathcal{W}_{\mu\to e}^{CRPA}}{\mathcal{W}_{\mu\to e}^{SF}}. \tag{4.7}$$

This is done similarly for anti-neutrinos, where the anti-neutrino cross-section is written as $\sigma_{\overline{\nu}_\mu} = \sigma_{\nu_\mu} \times \mathcal{W}_{\mu \to \overline{\mu}}$, meaning

$$\sigma_{\overline{\nu}_e} = \sigma_{\nu_\mu} \times \mathcal{W}_{\mu \to \overline{\mu}} \times \mathcal{W}_{\overline{\mu} \to \overline{e}}. \tag{4.8}$$

Since ND280 constrains the muon and anti-muon neutrino cross-sections, the weight $\mathcal{W}_{\mu \to \overline{\mu}} = \sigma_{\overline{\nu}_\mu/\nu_\mu}$ does not contribute to the systematic uncertainty. Therefore, also here, the fractional systematic uncertainty for the anti-neutrino case is given by

$$\delta_{\overline{\mu} \to \overline{e}} = \frac{\mathcal{W}_{\overline{\mu} \to \overline{e}}^{SF} - \mathcal{W}_{\overline{\mu} \to \overline{e}}^{CRPA}}{\mathcal{W}_{\overline{\mu} \to \overline{e}}^{SF}}. \tag{4.9}$$

4.4.1 Evaluation

The resulting uncertainty on $\sigma_{\nu_e/\overline{\nu}_e}$ as a function of the phase space is shown in fig. 4.11a with the usual isolines at 2, 3, 4, and 5%. In fig. 4.11b these isolines are overlaid onto the HK expected spectra. The overall correlation between these models is $C = 1$. Even
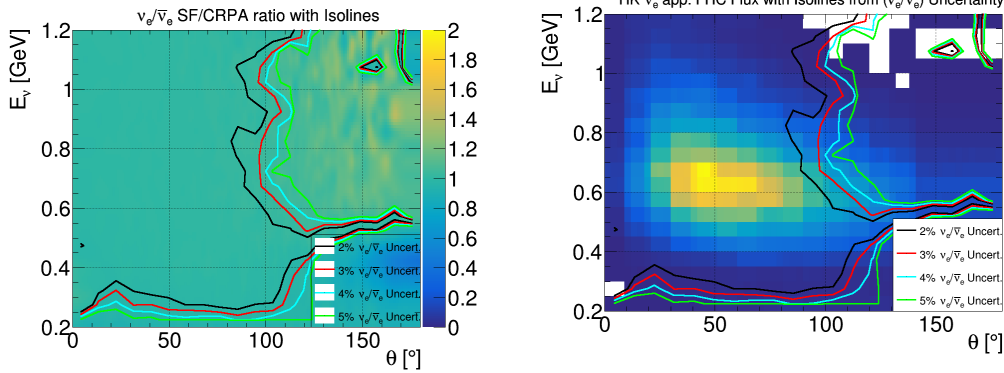
(a) Uncertainty on the $\nu_e/\overline{\nu}_e$ parameter.

(b) The isolines of the uncertainty overlaid on to the $\nu_\mu \to \nu_e$ HK recorded spectra.

Figure 4.11: The fractional difference between the cross-section ratio $\sigma_{\nu_e/\overline{\nu}_e}$, between CRPA and the SF model. The similar shape of σ_{ν_e/ν_μ} and $\sigma_{\overline{\nu}_e/\overline{\nu}_\mu}$ uncertainties results in a smaller uncertainty on $\sigma_{\nu_e/\overline{\nu}_e}$.

though the uncertainty on σ_{ν_e/ν_μ} and $\sigma_{\overline{\nu}_e/\overline{\nu}_\mu}$ were large in the region of the main flux peak, the correlation between them leads to a smaller discrepancy between both models when looking at the prediction of $\sigma_{\nu_e/\overline{\nu}_e}$. In the main flux-region, the deviations are below 2%. The region of the phase space related to a large uncertainty affecting the T2K experiment is again at angles above 100 degrees.

4.4.2 Flux Averaged Cross-Sections

In the HK experiment, the cross-section ratio between ν_e and $\overline{\nu}_e$ is used as a normalization parameter for the electron and anti-electron spectra at the SK/HK detector. Therefore the approach above, where the uncertainty was interpreted as a function of the phase space, is interesting for an illustrative understanding of the uncertainty, but to set an uncertainty used for HK in the current framework, one needs an overall uncertainty. For this, the weights are calculated using the flux-averaged cross-section. The neutrino cross-sections are averaged over the FHC flux, while the cross-section for the anti-neutrino is averaged over the RHC flux. Using the covariance matrix for the determination of the uncertainties results in the values shown in table 4.3. As expected by the study of the uncertainties on $\sigma^{SF/CRPA}_{\overset{(-)}{\nu}_e/\overset{(-)}{\nu}_\mu}$ in fig. 4.9, the uncertainty in the neutrino cross-section ratio is larger than the one for the anti-neutrinos. The uncertainty on $\sigma_{\nu_e/\overline{\nu}_e}$ due to nuclear effects is approximated to be 1.5%.

	$\delta_{\mu \to e}$	$\delta_{\overline{\mu} \to \overline{e}}$	$\delta_{\overline{e} \to e}$	Correlation
SF vs. CRPA	0.025	0.010	0.015	$+1$

Table 4.3: The uncertainties calculated for the flux-averaged differences between CRPA and the SF model.

HK uses water and not pure Oxygen as its target. Therefore around 20% of the target is Hydrogen, which does not undergo FSI. Hence it is expected that the uncertainty on $\sigma_{\nu_e/\overline{\nu}_e}$ is smaller if this is taken in to account. A more detailed evaluation of this will be necessary in the future.

4.5 Dependence of $\sigma_{\nu_e/\overline{\nu}_e}$ on Cross-Section Parameters

Both the SF and CRPA models are dependent on certain parameters like the M_A^{QE} value. In this section the effect of these parameters on $\sigma_{\nu_e/\overline{\nu}_e}$ is studied. A further comparison to other models is performed to get a better understanding of the uncertainty that should be used in the next section.

The baseline for this is the SF using an M_A^{QE} value of 1.21 GeV on Oxygen. The full set of models and parameters used are included in the appendix table C.1. A selection of these results are shown in table 4.4 and fig. 4.13.

Influence of M_A^{QE}

First, the influence of the M_A^{QE} value is investigated. While the T2K oscillation analysis includes an uncertainty to account for the variance in the M_A^{QE} value for the SF, the

impact of this variance on the CRPA model is not yet included. Nonetheless, both the impact of the M_A^{QE} value for the SF and CRPA are investigated here. For the CRPA model, the M_A^{QE} value in the previously evaluated set is 1.03 GeV.

For the Spectral Function, the nominal value of 1.21 GeV is compared to the value of 1.03 GeV. The resulting uncertainty of 0.05% is small compared to the uncertainty between the CRPA model and the SF.

The same holds when the M_A^{QE} value for the CRPA model is changed between 0.8, 1.03, and 1.21 GeV. With respect to the nominal SF, the uncertainty varies between 1.4 and 1.6 %. The impact of the M_A^{QE} value for the CRPA model on the uncertainty is therefore small compared to the uncertainty between the different models.

Pauli Blocking

To investigate the influence of Pauli Blocking on the σ_{ν_e/ν_μ} ratio, the SF is compared to a version in which the Pauli Blocking was disabled. The final uncertainty with respect to the SF including Pauli Blocking is small. This is due to the fact, that the region where the Pauli Blocking affects the cross-section ratio lies outside of the T2K/HK flux, which the cross-section was averaged over. A similar effect was seen in for the CRPA model in the previous sections. The resulting cross-section ratios σ_{ν_e/ν_μ} for the two cases can be seen in fig. 4.12. Here the change that Pauli-Blocking introduces can be seen clearly in the region of small angles and low energies.
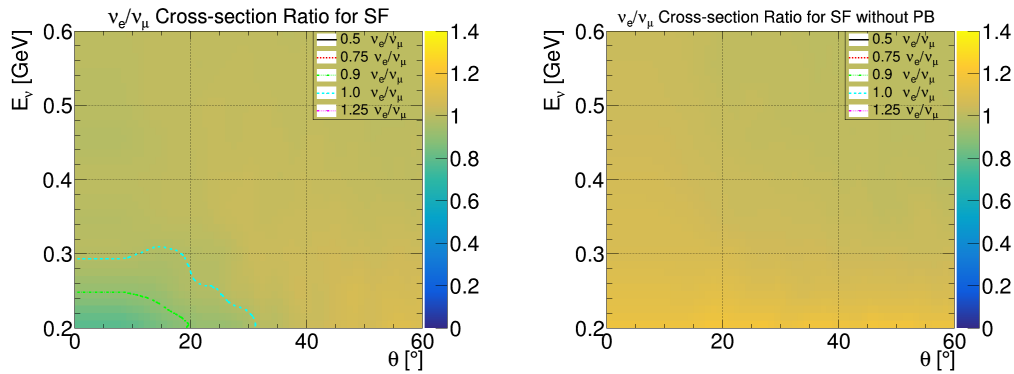
(a) The cross-section ratio σ_{ν_e/ν_μ} for the SF including PB.

(b) The cross-section ratio σ_{ν_e/ν_μ} for the SF without PB.

Figure 4.12: The cross-section ratios for the Spectral Function prediction including and excluding Pauli-Blocking. The effect that Pauli Blocking has on the low energy and forward-angled region of the phase-space can be clearly seen. As this region where these two predictions differ, lies outside of the T2K/HK flux, the final uncertainty between these is very small.

		$\delta_{\mu \to e}$	$\delta_{\overline{\mu} \to \overline{e}}$	$\delta_{\overline{e} \to e}$	Cor.
SF	CRPA	0.025	0.010	0.015	+1
CPRA	SuSAv2	0.001	0.002	0.004	-1
SF	SuSAv2	0.023	0.012	0.011	+1
CRPA	LFG	0.027	0.019	0.009	+1
LFG	SF	0.003	0.009	0.006	+1
SF	SF w/o PB	0.001	0.001	7e-5	+1
HF	CRPA	0.001	0.002	0.0006	+1
CRPA C	SF C	0.023	0.011	0.012	+1
CRPA C	SF	0.023	0.009	0.015	+1
SF 1.21	SF 1.03	0.0001	0.0006	0.0005	1
CRPA 0.8	CRPA 1.21	0.0007	0.001	0.002	-1

Table 4.4: The uncertainties calculated for the differences between the CRPA model and the Spectral Function. The full correlation comes from the comparison of only two models. If not mentioned otherwise, the assumed target is Oxygen.
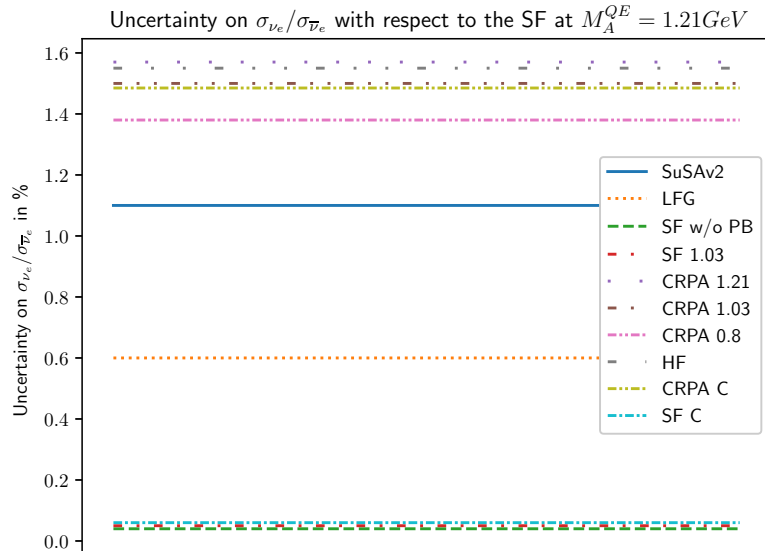
Figure 4.13: The uncertainties between different models. If not differently noted the cross-section is evaluated on oxygen.

RPA Inclusion

The CRPA model is based on the Hartree-Fock mean-field approach, but with the addition of the random phase space approximation (RPA). To evaluate the influence of the RPA correction on the $\nu_e/\overline{\nu}_e$ cross-section ratio, the CRPA model is compared to the pure HF predictions. Table 4.4 shows that the inclusion of the RPA correction leads to an uncertainty of 0.06%, which is small compared to the model differences between CRPA and SF. This can further be seen in fig. 4.13, where HF and CRPA with an M_A^{QE} value of 1.03 GeV lead to a similar uncertainty compared to the nominal SF.

Carbon and Oxygen

To evaluate the effect of the target differences between Carbon (ND280) and Oxygen (SK/HK), the analysis was done using the SF on Oxygen and then CRPA on Carbon and a comparison between the SF and CRPA predictions on Carbon. In both cases, the resulting uncertainty on $\sigma_{\nu_e/\overline{\nu}_e}$ is comparable to the one on Oxygen between both models. Therefore the target differences lead only to small discrepancies, which are dominated by the different modeling of FSI in the two models.

Local Fermi Gas & SuSAv2

The same study was done by comparing the predictions of the Local Fermi Gas (LFG) and the SuSAv2 model to the SF model. Results in fig. 4.13 show that the SuSAv2 model and the LFG models lie somewhere between the SF and HF predictions. The SuSAv2 model is closer to the HF predictions, which makes sense as it uses a relativistic HF Ansatz. Analogously the LFG is more similar to the SF. This clustering of models hints at the fact that the driving force between the discrepancies could be the different modeling of the FSI, even though the region where this difference is the largest does not directly impact HK.

4.6 Final Covariance Matrix

This work started to investigate the differences between model predictions of CRPA and SF in the forward scattered region. As these fall in a part of the T2K/HK phase-space which is only very sparsely populated, those differences are evaluated to not significantly impact the current and future experiments. During this research, larger discrepancies at angles above 50 degrees were found to impact the experiments more seriously. The sources of these differences are not clear yet but could be due to insufficient attention paid to these regions during the construction of the models.

It was shown that the largest variation between models comes from the comparison of the SF and CRPA predictions. Since comparing these two models implies the largest

uncertainty on the $\sigma_{\nu_e/\overline{\nu}_e}$ parameter, the corresponding covariance matrix (table 4.3)

$$V_{e,\overline{e}}^{\text{nuc. eff}} = \begin{pmatrix} 2.5\%^2 & 1 \times 1\% \times 2.5\% \\ 1 \times 1\% \times 2.5\% & 1\%^2 \end{pmatrix} \qquad (4.10)$$

is used for the further evaluation. This leads to uncertainty on $\nu_e/\overline{\nu}_e$ due to the model dependence of the nuclear effects of around 1.5%. As the nuclear effect uncertainties and the ones coming from radiative corrections are independent, this matrix has to be added to the already existing covariance matrix for radiative corrections. The total uncertainty then depends on the currently assumed values of the radiative corrections. For the main part of the next chapter, the current estimation for HK in eq. (3.7) is used. This would then result in an overall uncertainty of 3.1% on $\sigma_{\nu_e/\overline{\nu}_e}$.

Another covariance matrix used is the one from the 2018 T2K oscillation analysis. It already includes a way to account for the nuclear effects, even though in a more simple way. Nonetheless, the two covariance matrices are added. As will be shown in the next chapter, the inclusion of nuclear effects in to the T2K covariance matrix will not lead to a significant reduction of the sensitivity, even when HK statistics are assumed.

Impact of nuclear effects on the search for CP violation at Hyper-K via $\nu_\mu \rightarrow \nu_e$ oscillations

Having evaluated how the modeling of nuclear effects can lead to different cross-section predictions and having set a corresponding $\sigma_{\nu_e} - \sigma_{\overline{\nu}_e}$ covariance matrix, the next step is to assess how this affects the HK experiment. Therefore a study regarding the resolution and sensitivity of the HK experiment on δ_{CP} is performed. For this, the VALOR analysis software was used. VALOR is a neutrino oscillation software fitting package, originally designed for the T2K experiment, but now also used in other experiments like Hyper-Kamiokande, DUNE, and the short-baseline neutrino program at Fermilab.

5.1   Systematic Uncertainties on $\sigma_{\nu_e/\overline{\nu}_e}$

In the previous chapter a covariance matrix for the estimation of the $\sigma_{\nu_e/\overline{\nu}_e}$ systematic uncertainty due to nuclear effects (NE) was determined. Based on this covariance matrix, four sets of systematic uncertainties are defined for the studies in this chapter. They are summarized in table 5.1.

The systematic set of uncertainties from the 2018 T2K oscillation analysis is used without (T2K-like) and including (T2K-like+NE) the nuclear effects systematics found in the previous chapter's discussion. Further, the systematic uncertainty currently assumed for the HK experiment is also used. Without nuclear effects, this corresponds to an uncertainty on $\sigma_{\nu_e/\overline{\nu}_e}$ of 2.7%. Including nuclear effects the uncertainty increases to 3.1%.

- T2K-like: 2018 T2K systematic uncertainty, including an uncertainty on $\sigma_{\nu_e/\overline{\nu}_e}$ of 4.9%. This includes the radiative corrections uncertainty and an simple estimation of nuclear effect uncertainties.

	T2K	HK	T2K+NE	HK+NE
σ_{ν_e/ν_μ}	2.83%	1.7%	3.7%	3.0%
$\sigma_{\overline{\nu}_e/\overline{\nu}_\mu}$	2.83%	1.7%	3.0%	1.9%
C	-0.5	-0.33	-0.13	0.17
$\sigma_{\nu_e/\overline{\nu}_e}$	4.9%	2.7%	5.1%	3.1%

Table 5.1: The names given for the different sets of uncertainties used with the corresponding set of uncertainties in the cross-section ratios. Here C stands for the correlation between the two cross-section ratios σ_{ν_e/ν_μ} and $\sigma_{\overline{\nu}_e/\overline{\nu}_\mu}$.

- T2K-like+NE: 2018 T2K systematic uncertainty with the addition of the covariance matrix due to nuclear effects (NE) found in eq. (4.10). This results in a total systematic uncertainty on $\sigma_{\nu_e/\overline{\nu}_e}$ of 5.1%.

- HK: Expected Hyper-Kamiokande systematic uncertainty. This includes an uncertainty on $\sigma_{\nu_e/\overline{\nu}_e}$ of 2.7% due to radiative corrections and second class currents as discussed in section 3.5. The corresponding covariance matrix is found in eq. (3.7). Due to smaller theoretical uncertainties in the calculations for the radiative corrections, this uncertainty is smaller compared to the T2K-like. This is required for the HK experiment to not be prematurely systematically limited.

- HK+NE: Expected Hyper-Kamiokande systematic uncertainties, with the addition of the covariance matrix due to nuclear effects found in eq. (4.10), resulting in a total systematic uncertainty on $\sigma_{\nu_e/\overline{\nu}_e}$ of 3.1%.

5.1.1   Uncertainty on the number of events

In order to evaluate how the different sets of systematic uncertainties affect the number of selected neutrino events at HK, 10 000 Monte Carlo (MC) toys were computed, assuming 2.7×10^{22} PoT (10 years of HK runtime). This leads to a distribution of the number of events, from which the mean and the root mean square (RMS) are extracted. In these Toy MC the only variable that was varied was the cross-section ratio σ_{ν_e/ν_μ} and its corresponding anti-neutrino counterpart $\sigma_{\overline{\nu}_e/\overline{\nu}_\mu}$. For them a Gaussian distribution following the systematic uncertainties in table 5.1 was assumed. This was done to evaluate how much the specific systematic uncertainty affects the overall event rate. The results can be found in table 5.2.

As expected the total number of events in all four tables is very similar. Small differences in the mean number of events are seen for the multi-ring electron sample (FHC multire). But even in this case, the deviations are negligible.

The muon neutrino samples are not affected by the variation of the σ_{ν_e/ν_μ} ratio and

Sample HK	Mean	RMS	100× RMS/mean
FHC 1rmu	9577.74	0.02	0.00
RHC 1rmu	12654.40	0.01	0.00
FHC 1re	1926.86	26.76	1.39
RHC 1re	2172.95	4.86	0.22
FHC multire	187.44	2.61	1.39
1Re FHC / RHC	0.89	0.01	1.17

HK Systematics.

Sample HK+NE	Mean	RMS	100× RMS/mean
FHC 1rmu	9577.74	0.05	0.00
RHC 1rmu	12654.39	0.01	0.00
FHC 1re	1926.57	51.45	2.67
RHC 1re	2172.90	9.34	0.43
FHC multire	187.41	5.01	2.67
1Re FHC / RHC	0.89	0.02	2.24

HK Systematics including Nuclear Effects.

Sample T2K	Mean	RMS	100× RMS/mean
FHC 1rmu	9577.74	0.05	0.00
RHC 1rmu	12654.40	0.01	0.00
FHC 1re	1927.11	49.86	2.59
RHC 1re	2173.00	9.05	0.42
FHC multire	187.47	4.86	2.59
1Re FHC / RHC	0.89	0.02	2.17

T2K Systematics.

Sample T2K+NE	Mean	RMS	100× RMS/mean
FHC 1rmu	9577.74	0.06	0.00
RHC 1rmu	12654.40	0.02	0.00
FHC 1re	1927.78	66.25	3.44
RHC 1re	2173.12	12.02	0.55
FHC multire	187.53	6.45	3.44
1Re FHC / RHC	0.89	0.03	2.88

T2K Systematics including Nuclear Effects.

Table 5.2: The change of the overall recorded number of events for the SK and HK far detector set of uncertainties. Randomisation statistics from 10000 pseudo-data sets, with the σ_{ν_e/ν_μ} parameters varied.

the effect on the electron neutrinos is, as expected, larger for the T2K-like systematic uncertainties compared to the Hyper-Kamiokande ones.

5.1.2 Systematic Categories

The same kind of analysis as done in the previous section was repeated, this time with larger groups of systematic parameters varied, i.e. flux, detector, and cross-section systematic uncertainties. In the flux group, several parameters of the initial flux reconstruction are varied. Similarly, the detector category includes detector effects and the wrong classification of event modes due to FSI. The third category includes systematics on the cross-section determination, like the uncertainty on the $\sigma_{\nu_e/\overline{\nu}_e}$ ratio. The resulting distribution of the number of events is translated into an uncertainty in each sample.

For each of the four categories defined above, this analysis was done separately. The results for the HK set of systematics are found in table 5.3. This table also includes the corresponding results for the full varied set of systematics (*All syst*) and the different σ_{ν_e/ν_μ} uncertainties of the other three sets of systematics.

Including the nuclear effect uncertainties in to the T2K-like set has a less pronounced effect compared to the HK-like set. As the uncertainties are effectively summed in quadrature, this is expected. But even for the HK-like systematics, the overall change is small.

Error source	1-ring μ-like		1-ring e-like			
	ν-mode	$\bar{\nu}$-mode	ν-mode 0 d.e.	$\bar{\nu}$-mode 0 d.e.	ν-mode 1 d.e.	ν-mode/$\bar{\nu}$-mode 0 d.e.
Flux	0.84%	0.83%	0.78%	0.75%	0.78%	0.30%
Detector+FSI	1.03%	0.96%	1.98%	2.29%	7.31%	0.49%
Cross section	0.73%	0.66%	2.93%	3.02%	1.57%	1.37%
ν_e/ν_μ (2.7%)	0.00%	0.00%	0.99%	0.38%	0.66%	0.61%
ν_e/ν_μ (3.1%)	0.00%	0.00%	1.85%	0.71%	1.23%	1.13%
ν_e/ν_μ (4.9%)	0.00%	0.00%	1.91%	0.74%	1.27%	1.17%
ν_e/ν_μ (5.1%)	0.00%	0.00%	2.50%	0.96%	1.67%	1.53%
All syst (ν_e/ν_μ 2.7%).	1.16%	1.11%	3.16%	3.68%	7.45%	1.37%
All syst (ν_e/ν_μ 3.1%).	1.15%	1.11%	3.54%	3.80%	7.51%	1.49%
All syst (ν_e/ν_μ 4.9%)	1.17%	1.12%	3.52%	3.81%	7.44%	2.14%
All syst (ν_e/ν_μ 5.1%)	1.14%	1.12%	3.86%	3.89%	7.59%	2.21%

Table 5.3: Percentage error on event rate by error source and sample, for four different ν_e/ν_μ uncertainties as described earlier in the text as HK (2.7%), HK+N.E. (3.1%), T2K (4.9%) and T2K+NE (5.1%).

5.2 Asimov-Fits in VALOR

Using the VALOR oscillation analysis software, it is possible to generate Asimov data sets for a given set of oscillation parameters. An Asimov data set is the nominal predicted Monte Carlo spectrum, i.e. a data set where all observed quantities are set to their expected value. In this chapter several fits to such Asimov data sets are performed to extract the oscillation parameters.

The fits in VALOR are using the binned likelihood ratio method [29, 30, 31]. For this the recorded spectra at HK is split in to N bins, where bin i includes n_i^{obs} events. The total observed event rate $n_{\text{tot}}^{\text{obs}} = \sum_{i=0}^{N-1} n_i^{\text{obs}}$ is Poisson distributed. Its mean is the total expected eventrate $n_{\text{tot}}^{\text{exp}} = \sum_{i=0}^{N-1} n_i^{\text{exp}}$. Here $n_i^{\text{exp}}(\vec{o}, \vec{a})$ is the expected number of events in bin i, where $\vec{o}$ are the oscillation parameters to be fit and $\vec{a}$ are nuisance parameters, like uncertainties. The probability density function (p.d.f.) is therefore given by

$$f_{\text{Poisson}} = \frac{[n_{\text{tot}}^{\text{exp}}]^{n_{\text{tot}}^{\text{obs}}} e^{-n_{\text{tot}}^{\text{exp}}}}{n_{\text{tot}}^{\text{obs}}!}. \tag{5.1}$$

As there are N bins, there are N possible outcomes when placing a single event in to the histogram. The p.d.f. for this is the standard multinomial

$$f_{\text{multinomial}} = n_{\text{tot}}^{\text{obs}}! \prod_{i=0}^{N-1} \frac{1}{n_i^{\text{obs}}!} \left[\frac{n_i^{\text{exp}}}{n_{\text{tot}}^{\text{exp}}} \right]^{n_i^{\text{obs}}}. \tag{5.2}$$

The outcome of the reconstruction therefore follows the joint p.d.f.

$$f_{\text{joint}} = e^{-n_{\text{tot}}^{\text{exp}}} \prod_{i=0}^{N-1} \frac{1}{n_i^{\text{obs}}!} \, [n_i^{\text{exp}}]^{n_i^{\text{obs}}} \tag{5.3}$$

Dividing this by the oscillation parameter independent p.d.f.

$$f_0 = e^{-n_{\text{tot}}^{\text{obs}}} \prod_{i=0}^{N-1} \frac{1}{n_i^{\text{obs}}!} \, [n_i^{\text{obs}}]^{n_i^{\text{obs}}} \tag{5.4}$$

finally yields the likelihood ratio

$$\lambda = e^{n_{\text{tot}}^{\text{obs}} - n_{\text{tot}}^{\text{exp}}} \prod_{i=0}^{N-1} \left[\frac{n_i^{\text{exp}}}{n_i^{\text{obs}}} \right]^{n_i^{\text{obs}}}. \tag{5.5}$$

The fit then minimizes the log-likelihood ratio

$$-2\ln(\lambda(\vec{o}, \vec{a})) = 2 \sum_{i=0}^{N-1} \left(n_i^{\text{obs}} \ln \left(n_i^{\text{obs}}/n_i^{\text{exp}} \right) + n_i^{\text{exp}} - n_i^{\text{obs}} \right) + (\vec{a} - \vec{a}_0)\mathbf{C}^{-1}(\vec{a} - \vec{a}_0). \tag{5.6}$$

Here the last term is an added penalty term to constraint the nuisance parameters $\vec{a}$ around their nominal value $\vec{a}_0$. $\mathbf{C}$ is the covariance matrix between the nuisance parameters. This leads to a larger penalty the more the nuisance parameters deviate from the nominal value, depending on the uncertainty connected to the parameter. For minimisation of $-2\ln(\lambda)$ the MIGRAD algorithm is used, which calculates the first derivative and the covariance matrix of all the parameters. With this a step direction is determined, similar to the gradient descent method. For a more technical summary of this topic see [30]. The log-likelihood ratio is used as the large sample limit of it approaches a χ^2 distribution.

In this study, the parameter of interest is δ_{CP}. Several values of δ_{CP}^{fix} are scanned and the corresponding $\Delta\chi^2(\delta_{CP}^{fix})$ is calculated as the negative log-likelihood ratio $-2\ln\left(\lambda^{\text{fix}}/\lambda^{\text{BF}}\right)$ between the best fit (BF) and the currently scanned value. If the tested fixed value equals the best fit value $\Delta\chi^2$, therefore, equals 0.

For all of the following chapters, the mass hierarchy is assumed to be normal. An example of such a $\Delta\chi^2$ distribution for the HK systematic set of uncertainties, assuming a true $\delta_{CP} = 0$, is shown in fig. 5.1. The $\Delta\chi^2$ distribution takes its minimum at the assumed true value of $\delta_{CP} = 0$. The two maxima are at approximately $\pm\pi/2$, as here the predicted spectra differ the most between the trivial phase $\delta_{CP} = 0, \pm\pi$ and the tested value of $\delta_{CP} = \pm\pi/2$. At the boundaries ($\delta_{CP} = \pm\pi$), the χ^2 value again drops, as the predicted oscillated spectra for the three trivial phases are similar. The distribution in χ^2 is not symmetric around $\delta_{CP} = 0$. Differences between the positive and negative values of δ_{CP} are due to the fact that the value of $\sigma_{\nu_e/\bar{\nu}_e}$ has an opposite effect on the FHC and RHC sample. Since the statistical fluctuation in the RHC fluctuation is roughly 2-3

times higher compared to the FHC sample, the positive values of δ_{CP} can be excluded with a higher significance. Even taking three times more data in the RHC mode does not fully compensate for this difference due to the square-root scaling of the statistical uncertainty.
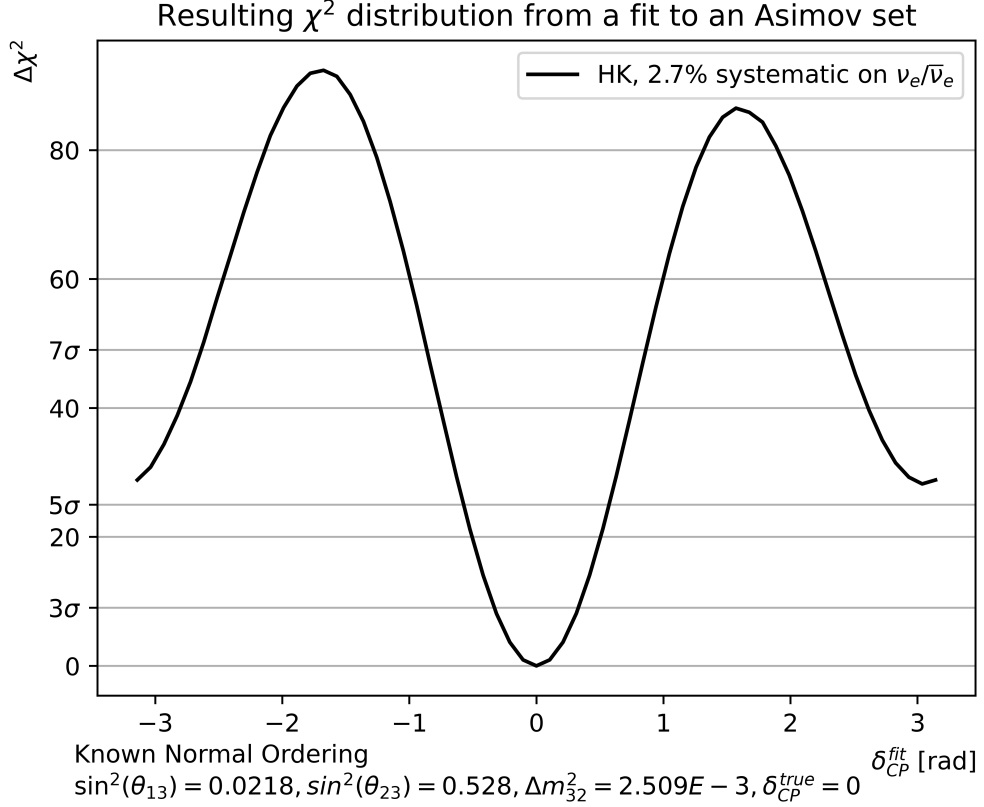
Figure 5.1: Result of a fit from an Asimov data set using $\delta_{CP} = 0$ and assuming HK (2.7%) systematic uncertainties. The mass-hierarchy is fixed to be normal and know. Significance lines assume 1 degree of freedom in the χ^2 distribution of $\Delta\chi^2$.

5.3 Resolution Study

The resulting $\Delta\chi^2$ distributions from the corresponding fits can be used to determine the resolution of the HK experiment to δ_{CP}. For this the half width of the 68% confidence intervals ($\pm 1\sigma$) for δ_{CP} is determined. Four different values of δ_{CP} where evaluated and are shown in table 5.4.

Instead of the usually used 361 point grid for δ_{CP}, a 61 point grid was used to reduce CPU time. To improve the final results, the corresponding $\Delta\chi^2$ distributions were fitted with a fourth-order polynomial. This owes results close to the standard method.

(a) $\delta_{CP}^{true} = 0$

(b) $\delta_{CP}^{true} = \pi$

(c) $\delta_{CP}^{true} = \pi/2$

(d) $\delta_{CP}^{true} = -\pi/2$
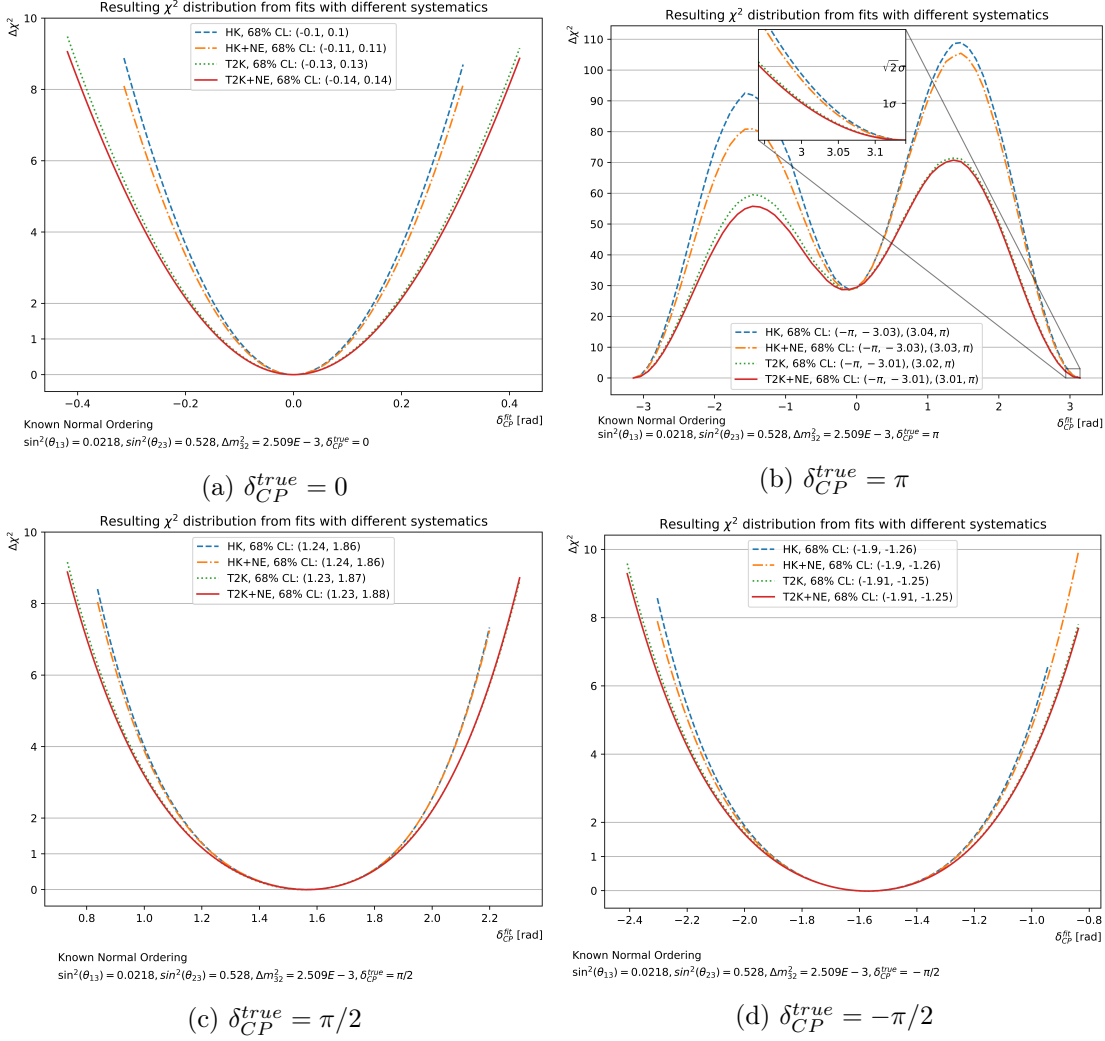
Figure 5.2: The resulting χ^2 distribution of the fits assuming different values of δ_{CP}, as labeled in the captions. This allows for the determination of the resolution to δ_{CP} that the T2K/HK experiments are able to achieve assuming the given sets of systematics. The corresponding confidence intervals are noted in the legend of the corresponding plots.

The result for the phase $\delta_{CP} = 0$ is shown in fig. 5.2a. Here the decrease in the width of the χ^2 distribution between the different sets of uncertainty can be seen. Going from the T2K-like to HK-like systematics, an improvement of the resolution of 22% is seen. Adding the nuclear effect uncertainty, the HK-like and T2K-like resolutions change by 5% and 2% respectively.

In fig. 5.2c and fig. 5.2d the results for $\delta_{CP} = \pm\pi/2$ are shown. Both $\Delta\chi^2$ distributions are wider compared to the one at $\delta_{CP} = 0$. The reason for this is the large asymmetry in the oscillation probability at $\sin^2(\delta_{CP}) = 1$, leading to a larger (smaller) sample size

δ_{CP} resolution for different $\sigma_{\nu_e/\overline{\nu}_e}$ systematic uncertainties				
	T2K	HK	T2K+NE	HK+NE
$\delta_{CP} = 0$	7.649°	5.987°	7.821°	6.245°
$\delta_{CP} = \pi/2$	18.535°	17.934°	18.592°	18.191°
$\delta_{CP} = -\pi/2$	19.022°	18.277°	19.137°	18.449°
$\delta_{CP} = \pi$	7.277°	6.073°	7.649°	6.159°

Table 5.4: The resolution to δ_{CP} for different assumed true δ_{CP} values evaluated using different sets of uncertainties. The exclusion at $\delta_{CP} = \pm\pi/2$ is worse than the at $\pi, 0$.
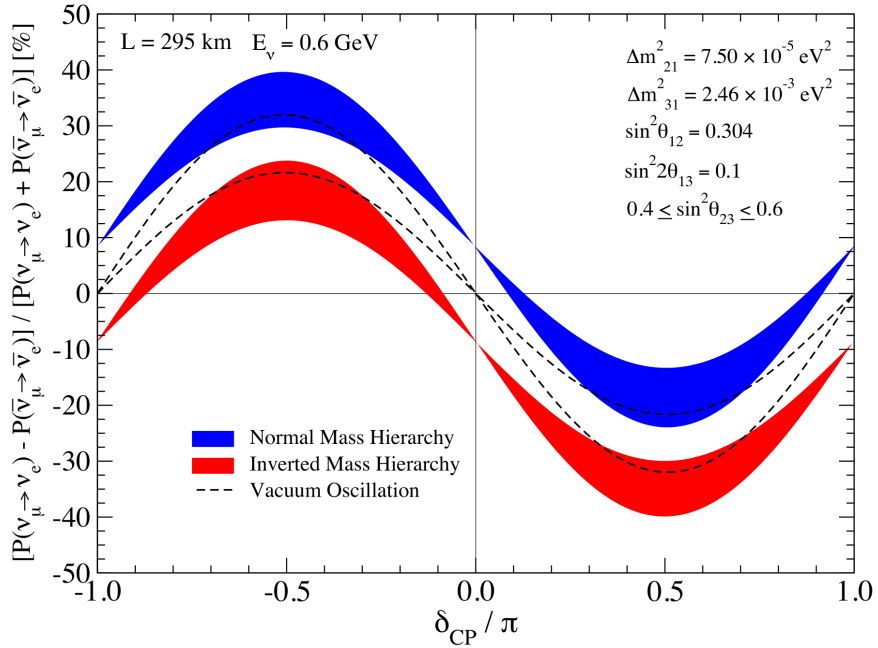
Figure 5.3: The fractional difference in oscillation probability between neutrinos and anti-neutrinos for different values of δ_{CP}. Taken from [23].

for the corresponding (anti-)neutrino sample. The asymmetry can be seen in fig. 5.3 as a function of δ_{CP}/π. This then leads to an increased statistical error on the ν_e or $\overline{\nu}_e$ samples. Due to this, the systematical error becomes less relevant compared to the statistical one. Further, the flatness of the asymmetry at $\pm\pi/2$ leads to a degeneracy of δ_{CP} values in this region. Therefore the fit can not precisely distinguish between these values, which leads to a widened resolution.

When looking at fig. 5.2b, the distribution looks different. This is due to the fact that the spectrum is partially degenerated between $\pm\pi$ and 0. Therefore the $\Delta\chi^2$ plot has local minima at $-\pi, 0$ and π. To show all three minima, the full range of δ_{CP} is shown, while this was not the case for the rest of the plots.

5.4 Exclusion Study

In this section, the power of the HK experiment to reject a trivial phase, i.e. $\sin \delta_{CP} = 0$, is analyzed. For this, a certain value of the parameter of interest, in case δ_{CP}, is chosen and several MC toys are thrown. Then a fit is performed for several values of δ_{CP} and the corresponding $\Delta\chi^2$ distribution is analyzed. The resulting $\Delta\chi^2 = \chi^2(\delta_{CP}^{\text{true}}) - \chi^2(\delta_{CP} = 0)$ values are then plotted as a function of the assumed true $\delta_{CP}^{\text{true}}$. Usually $\sqrt{\Delta\chi^2}$ is considered, since this corresponds to the significance, meaning a $\sqrt{\Delta\chi^2} = 3$ equals a 3σ exclusion.

Assuming 10 years of data taking, the sensitivity for the four sets of systematic uncertainties are plotted in fig. 5.4. The mass ordering is assumed to be normal and for the oscillation parameters the current values from [32] are used, as indicated on the plot.
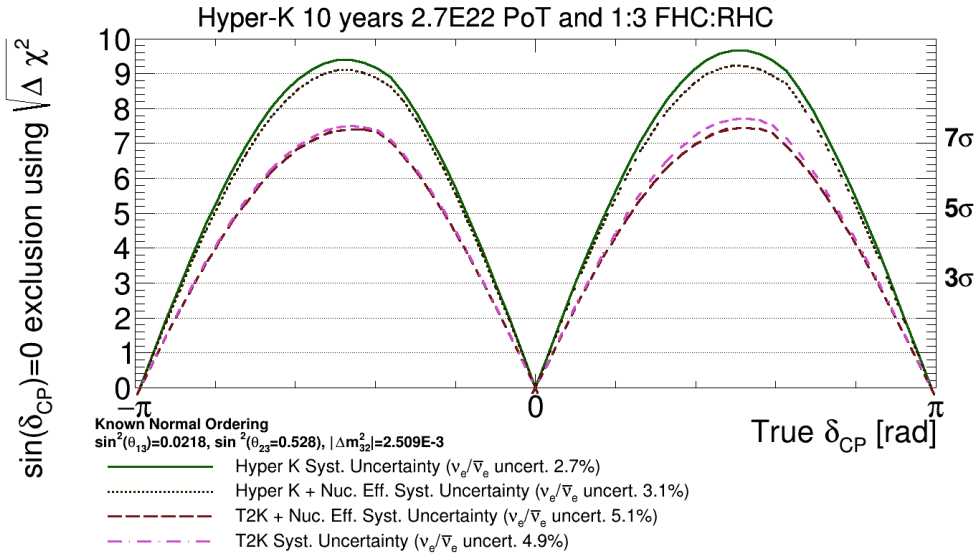
Figure 5.4: Exclusion power for $\sin \delta_{CP} =$ for different sets of systematic uncertainties.

5.4.1 Effect on T2K

The results for the assumed T2K-like systematics are shown in fig. 5.4 as the dashed brown and dash-dotted magenta lines. In the region of negative δ_{CP} values, the difference between the pure T2K-like systematics and the addition of the uncertainties of the nuclear effects is barely visible. For positive δ_{CP} values there is a small difference visible of roughly a quarter standard deviation in the peak position. Further, the width of the distribution is reduced. As discussed earlier, the differences between the RHC and FHC samples lead to an asymmetry in the exclusion power between positive and negative values of δ_{CP}.

For the T2K experiment, the data samples are smaller and therefore the statistical uncertainties are significantly larger compared to HK. As the inclusion of nuclear effects in to the overall uncertainty did not lead to a major change for HK statistics, it is assumed that the effect on sample sizes as currently available to T2K is even less pronounced. This was however not studied in detail.

5.4.2 Effect on Hyper Kamiokande

Comparing the green solid and black dotted lines in fig. 5.4, resembling the HK-like systematics, the effect that the addition of the nuclear effect uncertainty has is more pronounced as in the case for the T2K-like systematics. In the peaks at $\pm\pi/2$, a reduction of the sensitivity of half a standard deviation is seen. Moreover, the overall peak is narrower. Looking at values below the 3σ level, the shape differences become negligible. In total, also for the HK-like systematics, the effect is considered to be small.

5.5 Discussion

In this chapter, the overall effect of the inclusion of the systematic uncertainty due to nuclear effects was investigated. This was done by first looking at the resolution, where a change of several percent was seen for both the T2K-like and HK-like systematics. Even though the overall resolution at $\delta_{CP} = 0$ is better, adding the systematic uncertainty to it has a more pronounced effect compared to $\delta_{CP} = \pm\pi$. On the one side, this means that the measurements, when assuming maximally broken CP asymmetry are less precise but on the other, they are less affected by the added uncertainty. Overall, in the framework of the models studied for this thesis, the nuclear effects do not change the HK sensitivity to the CP violating phase $\delta_{CP} = 0$ in a significant manner. The main difference comes from changing between the T2K-like and HK-like systematic uncertainties for $\sigma_{\nu_e/\overline{\nu}_e}$. Since this whole evaluation is done using models and predictions instead of data, the small impact would have to be confirmed by neutrino data.

Conclusion and Outlook

In this work, we focused on the influence of nuclear effects on the electron-neutrino cross-section prediction and its impact on the HK experiment. For this the forward scattering region was investigated in detail, motivated by the findings in [1]. The authors showed that the cross-section ratio σ_{ν_e/ν_μ} between electron and muon neutrinos in the forward scattering region deviates between the Spectral Function and CRPA model. Due to the low flux in the affected region, the impact on the HK experiment was evaluated to be small.

Then the model dependence of the cross-section ratio $\sigma_{\nu_e/\overline{\nu}_e}$ was studied for the whole phase-space. Contrary to the initial expectation, the deviations between both models in the backward scattered region are more relevant for the HK experiment compared to the ones at low angles. The region with angles above 100 degrees was found to have an uncertainty larger than 5% for neutrinos and anti-neutrinos. This could be due to insufficiently precise modeling in the backward scattering area. More data needs to be evaluated for this.

An overall uncertainty for the cross-section dependence of nuclear effect modeling was set for the HK experiment. For this, the cross-sections were averaged over the corresponding expected oscillated spectrum at HK. The largest discrepancy amid the studied models was between SF and CRPA. The impact of the M_A^{QE} value of both the Spectral Function as well as the one of CRPA was found to only have a small impact compared to the overall change between models. The same holds for the inclusion of Pauli Blocking into the SF. Using the difference between CRPA and the SF as an estimator for the nuclear effect modeling uncertainty, a covariance matrix was constructed. From this, the systematic uncertainty on $\sigma_{\nu_e/\overline{\nu}_e}$ was evaluated to be 1.5%.

This uncertainty was then used in CP violation studies using the VALOR analysis software. Here the impact on the sensitivity and resolution of the HK experiment was evaluated. Including this extra uncertainty has a small effect, both in the case of the assumed T2K-like and HK-like systematic uncertainties. Similar findings hold for the resolution, where assuming T2K-like systematics, a reduction in resolution of below 2% and for HK-like of 5% was found when the nuclear effects were included. Both of these are small compared to the overall change between the T2K-like and HK-like systematic

uncertainties.

In the future a shape analysis of the $\sigma_{\nu_e/\bar{\nu}_e}$ uncertainty should be done, to get a better understanding of the phase-space depending effects on the HK experiment. This means that the uncertainty is included in the CP violation studies not as a single value, but as a function of the energy or lepton angle. This was not done in this thesis, as this would have required a significant extension of VALOR.

During this thesis a counter-intuitive phenomenon was found, when the Argon and Carbon predictions on σ_{ν_e/ν_μ} were regarded. The larger nucleus was less affected by FSI. To gain a sufficient understanding of this effect, more work has to be done on this topic.

This evaluation of the uncertainty is fully based on the prediction of different models and cannot be

As the nuclear effects, unlike the QED radiative corrections, can not be calculated, the only way to constrain the uncertainty is by using new electron neutrino data. This is especially necessary as the whole evaluation of the uncertainty is based on models, that are mainly constructed with insufficient data in the backward scattering region, which is where the major differences among the studied models lie.

Bibliography

[1] A. Nikolakopoulos, N. Jachowicz, N. Van Dessel, K. Niewczas, R. González-Jiménez, J. M. Udías, and V. Pandey, "Electron versus muon neutrino induced cross sections in charged current quasielastic processes," *Phys. Rev. Lett.*, vol. 123, p. 052501, Jul 2019. [Online]. Available: https://link.aps.org/doi/10.1103/PhysRevLett.123.052501

[2] E. Fermi, "Versuch einer theorie der β-strahlen. i," *Zeitschrift für Physik*, vol. 88, no. 3, pp. 161–177, Mar 1934. [Online]. Available: https://doi.org/10.1007/BF01351864

[3] F. Reines and C. L. Cowan, "Detection of the free neutrino," *Phys. Rev.*, vol. 92, pp. 830–831, Nov 1953. [Online]. Available: https://link.aps.org/doi/10.1103/PhysRev.92.830

[4] B. Pontecorvo, "Inverse beta processes and nonconservation of lepton charge," *Zh. Eksp. Teor. Fiz.*, vol. 34, p. 247, 1957.

[5] K. Abe *et al.*, "Evidence of Electron Neutrino Appearance in a Muon Neutrino Beam," *Phys. Rev. D*, vol. 88, no. 3, p. 032002, 2013.

[6] V. Kuzmin, V. Rubakov, and M. Shaposhnikov, "On anomalous electroweak baryon-number non-conservation in the early universe," *Physics Letters B*, vol. 155, no. 1, pp. 36–42, 1985. [Online]. Available: https://www.sciencedirect.com/science/article/pii/0370269385910287

[7] E. K. Akhmedov, "Do charged leptons oscillate?" *Journal of High Energy Physics*, vol. 2007, no. 09, p. 116, 2007.

[8] P. Zyla *et al.*, "Review of Particle Physics," *PTEP*, vol. 2020, no. 8, p. 083C01, 2020.

[9] B. Richter, "Conventional beams or neutrino factories: The Next generation of accelerator based neutrino experiments," 8 2000.

[10] V. Barger, K. Whisnant, S. Pakvasa, and R. J. N. Phillips, "Matter effects on three-neutrino oscillations," *Phys. Rev. D*, vol. 22, pp. 2718–2726, Dec 1980. [Online]. Available: https://link.aps.org/doi/10.1103/PhysRevD.22.2718

[11] J. A. Formaggio and G. P. Zeller, "From ev to eev: Neutrino cross sections across energy scales," *Rev. Mod. Phys.*, vol. 84, pp. 1307–1341, Sep 2012. [Online]. Available: https://link.aps.org/doi/10.1103/RevModPhys.84.1307

[12] O. Benhar, A. Fabrocini, and S. Fantoni, "The nucleon spectral function in nuclear matter," *Nuclear Physics*, vol. 505, pp. 267–299, 1989.

[13] A. M. Ankowski, O. Benhar, and M. Sakuda, "Improving the accuracy of neutrino energy reconstruction in charged-current quasielastic scattering off nuclear targets," *Phys. Rev. D*, vol. 91, p. 033005, Feb 2015. [Online]. Available: https://link.aps.org/doi/10.1103/PhysRevD.91.033005

[14] S. Gollapinni, "Neutrino Cross section Future," in *Prospects in Neutrino Physics*, 2 2016.

[15] R. González-Jiménez, G. D. Megias, M. B. Barbaro, J. A. Caballero, and T. W. Donnelly, "Extensions of superscaling from relativistic mean field theory: The susav2 model," *Phys. Rev. C*, vol. 90, p. 035501, Sep 2014. [Online]. Available: https://link.aps.org/doi/10.1103/PhysRevC.90.035501

[16] S. Dolan, A. Nikolakopoulos, O. Page, S. Gardiner, N. Jachowicz, and V. Pandey, "Implementation of the CRPA model in the GENIE event generator and analysis of nuclear effects in low-energy transfer neutrino-nucleus interactions," 10 2021.

[17] A. M. Ankowski, "Effect of the charged-lepton's mass on the quasielastic neutrino cross sections," *Phys. Rev. C*, vol. 96, p. 035501, Sep 2017. [Online]. Available: https://link.aps.org/doi/10.1103/PhysRevC.96.035501

[18] K. Abe *et al.*, "Indication of Electron Neutrino Appearance from an Accelerator-produced Off-axis Muon Neutrino Beam," *Phys. Rev. Lett.*, vol. 107, p. 041801, 2011.

[19] K. Abe *et al.*, "Precise Measurement of the Neutrino Mixing Parameter θ_{23} from Muon Neutrino Disappearance in an Off-Axis Beam," *Phys. Rev. Lett.*, vol. 112, no. 18, p. 181801, 2014.

[20] K. Abe *et al.*, "Measurements of neutrino oscillation in appearance and disappearance channels by the T2K experiment with 6.6×10^{20} protons on target," *Phys. Rev. D*, vol. 91, no. 7, p. 072010, 2015.

[21] D. Sgalaberna, "The T2K ND280 Upgrade," *PoS*, vol. ICHEP2020, p. 175, 2021.

[22] K. Abe *et al.*, "T2K ND280 Upgrade - Technical Design Report," 1 2019.

[23] K. Abe *et al.*, "Hyper-Kamiokande Design Report," 5 2018.

[24] J. Bian *et al.*, "Hyper-Kamiokande Experiment: A Snowmass White Paper, v1," in *2022 Snowmass Summer Study*, 3 2022.

[25] M. Day and K. S. McFarland, "Differences in quasielastic cross sections of muon and electron neutrinos," *Phys. Rev. D*, vol. 86, p. 053003, Sep 2012. [Online]. Available: https://link.aps.org/doi/10.1103/PhysRevD.86.053003

[26] O. Tomalak, Q. Chen, R. J. Hill, and K. S. McFarland, "QED radiative corrections to neutrino-nucleon elastic scattering," 5 2021.

[27] O. Benhar, A. Fabrocini, S. Fantoni, and I. Sick, "Spectral function of finite nuclei and scattering of gev electrons," *Nuclear Physics A*, vol. 579, no. 3, pp. 493–517, 1994. [Online]. Available: https://www.sciencedirect.com/science/article/pii/0375947494909202

[28] O. Benhar, N. Farina, H. Nakamura, M. Sakuda, and R. Seki, "Electron- and neutrino-nucleus scattering in the impulse approximation regime," *Phys. Rev. D*, vol. 72, p. 053005, Sep 2005. [Online]. Available: https://link.aps.org/doi/10.1103/PhysRevD.72.053005

[29] A. K. et. al., "Improved constraints on neutrino mixing from the t2k experiment with 3.13×10^{21} protons on target," *Phys. Rev. D*, vol. 103, p. 112008, Jun 2021. [Online]. Available: https://link.aps.org/doi/10.1103/PhysRevD.103.112008

[30] T. J. Dealtry, "A precision measurement of ν_μ disappearance in the t2k experiment," Ph.D. dissertation, University of Oxford, UK, 2014.

[31] K. A. et al, "Measurements of neutrino oscillation in appearance and disappearance channels by the t2k experiment with 6.6×10^{20} protons on target," *Phys. Rev. D*, vol. 91, p. 072010, Apr 2015. [Online]. Available: https://link.aps.org/doi/10.1103/PhysRevD.91.072010

[32] P. D. G. et al., "Review of Particle Physics," *Progress of Theoretical and Experimental Physics*, vol. 2020, no. 8, 08 2020, 083C01. [Online]. Available: https://doi.org/10.1093/ptep/ptaa104

[33] G. D. Megias, "Charged-current neutrino interactions with nucleons and nuclei at intermediate energies," Ph.D. dissertation, University of Seville, Spain, 2017, https://idus.us.es/xmlui/handle/11441/74826.

[34] C. K. C. Giunti, *Fundamentals of Neutrino Physics and Astrophysics*. Oxford University Press, 2019.

[35] E. K. Akhmedov, "Do charged leptons oscillate?" *Journal of High Energy Physics*, vol. 2007, no. 09, pp. 116–116, sep 2007. [Online]. Available: https://doi.org/10.1088/1126-6708/2007/09/116

Bibliography

Implementation of Hartree Fock Based Models in the T2K Neutrino Interaction Modeling Software

A.1 Reweighting

As explained above the CRPA model predicts substantial differences compared to the Spectral Function in the physics most important for extrapolating the near detector constraint to the far detector in the neutrino oscillation analysis. Assuming that CRPA describes nature, using the T2K nominal SF model, therefore, leads to incorrect constraints. To quantify this bias, we want to be able to evaluate the differences between these two models.

For an oscillation analysis, this would mean throwing toys for each model several times, which is time-consuming. Instead, the Spectral Function can be reweighted to match the predictions of the CRPA model. This is done by dynamically calculating the cross-section ratios of the two models in the relevant kinematic phase space and applying these as event weights. For the calculation of these weights, we can use theory predictions or high statistics Monte Carlo samples.

This way we can use solely the Spectral Function Monte Carlo sample for the evaluation of the bias, which saves computation time, as not every model has to be generated but inferred from the reweighting. The SF sample is reweighted to match the CRPA model predictions and then compared to this reweighted result.

The implementation is part of NIWGReWeight and also includes a reweighting to the SuSAv2, Hartree Fock, and SuSAv2-CRPA-Hybrid models. The resulting code can be seen on github [1] and in the T2K Technical Note 434 [2].

---

[1] https://github.com/t2k-software/NIWGReWeight/commit/6fb7d78329dfe6e81847dbb8ba4b6a25e8b53a58
[2] https://t2k.org/docs/technotes/434

A.2   Implementation

The implementation uses Hadron Tensors and NEUT Monte Carlo generated templates for the cross-sections and the weight calculation.

The Hadron Tensors return the double differential cross-section

$$\sigma_{HT}^{preJac} = \frac{d^2\sigma}{d\cos\theta dT}(E_\nu, \cos\theta, T),$$

where θ is the angle of the final state lepton with respect to the neutrino's direction of travel and T is the kinetic energy of the lepton. The same holds for the SuSAv2 and Hartree-Fock Hadron Tensors. To the output of these tensors we apply the Jacobian $\frac{dT}{dp} = \frac{p}{T}$ to convert them in to $\sigma_{HT} = \frac{d^2\sigma}{d\cos\theta dp}(E_\nu, \cos\theta, T(p))$. The Hadron Tensors for CRPA are divided into three regions of q_0, so they have to be loaded into the code separately. The SuSAv2 Hadron Tensor is included only for Carbon, but for other targets a re-scaling according to [33] is used.

From the Spectral Function templates we get the triple differential cross-section

$$\sigma_{SF}^{preInterpol} = \frac{d^3\sigma}{d\cos\theta dpdE_\nu}(E_\nu, \cos\theta, p).$$

The template is generated at $M_A^{QE} = 1.21$ GeV. A reweighting of samples using $M_A^{QE} = 1.03$ GeV is not meaningful without a prior reweighting to $M_A^{QE} = 1.21$ GeV. Here $\cos\theta$ is again the leptons angle with respect to the neutrino, while p is the lepton's momentum. To convert this to the same double differential cross-section as we have for the tensors, we select the slice of the 3D histogram that corresponds to the incoming neutrino energy. This 2D distribution in $\cos\theta$ and p is then normalised, such that the width-weighted integral is equal to $\sigma(E_\nu)$. Then selecting the corresponding angle and kinetic energy bin in this distribution returns the double differential cross-section $\frac{d^2\sigma}{d\cos\theta dp}(E_\nu, \cos\theta, p)$. This makes the Hadron Tensor results comparable with the results from the Spectral Function template.

Since the binning in neutrino energy of the SF template is given by 50 MeV and with that quite coarse, we need to do a three-dimensional interpolation to get more fine-grained results. This is done by selecting two neighboring energy slices. First, we select the energy slice which corresponds to the incoming neutrino energy of the sample event to reweight. If the neutrino energy is larger than the bin center energy, we select the next higher energy slice. While if the neutrino energy is below the bin center, we select the lower neighbor as our second energy slice.

In each slice a two-dimensional interpolation using `TH2D->Interpolate()` is performed. Then a linear interpolation between these two cross-sections results in σ_{SF}.

The weights ω are then calculated by $\omega = \frac{\sigma_{HT}}{\sigma_{SF}}$, where σ_{HT} is the double differential cross-section we get from the Hadron Tensors, while σ_{SF} is the double differential cross-section we get from the Spectral Function template.

A.2.1 Dynamic Normalisation Method

Since we observed some dependency of the norm on the exact energy that we attribute to a given two-dimensional slice for the normalization, we implemented a second method for this attribution. This method takes into account how quickly the total cross-section changes as a function of the neutrino energy. For this, we first select the energy bin of the $\sigma(E)$ histogram, corresponding to the incoming neutrino energy. We then take the right edge of the bin and calculate

$$\Delta = \frac{\sigma_{higher} - \sigma_{center}}{\sigma_{higher}}$$

This will be a measure of how much we move our attributed energy away from the bin center. The attributed energy is then calculated as

$$E_{attr} = E_{center} + \Delta \times \frac{\text{bin width}}{2}$$

This means that, when the cross-section is steeply growing, we attribute energy on the far right of the bin to that bin. While when the cross-section is falling, we move the attributed energy to the left of the bin center. This leads to marginally better reweightings in the low energy region, while the high energy region is not affected.

A.2.2 Hybrid Model

To get the weights for the Hybrid model we interpolate between CRPA and SuSAv2 with respect to the energy transfer q_0. For $q_0 \leq 0.5$ GeV we use the CRPA model to describe the interaction. For $q_0 \geq 1$ GeV we use the SuSAv2 model. In the intermediate region of $q_0 \in (0.5, 1)$ GeV we use a linear interpolation between these two models given by

$$\sigma_{HT}^{Hybrid} = \sigma_{CRPA} + (\sigma_{SuSAv2} - \sigma_{CRPA}) \times \frac{q_0 - 0.5}{1 - 0.5}.$$

A.2.3 Catches

To prevent meaningless weights we implement several catches. When the cross-section of either the Hadron Tensors or the Template is zero, we set the weight to 1. This mainly happens when an event lies on the edge of the corresponding phase space. If the weight is larger than 10, we set it to 10. This way we prevent large weights that could lead to unwanted behavior. We do not set these weights to 1, since in regions where the phase-space does not perfectly overlap, this can happen, and here larger weights than 1 are expected.
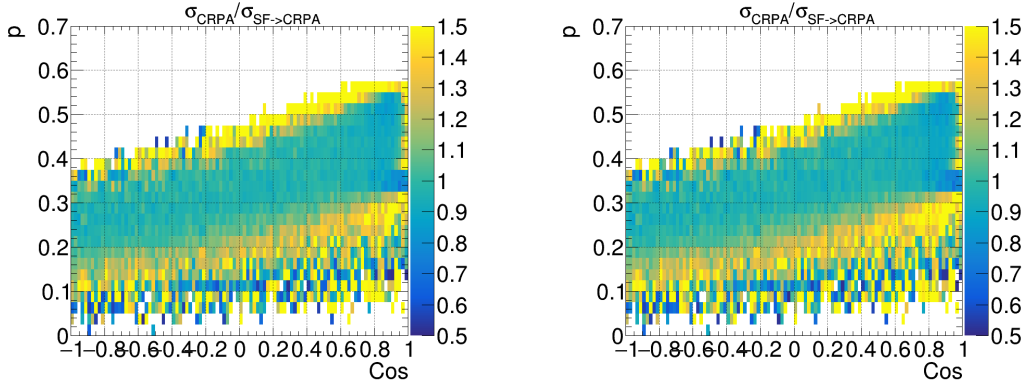
(a) Reweighted SF to CRPA, Dynamically   (b) Reweighted SF to CRPA, Bin Center
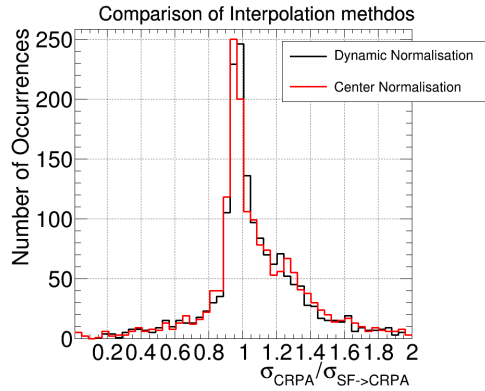
(c) Occurrences of the ratio.

Figure A.1: The results of the reweighting of ν_e on Carbon following a flat flux between 400 and 600 MeV, using the different normalisation options. The first one uses the dynamical normalisation, while the second the normalisation to the energy corresponding to the bin center. These plots show the ratio between the Spectral Function reweighted to CRPA and the actual CRPA theory predictions. The third plot shows the distribution of these ratios for both cases. We see that the dynamical method is a slightly narrower and more centered around 1.

A.3   Evaluation

The reweighting works well for extended fluxes but has problems due to nonoverlapping phase space with very narrow and monoenergetic fluxes. We tested the reweighting for the CRPA model thoroughly and looked at the T2K ν_e flux for the SuSAv2 model. The reweighted NEUT Spectral Function results are compared to the corresponding GENIE generations following the same fluxes or to the output of the Hadron Tensors in the case of a flat or monoenergetic flux.[3]

---

[3]For a collection of tested configuration https://t2k.org/docs/technotes/434/ValidationPlots

A.3.1 Mono Energetic Fluxes

We look at a 800 MeV ν_μ flux on Carbon. In fig. A.2a we see the NEUT output for the Spectral Function as the cross-section in phase space. fig. A.2b shows the reweighted Spectral Function. Comparing it to the third histogram in fig. A.2c, the cross-section resulting from the CRPA Hadron Tensors, we see that the reweighting is not able to reproduce the peak position at the edge of the phase space. This is due to the limited overlap at the edge of phase space. This can also be seen in the fig. A.2d, where the ratio between the reweighted Spectral Function and the original CRPA model is shown. This should be a flat plot at 1, while the Monte Carlo nature of the Spectral Function Template explains the deviations at the edges. In the peak cross-section region, the ratio should be very close to one, since here we have more statistics. But here the peak region has a ratio smaller than 0.75, meaning that the reweighted Spectral Function cross-section is too small compared to the actual CRPA model. This affects mono-energetic or very narrow fluxes since here the CRPA cross-section peak is situated directly at the edge of phase space. In the region where we have an overlap of phase space, we have a better agreement between the CRPA model and its reweighted Spectral Function counterpart. This can be seen by the shortening of the cross-section tail in fig. A.2b. The reweighting should non the less be used with caution in the case of very narrow and monoenergetic fluxes.

A.3.2 Wide Flat Flux

We look at three different wide flat fluxes, to test different energy regions. The shown plots are for ν_e interacting on Carbon for 400-600 MeV, 800-1000 MeV and 1500-2000 MeV. In general, we can see that the wider energy region shifts the peak from the edge of phase space to a region where there is more overlap between these two models. This is reflected in a flatter comparison plot. The CRPA model and reweighted Spectral Function agree not only in the region of peak cross-section but also in the elongated tail.

In the intermediate region of 0.8 to 1 GeV, we see that the comparison plot is quite smoothly distributed around 1, especially in the peak energy region. This shows that the reweighting works well for this energy region.

The high energy region of 1.5 to 2 GeV in fig. A.5c shows that the energy transfer is limited to 1 GeV. The lowest energy that a final state lepton can have with this flux is 500 MeV, which in the case of ν_e equals its momentum. In the region with a low cross-section, we see that the reweighting struggles to reproduce the CRPA model. This shows the limitations of pure CRPA reweighting. Non the less the peak cross-section region is reproduced quite well by the reweighting.

For wider band fluxes ($E_{high} - E_{low} > 100$ MeV) the intermediate energy region between 600 and 1000 MeV is the region where the reweighting works the best. Here the shape and the normalization are reproduced better compared to the low or high energy regions. Fortunately, this is where we expect that this method is used the most since the

(a) Spectral Function

(b) Reweighted SF to CRPA

(c) CRPA from Theory
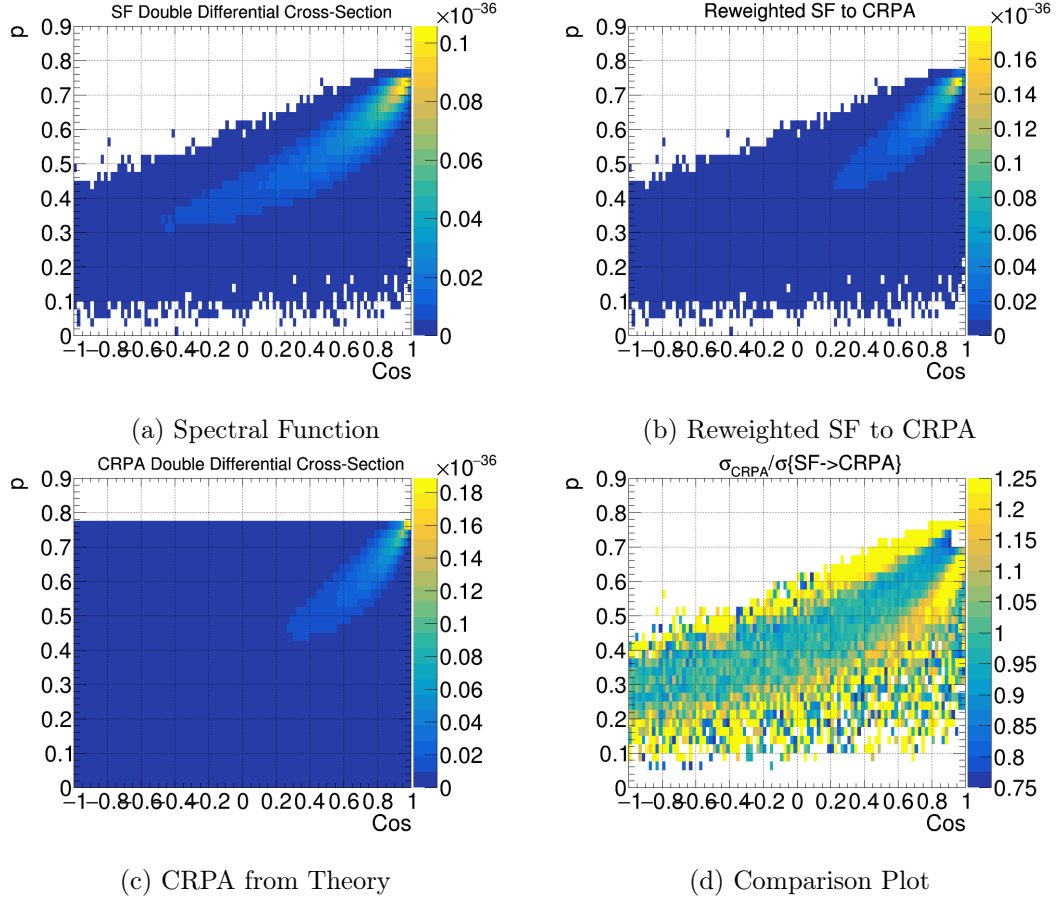
(d) Comparison Plot

Figure A.2: The results from the Spectral Function to CRPA reweighting with a mono-energtic ν_μ flux on Carbon at 800 MeV. The comparison plot is the ratio between the Spectral Function reweighted to CRPA and the actual CRPA theory predictions. This should be, in the peak region be around one, while it falls below 0.75 due to the limited phase space overlap.

T2K flux resides in this energy region.

A.3.3 T2K Flux

For the T2K flux, we use the ν_e flux at ND280 with electron neutrinos and Oxygen as a target. We see that the reweighting works well for the T2K flux since the comparison plot is mainly distributed around one. On the edge, we see some deviations since we compare two Monte Carlo generations with limited statistics.

(a) Spectral Function

(b) Reweighted SF to CRPA

(c) CRPA from Theory
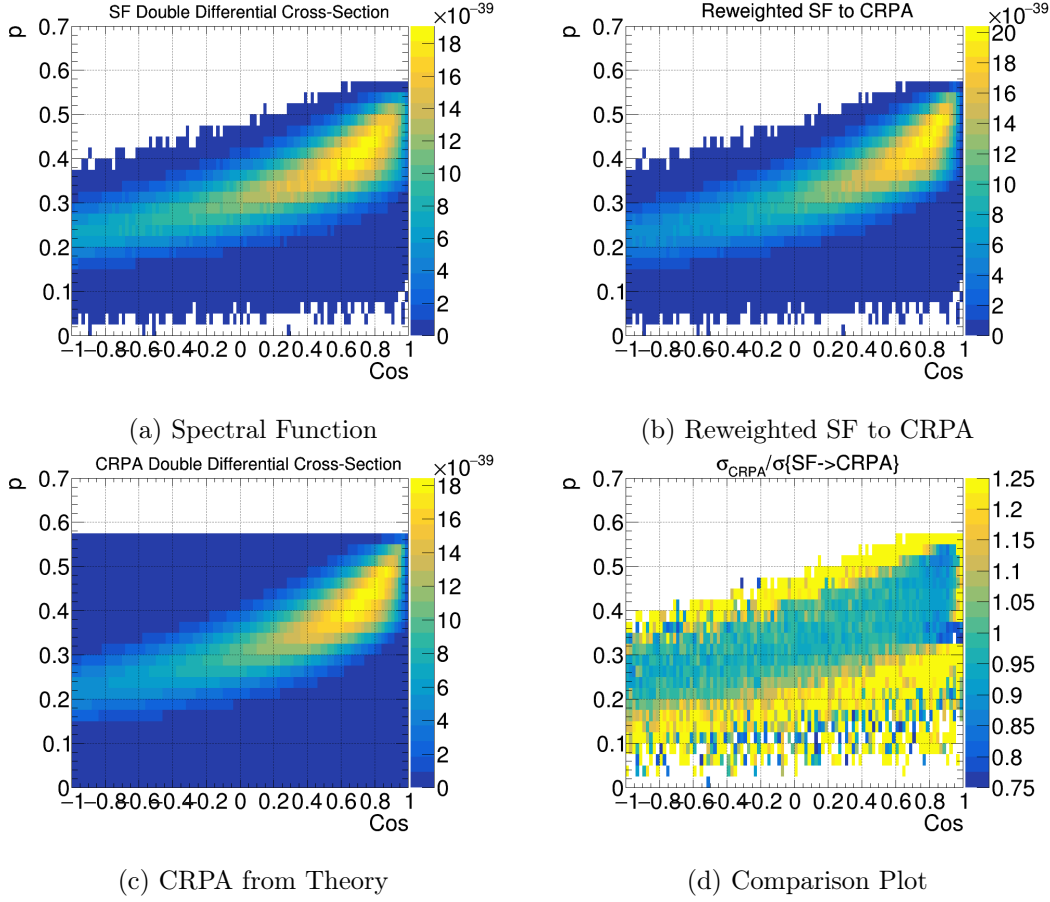
(d) Comparison Plot

Figure A.3: The results from the Spectral Function to CRPA reweighting with a ν_e flux on Carbon with $E_\nu \in (400, 600)$ MeV. The comparison plot is the ratio between the Spectral Function reweighted to CRPA and the actual CRPA theory predictions.

A.3.4 Hybrid Model

In fig. A.7 we look at the normalized distribution of the weights with respect to the energy transfer q_0 of the T2K ν_e flux at ND280. We see that the hybrid model nicely interpolates between the CRPA model in the region of low energy transfer and the SuSAv2 model at higher energy transfers. This way the wide weight distribution at high q_0 for the CRPA model is avoided. Further, the limitations of the CRPA hadron tensors to energy transfers below 1 GeV are lifted by the extension to the SuSAv2 model.

(a) Spectral Function

(b) Reweighted SF to CRPA

(c) CRPA from Theory
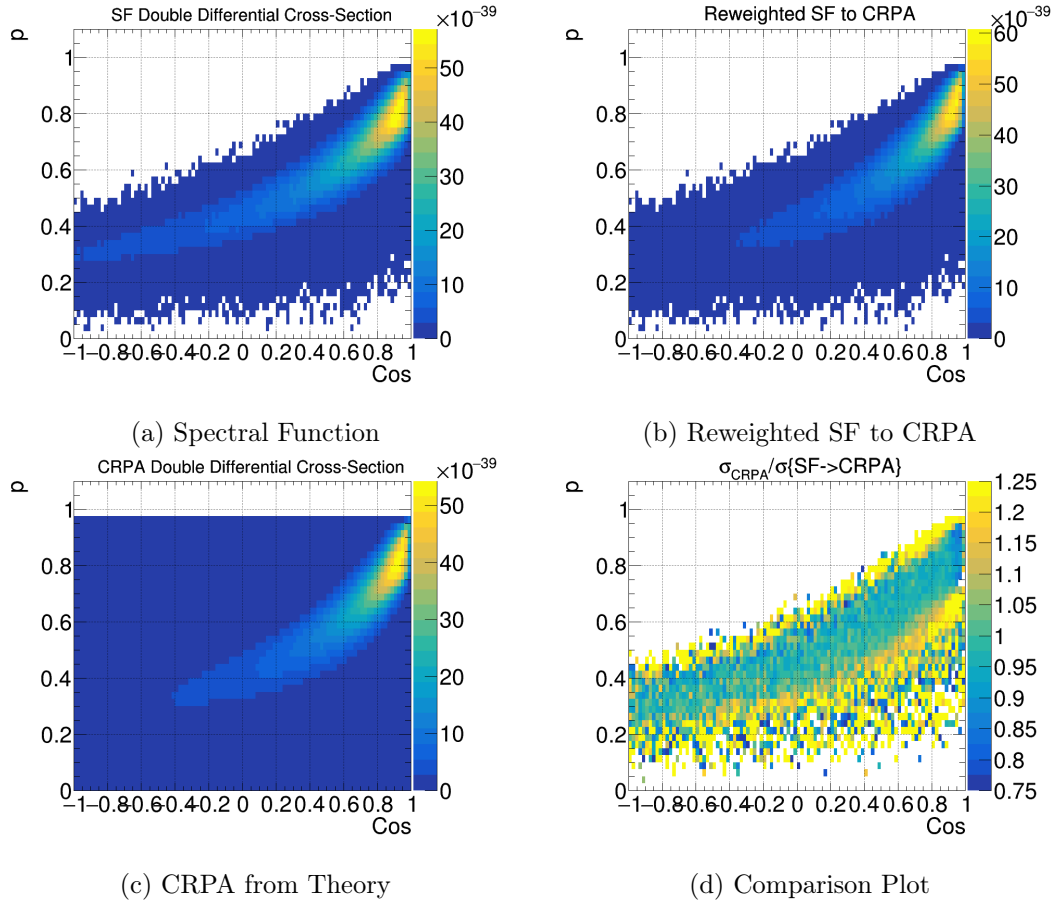
(d) Comparison Plot

Figure A.4: The results from the Spectral Function to CRPA reweighting with a ν_e flux on Carbon with $E_\nu \in (800, 1000)$ MeV. The comparison plot is the ratio between the Spectral Function reweighted to CRPA and the actual CRPA theory predictions.

(a) Spectral Function

(b) Reweighted SF to CRPA

(c) CRPA from Theory
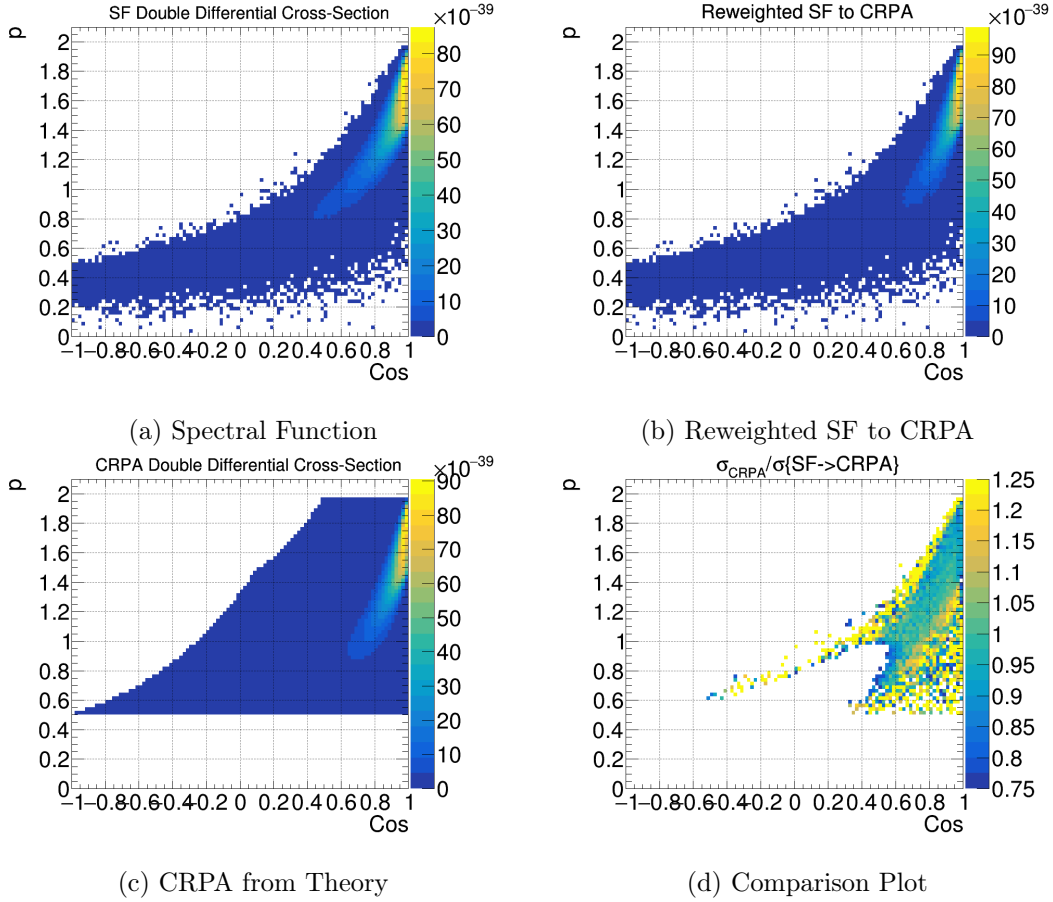
(d) Comparison Plot

Figure A.5: The results from the Spectral Function to CRPA reweighting with a ν_e flux on Carbon with $E_\nu \in (1500, 2000)$ MeV. The comparison plot is the ratio between the Spectral Function reweighted to CRPA and the actual CRPA theory predictions. In the CRPA theory predictions we see the limitation of $q_0 \leq 1$ GeV, which translates to a problematic reweighting in the lower energy region.

(a) Spectral Function

(b) Reweighted SF to CRPA

(c) CRPA from Genie MC
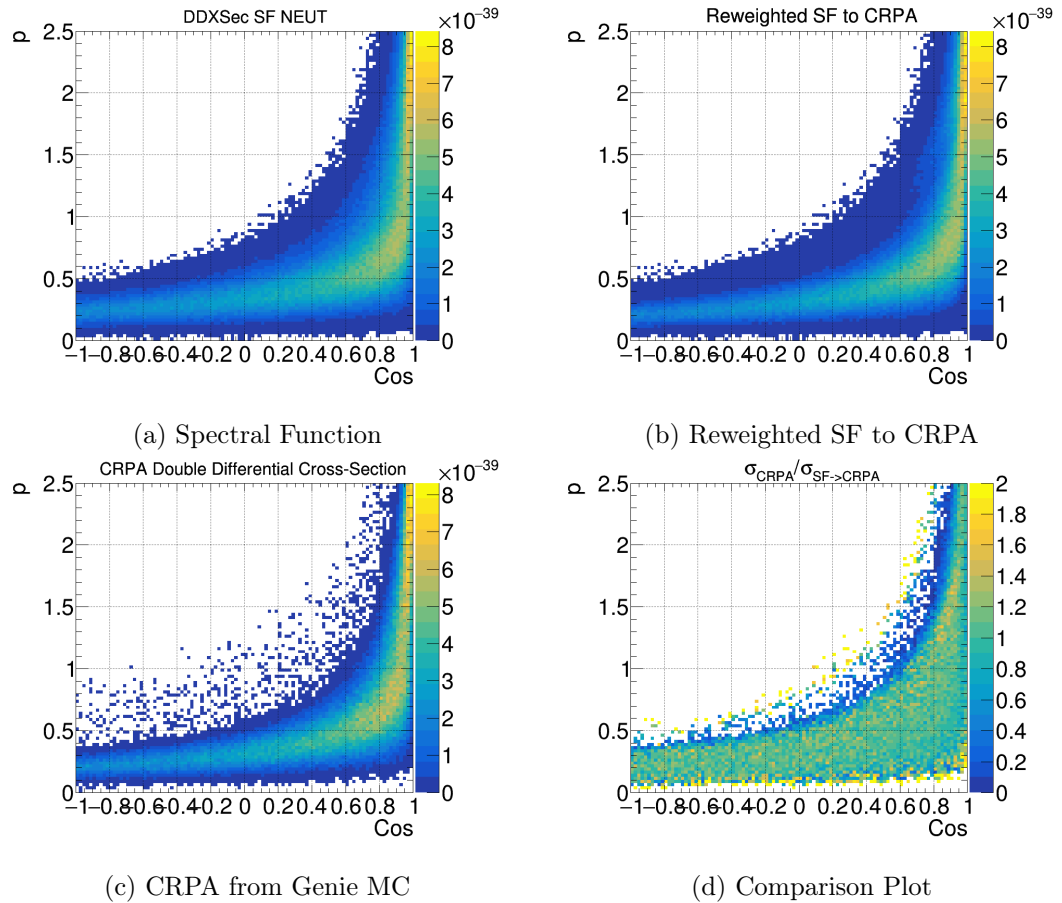
(d) Comparison Plot

Figure A.6: The results from the Spectral Function to CRPA reweighting with ν_e following the ν_e ND280 flux. As a target Oxygen is used. The comparison plot is the ratio between the Spectral Function reweighted to CRPA and the actual CRPA theory predictions. Here the CRPA plot is generated using the GENIE event generator with 500.000 events.

(a) CRPA model

(b) Hybrid model

(c) SuSAv2 model
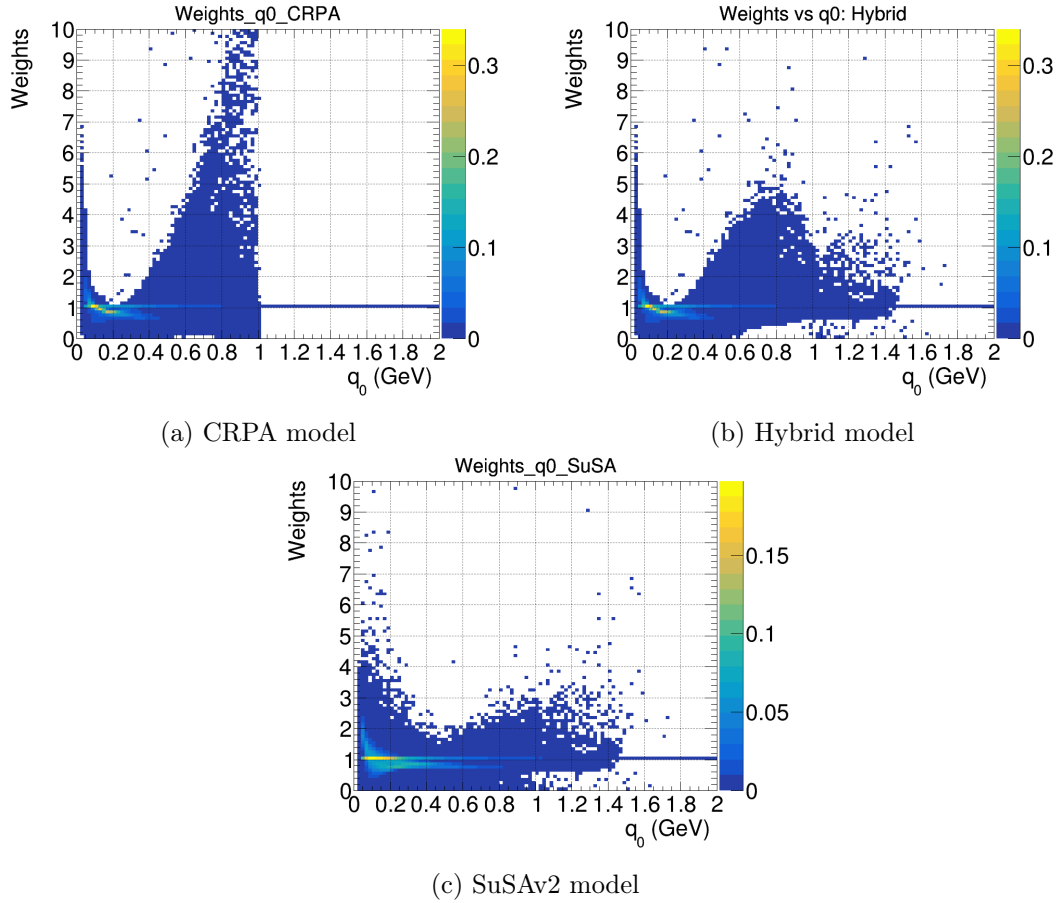
Figure A.7: The weight distribution with respect to the energy transfer q_0. We see the affect of the interpolation in removing the wide distribution of weights at higher energy transfers. The line at one is due to the catches and mainly attributed to missing phase space overlap.

Oscillations and Wavepackets

Neutrino oscillations are a quantum interference effect, where the coherent creation and detection of the neutrino wave packets plays an important role. This explanation follows closely [34] and [35].

As the mass-difference between the neutrinos is smaller than the energy differences, the Heisenberg principle gets important. As wave-packages with different masses propagate at different phase velocities, as seen in fig. B.1, this can lead to the destruction of the interference and with this, the different massive neutrinos cannot be detected coherently. This leads to the fact that the probability of transitions between different flavours does not oscillate as a function of the source-detector distance. To see this, first it has to be noted that any interaction is connected to a space uncertainty σ_x related to the corresponding momentum uncertainty σ_p by $\sigma_x\,\sigma_p \approx 1/2$. As the total momentum uncertainty can be approximated by the quadratic sum of the momentum uncertainty of all the localised particles taking part in the interaction, the space uncertainty can be written as

$$(\sigma_x)^{-2} \approx \sum_i (\sigma_x^i)^{-2}. \tag{B.1}$$

Here it becomes clear, that the particles with a smaller space uncertainty contribute in a dominant way to the overall spacial uncertainty.

In an interaction process, the time that wave packets overlap is called coherence time σ_t. For particles with velocity v_i, this time can be approximated as

$$(\sigma_t)^{-2} \approx \sum_i \left(\frac{\sigma_x^i}{v_i}\right)^2. \tag{B.2}$$

Since the neutrino masses are assumed to be small and that they do not interact with other final state particles, this approximation yields $\sigma_x^\nu \approx \sigma_t^\nu$.

In a detection process of a massive superposition, the single wave packets are separated by a distance of $\Delta x = \Delta v T$, where Δv is the difference in phase velocity. Large source-detector distances therefore lead to a lack of overlap between the wave packets. The coherent size in this case is

$$\sigma_{x,\text{eff}}^\nu \approx \sqrt{(\sigma_x^\nu)^2 + \Delta x^2} \approx \sqrt{\sigma_t^2 + (\Delta v T)^2}. \tag{B.3}$$
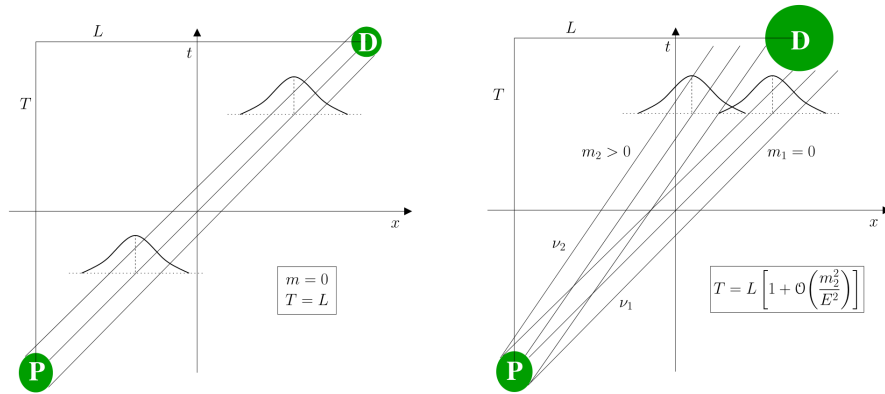
Figure B.1: Schematic representation of the propagation of wave packets. On the left, a single massless particle propagates, while on the right, a superposition of a massless and a massive ultra relativistic particle is shown. If the separation between the two wave packets gets to large, the neutrino oscillations are not detectable anymore. Both propagate from the production state at P to the detection region D. Taken from [34].

As seen, the particle with the smallest space uncertainty contributes the most to the coherence size. If the effective coherence size of the neutrino is dominated by the separation of the wave packets ($\Delta vT \gg \sigma_t$) and another particle with a smaller space uncertainty, like a muon, is participating in the detection process, the different massive neutrinos cannot be detected coherently. In such a case, the neutrino flavour does not oscillate as a function of the source-detector distance, but the incoherent transition probability will be measured.

If the spacial uncertainty of the other particles is larger than the effective coherence size of the neutrino, the different massive neutrino can be detected in their superposition and the neutrino oscillation is measurable.

The wave packet treatment of the neutrinos shows, that the neutrino oscillation is a quantum interference effect, based on the Heisenberg principle. The oscillations are due to the difference between the weak and mass eigenstates, but to detect the oscillation, one has to keep in mind the coherence. Meaning that if the weak eigenstates would be the same as the mass eigenstates, no oscillations would be measured, even thought the mass differences are so small. While if the mass-differences where larger, no oscillations would be measured, as the Heisenberg principle would precisely "determine" the flavour of the neutrino at creation.

Full Set of Evaluated Models

In this table a collection of the results of the compared models is shown. The models used are CRPA at different M_A^{QE} values (the standard is 1.03 GeV), Spectral Function with different M_A^{QE} values (1.03 as nominal) and Pauli Blocking disabled (w/o PB), the Local Fermi Gas (LFG), the SuSAv2, Hartee Fock (HF).

If nothing else is noted, the models where evaluated on Oxygen, since the eventrate that was used corresponds to the expected detected flux at Super Kamiokande, and therefore on water.

To evaluate the differences between Carbon and Oxygen, the SF model and the CRPA model where further evaluated on Carbon, but the flux averaging non the less was done over the expected event rate on Oxygen.

Model 1	Model 2	$\delta_{\mu \to e}$	$\delta_{\bar{\mu} \to \bar{e}}$	$\delta_{\bar{e} \to e}$	Cor.
SUSA	CRPA	0.0015515	0.00239941	0.00395092	-1
SF	CRPA	0.0247555	0.0104083	0.0143472	1
SF	SUSA	0.023204	0.0128077	0.0103963	1
LFG	CRPA	0.0278462	0.0192388	0.00860733	1
LFG	SUSA	0.0262947	0.0216383	0.00465641	1
LFG	SF	0.00309072	0.00883059	0.00573987	1
SF w/o PB	CRPA	0.0238518	0.00840181	0.01545	1
SF w/o PB	SUSA	0.0223003	0.0108012	0.0114991	1
SF w/o PB	SF	0.000903626	0.00200645	0.00110282	1
SF w/o PB	LFG	0.00399434	0.010837	0.00684269	1
SF M_A^{QE}=1.03	CRPA	0.0248658	0.00933779	0.015528	1
SF M_A^{QE}=1.03	SUSA	0.0233143	0.0117372	0.0115771	1
SF M_A^{QE}=1.03	SF	0.000110382	0.00107046	0.00118085	-1

SF M_A^{QE}=1.03	LFG	0.00298033	0.00990105	0.00692072	1
SF M_A^{QE}=1.03	SF w/o PB	0.00101401	0.000935984	7.80236e-05	1
SF M_A^{QE}=1.21	CRPA	0.0249784	0.00996568	0.0150127	1
SF M_A^{QE}=1.21	SUSA	0.0234269	0.0123651	0.0110618	1
SF M_A^{QE}=1.21	SF	0.000222964	0.000442577	0.000665541	-1
SF M_A^{QE}=1.21	LFG	0.00286775	0.00927317	0.00640541	1
SF M_A^{QE}=1.21	SF w/o PB	0.00112659	0.00156387	0.000437282	1
SF M_A^{QE}=1.21	SF M_A^{QE}=1.03	0.000112582	0.000627887	0.000515305	1
CRPA M_A^{QE}=1.21	CRPA	0.000332565	0.00033561	0.000668174	-1
CRPA M_A^{QE}=1.21	SUSA	0.00188407	0.00273502	0.00461909	-1
CRPA M_A^{QE}=1.21	SF	0.025088	0.0100726	0.0150154	1
CRPA M_A^{QE}=1.21	LFG	0.0281787	0.0189032	0.0092755	1
CRPA M_A^{QE}=1.21	SF w/o PB	0.0241844	0.0080662	0.0161182	1
CRPA M_A^{QE}=1.21	SF M_A^{QE}=1.03	0.0251984	0.00900218	0.0161962	1
CRPA M_A^{QE}=1.21	SF M_A^{QE}=1.21	0.025311	0.00963007	0.0156809	1
CRPA M_A^{QE}=0.8	CRPA	0.000407313	0.00074371	0.00115102	-1
CRPA M_A^{QE}=0.8	SUSA	0.00114419	0.0016557	0.0027999	-1
CRPA M_A^{QE}=0.8	SF	0.0243481	0.011152	0.0131962	1
CRPA M_A^{QE}=0.8	LFG	0.0274389	0.0199826	0.0074563	1
CRPA M_A^{QE}=0.8	SF w/o PB	0.0234445	0.00914552	0.014299	1
CRPA M_A^{QE}=0.8	SF M_A^{QE}=1.03	0.0244585	0.0100815	0.014377	1
CRPA M_A^{QE}=0.8	SF M_A^{QE}=1.21	0.0245711	0.0107094	0.0138617	1
CRPA M_A^{QE}=0.8	CRPA M_A^{QE}=1.21	0.000739877	0.00107932	0.0018192	-1
CRPA M_A^{QE}=1.03	CRPA	2.97879e-05	2.16418e-05	8.14608e-06	1
CRPA M_A^{QE}=1.03	SUSA	0.00152172	0.00242106	0.00394277	-1
CRPA M_A^{QE}=1.03	SF	0.0247257	0.0103866	0.0143391	1
CRPA M_A^{QE}=1.03	LFG	0.0278164	0.0192172	0.00859918	1
CRPA M_A^{QE}=1.03	SF w/o PB	0.023822	0.00838017	0.0154419	1
CRPA M_A^{QE}=1.03	SF M_A^{QE}=1.03	0.0248361	0.00931615	0.0155199	1

CRPA M_A^{QE}=1.03	SF M_A^{QE}=1.21	0.0249486	0.00994404	0.0150046	1	
CRPA M_A^{QE}=1.03	CRPA M_A^{QE}=1.21	0.000362353	0.000313968	0.000676321	-1	
CRPA M_A^{QE}=1.03	CRPA M_A^{QE}=0.8	0.000377525	0.000765352	0.00114288	-1	
HF	CRPA	0.00132793	0.00190827	0.000580337	1	
HF	SUSA	0.000223575	0.00430768	0.00453126	-1	
HF	SF	0.0234275	0.00849999	0.0149275	1	
HF	LFG	0.0265182	0.0173306	0.00918766	1	
HF	SF w/o PB	0.0225239	0.00649354	0.0160304	1	
HF	SF M_A^{QE}=1.03	0.0235379	0.00742953	0.0161084	1	
HF	SF M_A^{QE}=1.21	0.0236505	0.00805742	0.0155931	1	
HF	CRPA M_A^{QE}=1.21	0.00166049	0.00157266	8.78374e-05	1	
HF	CRPA M_A^{QE}=0.8	0.000920615	0.00265198	0.00173136	1	
HF	CRPA M_A^{QE}=1.03	0.00129814	0.00188662	0.000588483	1	
CRPA C	CRPA	0.000992411	0.00150007	0.000507659	1	
CRPA C	SUSA	0.000559092	0.00389948	0.00445858	-1	
CRPA C	SF	0.023763	0.00890819	0.0148549	1	
CRPA C	LFG	0.0268538	0.0177388	0.00911499	1	
CRPA C	SF w/o PB	0.0228594	0.00690174	0.0159577	1	
CRPA C	SF M_A^{QE}=1.03	0.0238734	0.00783772	0.0160357	1	
CRPA C	SF M_A^{QE}=1.21	0.023986	0.00846561	0.0155204	1	
CRPA C	CRPA M_A^{QE}=1.21	0.00132498	0.00116446	0.000160516	1	
CRPA C	CRPA M_A^{QE}=0.8	0.000585099	0.00224378	0.00165868	1	
CRPA C	CRPA M_A^{QE}=1.03	0.000962623	0.00147843	0.000515805	1	
CRPA C	SF C	0.023261	0.0112192	0.0120418	1	

Table C.1: The uncertainties calcualted for the differences between the CRPA model and the Spectral Function. The full correlatin comes from the comparison of only two models.

Cross-Sections

In this Appendix the cross-sections for the anti-neutrinos.

(a) ν_e on Carbon   (b) ν_μ on Carbon   (c) Fractional Cross-Section
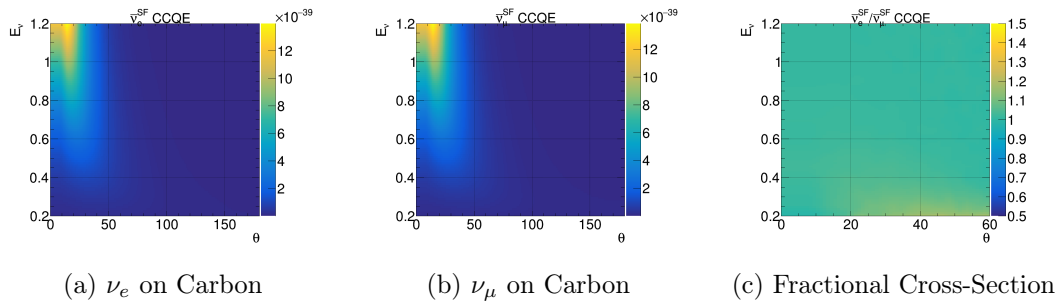
Figure D.1: The electron and muon anti-neutrino cross-section $\frac{d\sigma}{d\cos\theta}$ on Carbon assuming the Spectral Function with $M_aA = 1.03$ GeV. The third plot shows the ratio between the electron and muon anti-neutrino cross-section. It is flatly distributed around 1, with a small electron deficiency in the low energy region.

(a) ν_e on Carbon   (b) ν_μ on Carbon   (c) Fractional Cross-Section
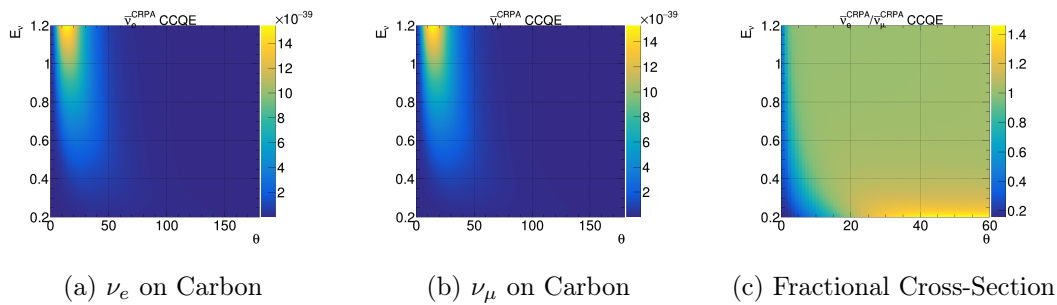
Figure D.2: The electron and muon anti-neutrino cross-section $\frac{d\sigma}{d\cos\theta}$ on Carbon assuming the CRPA model using the Hadron Tensors. The third plot shows the ratio between the electron and muon anti-neutrino cross-section. Here we see that the low angle region looks vastly different from the corresponding plot for the Spectral Function. The muon anti-neutrino cross-section dominates the region of low angles stronger than in the Spectral Function case.

ETH

Eidgenössische Technische Hochschule Zürich
Swiss Federal Institute of Technology Zurich

Declaration of originality

The signed declaration of originality is a component of every semester paper, Bachelor's thesis, Master's thesis and any other degree paper undertaken during the course of studies, including the respective electronic versions.

Lecturers may also require a declaration of originality for other written papers compiled for their courses.

I hereby confirm that I am the sole author of the written work here enclosed and that I have compiled it in my own words. Parts excepted are corrections of form and content by the supervisor.

Title of work (in block letters):

Nuclear Effects For Electron-Neutrino-nucleus interactions and their impact on the search for CP-violation at the T2K and Hyper-K experiments

Authored by (in block letters):
For papers written by groups the names of all authors are required.

Name(s):	First name(s):
Dieminger	Till

With my signature I confirm that
- I have committed none of the forms of plagiarism described in the 'Citation etiquette' information sheet.
- I have documented all methods, data and processes truthfully.
- I have not manipulated any data.
- I have mentioned all persons who were significant facilitators of the work.

I am aware that the work may be screened electronically for plagiarism.

Place, date
28th March 2022, Zürich

Signature(s)

For papers written by groups the names of all authors are required. Their signatures collectively guarantee the entire content of the written paper.